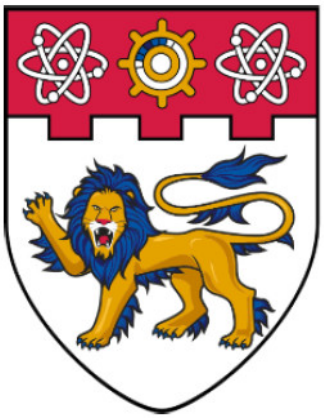

NANYANG TECHNOLOGICAL UNIVERSITY
SINGAPORE

Photodegradation of Micropollutants in Water by UV/H_2O_2 and UV/Persulfate

Zhang Yiqing

School of Civil and Environmental Engineering

2019

Photodegradation of Micropollutants in Water by UV/H_2O_2 and UV/Persulfate

Zhang Yiqing

School of Civil and Environmental Engineering

A thesis submitted to the Nanyang Technological University
in partial fulfilment of the requirements for the degree of
Doctor of Philosophy

2019

Statement of Originality

I hereby certify that the work embodied in this thesis is the result of original research, is free of plagiarised materials, and has not been submitted for a higher degree to any other University or Institution.

27/05/2019
Date


Zhang Yiqing

Supervisor Declaration Statement

I have reviewed the content and presentation style of this thesis and declare it is free of plagiarism and of sufficient grammatical clarity to be examined. To the best of my knowledge, the research and writing are those of the candidate except as acknowledged in the Author Attribution Statement. I confirm that the investigations were conducted in accord with the ethics policies and integrity standards of Nanyang Technological University and that the research data are presented honestly and without prejudice.

27/05/2019
. . . . . .
Date


. . . . . .
A/P Lim Teik-Thye

Authorship Attribution Statement

This thesis contains material from 5 papers published in the following peer-reviewed journals in which I am listed as an author.

Section 2.1 is published as Zhang, Y., Lim, T.T. **2018**. Fate and effects of cytostatic pharmaceuticals in the environment. Springer. Book Chapter.
The contributions of the co-authors are as follows:

- I designed the experiment and prepared the manuscript drafts.
- A/P Lim provided the project direction and edited the manuscript.

Section 4.2 is published as Zhang, Y.; Zhang, J.; Xiao, Y.; Chang, V.W.C.; Lim, T.T. **2017**. Direct and indirect photodegradation pathways of cytostatic drugs under UV germicidal irradiation: Process kinetics and influences of water matrix species and oxidant dosing. ***Journal of Hazardous Materials***, 324, 481-488. DOI: 10.1016/j.jhazmat.2016.11.016.
The contributions of the co-authors are as follows:

- I designed the experiment and prepared the manuscript drafts.
- Dr. Xiao provided guidance in the experimental design.
- Dr. Zhang and Dr. Chang assisted in the sample preparation.
- A/P Lim provided the project direction and edited the manuscript.

Section 4.3 is published as Zhang, Y.; Zhang, J.; Xiao, Y.; Chang, V.W.C.; Lim, T.T. **2017**. Degradation of cyclophosphamide and 5-fluorouracil in water using UV and UV/H_2O_2: Kinetics investigation, pathways and energetic analysis. ***Journal of Environmental Chemical Engineering***, 5, 1133-1139. DOI: 10.1016/j.jece.2017.01.013.
The contributions of the co-authors are as follows:

- I designed the experiment and prepared the manuscript drafts.
- Dr. Xiao provided guidance in the experimental design.

- Dr. Zhang and Dr. Chang assisted in the sample preparation.
- A/P Lim provided the project direction and edited the manuscript.

Section 4.4 is published as Zhang, Y.; Zhang, J.; Xiao, Y.; Chang, V.W.C.; Lim, T.T. **2016**. Kinetic and mechanistic investigation of azathioprine degradation in water by UV, UV/H_2O_2 and UV/persulfate. ***Chemical Engineering Journal***, 302, 526-534. DOI: 10.1016/j.cej.2016.05.085.

The contributions of the co-authors are as follows:

- I designed the experiment and prepared the manuscript drafts.
- Dr. Xiao provided guidance in the experimental design.
- Dr. Zhang and Dr. Chang assisted in the sample preparation.
- A/P Lim provided the project direction and edited the manuscript drafts.

Chapter 5 is published as Zhang, Y.; Xiao, Y.; Zhong, Y.; Lim, T.T. **2019**. Comparison of amoxicillin photodegradation in the UV/H_2O_2 and UV/persulfate systems: Reaction kinetics, degradation pathways, and antibacterial activity. ***Chemical Engineering Journal***, 372, 420-428. DOI: 10.1016/j.cej.2019.04.160

The contributions of the co-authors are as follows:

- I designed the experiment and prepared the manuscript drafts.
- Dr. Xiao provided guidance in the experimental design.
- Dr. Zhong assisted in the sample preparation and data collection.
- A/Prof Lim provided the project direction.

27/05/2019 .....
Date

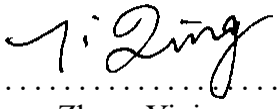
..... Zhang Yiqing

ACKNOWLEDGEMENT

First and foremost, I would like to sincerely thank my supervisor, A/P Lim Teik-Thye, for his constructive guidance and support throughout my study. He has continuously provided me with enthusiasm and vision for my research work. Without his guidance, this work would not have been possible.

I also would like to thank all staffs and students in School of Civil and Environmental Engineering and Nanyang Environment and Water Research Institute for their friendship and corporation, especially for Dr. Xiao Yongjun, Dr. Zhang Jiefeng, Dr. Wang Penghua, Dr. Ronn Goei, Dr. Oh Wen Da, Dr. Wu Weiyi and Dr. Hu Zhongting. Without their kind help, I would not have opportunity to improve myself in the stimulating and friendly environment.

I would like to express my sincere gratitude to Nanyang Technological University for the Research Student Scholarship. Without this financial assistance, I could not conduct my research project smoothly.

Finally, with all my heart, I would like to express my deepest appreciation to my family and my boyfriend for their love. Their understanding and endless love have been my greatest strength.

SUMMARY

The emerging micropollutants have posed serious threat to the ecological environment and human beings. Among them, cytostatic drugs and antibiotics have raised great public concern due to their frequent usage, high persistence, and biological stability towards conventional water treatment processes. Therefore, this study focused on the photodegradation of cytostatic drugs and amoxicillin using UV, UV/H_2O_2 and UV/persulfate ($S_2O_8^{2-}$, PS) processes. In addition, quantitative structure–property relationship (QSPR) method was applied to model the photodegradation efficiency of the emerging micropollutants by UV/H_2O_2 and UV/PS processes.

In the first part of this study, direct and indirect UV photolysis were applied to investigate the degradation effect of eight cytostatic drugs using a pseudo first-order kinetic model. Six cytostatic drugs were degraded by less than 10% at UV dose of 400 mJ·cm^{-2}, indicating the ineffectiveness of UV photolysis towards most of the investigated cytostatic drugs. The influence of water matrix components was investigated, including natural dissolved organic matter (DOM), bicarbonate (HCO_3^-), nitrate (NO_3^-), chloride (Cl^-), and sulfate (SO_4^{2-}). Treated water from a water treatment plant and secondary effluent from a wastewater treatment plant were employed as natural waters to evaluate the potential application of the processes. The primary photodegradation byproducts of cytostatic drugs were identified to investigate the degradation mechanism of the processes.

In the second part of this study, the reaction kinetics, degradation pathways, and antibacterial activity of UV/H_2O_2 and UV/PS systems were compared using amoxicillin as a typical antibiotic. The extensive use of non-metabolized amoxicillin has led to the contamination of the aquatic environment. UV irradiation alone shows negligible effect on amoxicillin degradation; while the degradation efficiency of

amoxicillin increases significantly with the addition of oxidant due to the generation of radical species. The second-order rate constant of amoxicillin with $HO^{\bullet}$ and $SO_4^{\bullet-}$ are $3.9 \times 10^9\ M^{-1}\ s^{-1}$ and $3.5 \times 10^9\ M^{-1}\ s^{-1}$, respectively. In the UV/PS system at neutral pH, the contributions of UV, $HO^{\bullet}$, and $SO_4^{\bullet-}$ for amoxicillin degradation are 7.3%, 22.8%, and 69.9%, respectively. Based on the experimental evidence substantiated with theoretical calculations, the degradation pathways of amoxicillin in the UV/H_2O_2 and UV/PS systems were proposed, including hydroxylation (+16 Da), hydrolysis (+18 Da), and decarboxylation (-44 Da). The frontier electron density of amoxicillin was calculated to predict the susceptible regions for $HO^{\bullet}$ and $SO_4^{\bullet-}$ attack. The antibacterial activity of amoxicillin solution decreases significantly after applying UV/H_2O_2 or UV/PS processes.

In the third part of this study, QSPR method was developed to model the second-order hydroxyl radical and sulfate radical rate constants ($k_{HO^{\bullet}}$ and $k_{SO_4^{\bullet-}}$) for a wide range of micropollutants. The modeling was conducted by a sequential process of data collection, descriptor filtration, model optimization, and model validation. 128 micropollutants were collected from the published papers and randomly divided into the training, validation, and test set. 5286 descriptors were generated from the software to develop the model. Multiple linear regression (MLR) models show low predictivity in this study. In comparison, artificial neural network (ANN) and deep neural network (DNN) models can predict the dataset accurately. Three descriptor filtration approaches were evaluated and compared, including non-dimension-reduction approach, correlation analysis approach, and principal component analysis approach. The most predictive models were validated using application domain and visualized in the Williams plot. With outliers identified and removed, the $k_{HO^{\bullet}}$ and $k_{SO_4^{\bullet-}}$ models developed in this study show good robustness and high reliability, indicating that ANN and DNN methods can be used to evaluate the degradation of

micropollutants by $HO^{\bullet}$ and $SO_4^{\bullet-}$ in water. The selected descriptors for $k_{HO^{\bullet}}$ model indicate three reaction pathways for $HO^{\bullet}$ oxidation with chemicals, namely hydrogen atom abstraction, radical addition, and electron transfer. In comparison, the electrophilic radical $SO_4^{\bullet-}$ tends to react with electron-rich moiety groups directly through electron-transfer mechanism.

Table of Contents

LIST OF PUBLICATIONS

A. Journal articles

1. Zhang, Y.; Zhang, J.; Xiao, Y.; Chang, V.W.C.; Lim, T.T. **2016**. Kinetic and mechanistic investigation of azathioprine degradation in water by UV, UV/H_2O_2 and UV/persulfate. ***Chemical Engineering Journal***, 302, 526-534.

2. Zhang, Y.; Zhang, J.; Xiao, Y.; Chang, V.W.C.; Lim, T.T. **2017**. Direct and indirect photodegradation pathways of cytostatic drugs under UV germicidal irradiation: Process kinetics and influences of water matrix species and oxidant dosing. ***Journal of Hazardous Materials***, 324, 481-488.

3. Zhang, Y.; Zhang, J.; Xiao, Y.; Chang, V.W.C.; Lim, T.T. **2017**. Degradation of cyclophosphamide and 5-fluorouracil in water using UV and UV/H_2O_2: Kinetics investigation, pathways and energetic analysis. ***Journal of Environmental Chemical Engineering***, 5, 1133-1139.

4. Zhang, Y.; Xiao, Y.; Zhong, Y.; Lim, T.T. **2019**. Comparison of amoxicillin photodegradation in the UV/H_2O_2 and UV/persulfate systems: Reaction kinetics, degradation pathways, and antibacterial activity. ***Chemical Engineering Journal***, 372, 420-428.

5. Zhang, Y.; Zhang, Y.; Xiao, Y.; Lim, T.T. QSPR prediction for the hydroxyl and sulfate radical oxidation of micropollutants using artificial neural networks. Under review.

6. Zhang, Y.; Zhang, Y.; Xiao, Y.; Lim, T.T. UV direct photolysis of halogenated disinfection byproducts: Experimental study and QSPR modeling. Under review.

B. Conference contributions

1. Zhang, Y.; Lim T.T. **2015**. Degradation of mixed cytostatic drugs by UV, UV/H_2O_2 and UV/PS, oral presentation, IWA Micropol & Ecohazard Conference, 22-26, November, Singapore.

2. Zhang, Y.; Lim T.T. **2018**. Photodegradation of amoxicillin by UV, UV/H_2O_2 and UV/PS: reaction kinetics, degradation pathways and antibacterial activity, oral presentation, 10th European meeting on Solar Chemistry and Photocatalysis: Environmental Applications (SPEA10), Spain, June, Spain.

C. Book chapter

1. Zhang, Y., Lim, T.T. **2018**. Chapter 12 Photodegradation of cytostatic drugs in low-pressure UV photoreactor through direct and indirect pathways. In Fate and Effects of Cytostatic Pharmaceuticals in the Environment. Eds. Heath E., Filipič M., Kosjekw T., Isidori M. In press. Springer.

LIST OF TABLES

LIST OF FIGURES

LIST OF ABBREVIATIONS

AD: applicability domain

ANN: artificial neural network

AOP: advanced oxidation process

AZA: azathioprine

AMX: amoxicillin

CA: correlation analysis

CP: cyclophosphamide

Cost/O: cost per order

CSDs: cytostatic drugs

CYT: cytarabine

DNN: deep neural network

DOX: doxorubicin

FLU: flutamide

5FU: fluorouracil

LC-MS/MS: liquid chromatography tandem mass spectrometry

MET: methotrexate

MLR: multiple linear regression

MIT: mitotane

m/z: mass-to-charge ratio

NDR: non-dimension-reduction

NOM: natural organic matter

PCA: principal component analysis

PS: persulfate

QSPR: quantitative structure-property relationship

TOC: total organic carbon

STP: sewage treatment plant

LIST OF SYMBOLS

ε_{254}: molar absorption coefficient (M^{-1} cm^{-1})

Φ_{254}: quantum yield (mol E^{-1})

C_0: chemical concentrations before degradation (M)

C: chemical concentrations after degradation (M)

C-001: number of CH_3R or CH_4

C-016: number of functional group =CHR

E_{homo}: energy of highest occupied molecular orbital

E_{lomo}: energy of lowest unoccupied molecular orbital

$f(+)_x(e)$: maximum of nucleophilic attack

$f(+)_n(e)$: minimum values of nucleophilic attack

$f(-)_x(e)$: maximum values of electrophilic attack

$f(-)_n(e)$: minimum values of electrophilic attack

$f(0)_x(e)$: maximum values of $HO^{\bullet}$ attack

$f(0)_n(e)$: minimum values of $HO^{\bullet}$ attack

hc/λ: energy of photon at wavelength λ (kJ E^{-1})

HLG: gap between E_{homo} and E_{lumo}

I_0: average photonic intensity per volume (E L^{-1} s^{-1})

I_E: UV intensity (mW cm^{-2})

IC3: information content index (neighborhood symmetry of 3-order)

K_{ow}: octanol-water partition coefficient

k_t: time-based first-order rate constant (min^{-1})

k_f: fluence-based first-order rate constant (cm^2 mJ^{-1})

L: optical path length (cm)

Me: mean of atomic Sanderson electronegativity (scaled on C atom)

MLogP: Moriguchi octanol-water partition coefficient

N%: percentage of nitrogen

nHM: number of heavy atoms

nRNHR: number of secondary amines (aliphatic)

nRSR: number of sulfides

pH: $-\lg[H^+]$

piPC03: molecular multiple path count of order 3

pK_a: acid dissociation constant

q: photon flux ($E\ s^{-1}\ cm^{-2}$)

$qH^+(e)$: maximum value of most positive partial charge on a H atom

$q(C)_{min}(e)$: minimum value of most negative partial charge on a main-chain C atom

$q(C)_{max}(e)$: maximum value of most negative partial charge on a main-chain C atom

R^2: correlation coefficient

Sp: sum of atomic polarizabilities (scaled on C atom)

$T_{1/2}$: half-life (min)

t: degradation time (min)

μ(Debye): dipole moment

Chapter 1 Introduction

1.1 Background

Due to the rising life expectancy and declining fertility rates, population aging has emerged as a major social concern especially in the developed countries. The increasing risk of aging-related diseases has led to an ever-growing consumption of various pharmaceuticals and attracted public concern and scientific interest. Based on their therapeutic use, pharmaceuticals can be classified into groups such as cytostatic drugs (CSDs), antibiotics, antidepressant, analgesics, antidiabetic, antiepileptics, etc (Kovalova et al., 2012). Among these pharmaceuticals, special attention has been made to the presence of CSDs and antibiotics due to their frequent usage and high toxicity.

CSDs are a broad group of carcinogenic, mutagenic and teratogenic pharmaceuticals used in chemotherapy of cancer, treatment of skin diseases and treatment of infections. They can be further divided into several sub-groups based on their therapeutic action, including alkylating agents, antimetabolites, plant alkaloids, cytotoxic antibiotics, and other antineoplastic agents (Kosjek and Heath, 2011; Ocampo-Pérez et al., 2010). Over 100 kinds of CSDs are currently in use or being developed. Large-scale European Union Framework Program 7 projects such as Cytothreat (http://www.cytothreat.eu) have focused on investigating the human health and environmental effects of these CSDs. Antibiotics are another family of pharmaceuticals developed for inhibiting or killing microorganisms and extensively used in human and veterinary medicine. Amoxicillin (AMX), as a significant broad-spectrum and semi-synthetic penicillin, has been reported as the most consumed antibiotic used in European countries, India, Brazil, etc (Andreozzi et al., 2004).

Due to the lack of control, these pharmaceuticals have been directly discharged into hospital wastewater or domestic sewage through irresponsible disposal. The

detection of CSDs in various water bodies has been frequently reported worldwide from sub-ng to μg L^{-1}. Large hospitals and specialized cancer treatment center are the key emission points of these anticancer medicines (Parrella et al., 2014). In addition, AMX has also been detected in raw sewage, wastewater treatment plant effluents, and even surface waters (Hirte et al., 2016).

Once discharged into sewer, the fate and behavior of these pharmaceuticals are significantly influenced by their environmental stability. A study of 26 CSDs in the aqueous solutions indicate that most of the investigated CSDs are considerably recalcitrant in wastewater system due to their high biochemical and photochemical stability (Negreira et al., 2014). It has also been reported that 80-90% of AMX can be discharged into the effluent as unchanged form due to its poor metabolism in the organism (Dodd et al., 2010; Karlesa et al., 2014; Kıdak and Şifa, 2018; Pereira et al., 2014).

Due to their high toxicity, the presence of pharmaceuticals potentially in aquatic environment exerts adverse effects on the ecosystem and human health even at trace levels. People who are occupationally exposed to the anticancer drugs can suffer from a high risk of developing cancer. In addition, the beta-lactam ring of AMX can inhibit the cross-linkage between the linear peptidoglycan polymer chains of the bacteria cell wall, leading to the propagation of beta-lactam resistant bacteria in the environmental matrices (Jung et al., 2012; Martinez, 2009; Michael-Kordatou et al., 2015).

1.2 Motivation and knowledge gap

Given the frequent usage, continuous discharge, high persistence, and detrimental environmental impacts, it is essential to remove these micropollutants from the contaminated water by water and wastewater treatment processes. However, most biorefractive pharmaceuticals cannot be effectively removed by the conventional water and wastewater treatment technologies. Kovalova et al. (2012) assessed the degradation effect of cyclophosphamide in hospital wastewater using

MBR treatment method, and merely obtained a removal efficiency of less than 20%. It has also been reported that conventional wastewater treatment processes may promote the spread of antibacterial resistant genes of AMX, based on the detection of an increasing proportion of beta-lactam resistant organisms (Karlesa et al., 2014). In addition, some conventional treatment methods such as chlorination, bromination, and ozonation can lead to a potential formation of carcinogenic disinfection byproducts (DBPs) or intermediates. As a result, it is of great significance to develop alternative approaches to remove pharmaceuticals from the aquatic environment.

UV photolysis has been applied as a post-treatment process to disinfect pathogen and remove organic compound in water treatment plant. Organic compounds can absorb UV light at a certain wavelength, which leads to the destruction of the chemical bond and subsequent photolysis. UV-based advanced oxidation processes (UV/AOPs) have been regarded as more promising treatment processes due to the generation of highly oxidizing radicals. Compared with direct UV photolysis, UV/AOPs can remove pharmaceuticals completely within shorter reaction time (Wols and Hofman-Caris, 2012). For example, UV/H_2O_2 process can generate hydroxyl radical ($HO^{\bullet}$), which can react with organic compounds non-selectively through electron transfer, hydrogen abstraction and electrophilic addition reactions. In the recent decades, UV/persulfate ($S_2O_8^{2-}$, PS) process has gained more attention due to the generation of sulfate radical ($SO_4^{\bullet-}$), which can react with chemicals selectively through electron transfer reactions. However, the degradation of CSDs and AMX by UV/H_2O_2 and UV/PS processes has been seldom investigated. In addition, most studies focused on the reaction kinetics, while few investigated the degradation mechanism and antibacterial activity.

Due to the huge expenditure, experimental measurement on the degradation efficiency of various pharmaceuticals by UV/AOPs is difficult, leading to a considerable lag of available data. As a result, developing a reliable model using the

existing data to predict the emerging micropollutants is of scientific and practical significance. Quantitative structure-property relationship (QSPR) method has been widely investigated as an alternative modelling approach to establish relationships between the properties of compounds and their structural characteristics. Artificial neural network (ANN), inspired by the biological neural network of animal brains, has been applied in a wide range of disciplines since the 1990s. Recently, deep neural networks (DNNs), namely ANN with more than one hidden layer, have received increasing attention in the field of artificial intelligence and machine learning. The predictivity of ANN models can be further improved by multiple hidden layers (Ma et al., 2015; Song et al., 2017; Winkler and Le, 2017). However, to our knowledge, no attempt has been made to predict the degradation efficiency of micropollutants using DNN approach.

1.3 Objective and scope of works

The aim of this study is to investigate the photodegradation of micropollutants in water by direct UV photolysis, UV/H_2O_2, and UV/PS processes, and to establish QSPR models to predict the second-order rate constant of various micropollutants with $HO^{\bullet}$ and $SO_4^{\bullet-}$.

The scope of works is described as follows.

i. To investigate the direct and indirect UV photolysis of CSDs.

- Evaluate the degradation efficiency of eight CSDs by direct UV photolysis, UV/H_2O_2, and UV/PS processes.
- Investigate the effect of water matrix species in each process.
- Compare the degradation efficiency of CSDs in different water types.
- Propose direct and indirect degradation pathways of CSDs in each process.

ii. To compare the reaction kinetics, degradation pathways, and antibacterial activity of AMX photodegradation by UV/H_2O_2 and UV/PS processes.

- Compare the reaction kinetics of AMX by different approaches.

- Investigate the degradation pathways of AMX in each process.
- Evaluate the antibacterial activity change of AMX in each process.

iii. To establish QSPR models to predict the second-order rate constants of micropollutants with radicals.

- Collect the dataset from the publications and software.
- Reduce the descriptors using various descriptor filtration methods.
- Optimize QSPR models using various algorithm methods.
- Validate the developed QSPR models using Williams plot approach.

1.4 Structure of thesis

Chapter 1 briefly introduces the introduction to the background, motivation and knowledge gap, objectives and scopes, as well as the structure of thesis. Chapter 2 reviews the physicochemical properties, the predicted environmental behaviors, the occurrence in the aquatic environment, the human risk and ecotoxicological potency, the advanced wastewater treatment processes of CSDs. It also presents the fundamentals of UV direct and indirect photolysis, as well as the procedures of QSPR. Chapter 3 describes the chemicals, water samples, experimental procedures, analytical methods, antibacterial activity tests, and computational calculations used in this thesis. Chapter 4 investigates the degradation effect of eight CSDs by direct and indirect UV photolysis. Chapter 5 focuses on comparing UV/H_2O_2 and UV/PS processes for AMX degradation, including reaction kinetics, degradation pathways, and antibacterial activity. Chapter 6 develops QSPR models to estimate $k_{HO^{\bullet}}$ and $k_{SO_4^{\bullet-}}$ for a wide range of micropollutants, using a sequential process of data collection, descriptor filtration, model optimization, and model validation. Chapter 7 outlines the major conclusions from this study and recommendations for the future work.

Chapter 2 Literature review

2.1 Pharmaceuticals

2.1.2 Physicochemical properties

Table 2.1 compares the physicochemical properties of nine representative pharmaceuticals investigated in this study, including azathioprine (AZA), cyclophosphamide (CP), cytarabine (CYT), doxorubicin (DOX), fluorouracil (5FU), flutamide (FLU), methotrexate (MET), mitotane (MIT), and amoxicillin (AMX). Their information was collected from several databases such as PubChem (http://pubchem.ncbi.nlm.nih.gov/), Drug Bank (http://www.drugbank.ca/), and ChemSpider (http://www.chemspider.com/). As can be seen, there is a great diversity of their physicochemical properties, including their molecular weight (MW), molecular structure, dissociation constant (pKa), solubility, octanol-water partition coefficient (K_{ow}), and Henry's Law constant.

The properties of pharmaceuticals can influence their fate and distribution in the aquatic environment to some extent. Pharmaceuticals with low vapor pressure can be distributed in aquatic environment or solid waste, while pharmaceuticals with low dissociation constant can be dissociated into ionic forms under normal circumstances. For example, with a low octanol-water partition coefficient (log K_{ow} = -0.89) and a relatively high dissociation constant (pK_a = 8), 5FU shows high mobility in infiltrating water and low sorption to solids in water. In addition, with high water solubility of 272 mg L^{-1} and low log K_{ow} of 0.1, AZA can remain soluble in the aquatic environment, leading to the potential health and environmental risks (Fazio et al., 2007).

Table 2.1 The physicochemical properties of nine investigated pharmaceuticals

Compound	Molecule	MW (g mol^{-1})	Structure	pK_a	Water solubility (mg L^{-1})	Log K_{ow}	Henry's Law Constant (atm m^3 mol^{-1})
AZA	$C_9H_7N_7O_2S$	277	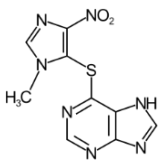	8.2	272	0.1	2.64×10^{-15}
CP	$C_7H_{15}Cl_2N_2O_2P$	260	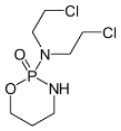	2.8	4×10^{4}	0.63	1.40×10^{-11}
CYT	$C_9H_{13}N_3O_5$	243	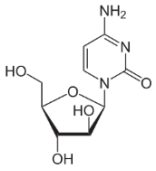	4.22	1.76×10^{4}	-1.82	1.57×10^{-19}
DOX	$C_{27}H_{29}NO_{11}$	544	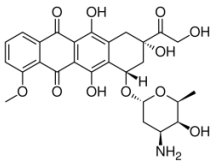	8.2	92.8	1.27	2.23×10^{-23}
5FU	$C_4H_3FN_2O_2$	130	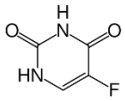	8.0	1.11×10^{4}	-0.89	1.66×10^{-10}
FLU	$C_{11}H_{11}F_3N_2O_3$	276	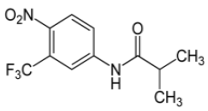	13.1	9.45	3.35	3.73×10^{-10}
MET	$C_{20}H_{22}N_8O_5$	454	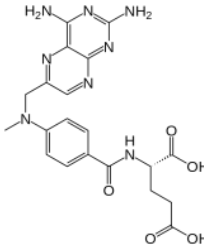	4.7	2600	-1.85	1.54×10^{-31}
MIT	$C_{14}H_{10}Cl_4$	322	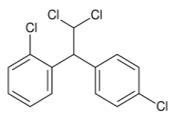	n.a.	0.1	5.87	8.17×10^{-6}
AMX	$C_{16}H_{19}N_3O_5S$	365	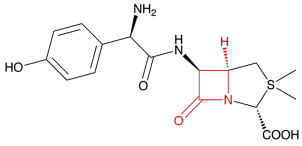	3.23, 7.43	3430	0.87	2.49×10^{-21}

2.1.2 Occurrence in the aquatic environment

Besides physicochemical properties, the occurrence of pharmaceuticals in the aquatic environment can be also influenced by their annual consumption at regional or national scale, discharge by the hospitals and patients, dilution factor and environmental distribution, excretion rate and metabolites, sewage treatment plants (STP) removal efficiency and tertiary treatments, etc. It is imperative to investigate the environmental behaviors and fates of these pharmaceuticals before conducting a risk assessment or making corresponding policies. A modelling method to evaluate their predicted environmental concentration has been widely applied (Andreozzi et al., 2004). As prescription drugs, the population-related parameters such as annual consumption can be approximately estimated, except for some overestimation caused by the unknown transformation processes in aquatic environment. Other factors with regards to degradation efficiency can be further investigated to provide a fine-scale estimation for local and hot spots of pharmaceuticals contamination.

Due to the increasing consumption, continuous discharge, and lack of effective treatment processes, a large number of pharmaceuticals have been detected at ng L^{-1} or μg L^{-1} level at natural water bodies. As shown in **Table 2.2**, CP has been most frequently detected in hospital wastewater, STP influent or effluent, as well as surface water of various countries, which indicate its prevalence worldwide. 5FU has been detected at up to hundreds of μg L^{-1} level in the hospital effluents of Austria, which implies its high consumption and low removal efficiency (Mahnik et al., 2007).

Table 2.2 Detection of pharmaceuticals in aquatic environment (ng L^{-1}).

CSDs	Hospital effluent	STP influent	STP effluent	Receiving surface water	Country	Ref
AZA	9-32	-	-	-	China	(Yin et al., 2010)
	-	-	11.8	0.45	Catalonia	(Franquet-Griell et al., 2015)
	14.5-187.9	18.2-19.1				(Ferrando-Climent et al., 2013)
CP	-	-	-	1.74	France	(Besse et al., 2012)
	-	-	70.2	-	UK	(Rowney et al., 2009)
	-	-	-	4.1	UK	(Booker et al., 2014)
	-	-	-	0.60	Germany	(Kümmerer and Al-Ahmad, 2010)
	-	-	-	4.35	Spain	(Ortiz et al., 2013)
	-	-	-	4.56	Spain	(Martín et al., 2014)
	-	-	-	0.11	Catalonia	(Franquet-Griell et al., 2015)
	146	-	-	-	Germany	(Steger-hartmann et al., 1996)
	19-4486	<6-143	<6-17	-	Germany	(StegerHartmann et al., 1997)
	-	-	<10-20	<10	Germany	(Ternes, 1998)
	-	-	0.6	<0.0074	Italy	(Calamari et al., 2003)
	-	2-11	2-11	0.15-0.17	Switzerland	(Buerge et al., 2006)
	-	-	-	<30-64.8	Romania	(Moldovan, 2006)
	<2-21	<2	<2	-	Norway	(Thomas et al., 2007)
	-	-	<125	<100	Australia	(Busetti et al., 2009)
	6-2000	-	-	-	China	(Yin et al., 2010)
	-	<2.1	<2.3	<1.7	Spain	(Martín et al., 2011)
	-	-	0.19-0.37	-	UK	(Llewellyn et al., 2011)
	0.161	-	-	-	Switzerland	(Kovalova et al., 2012)
	5730	<3.1-13,100	<3.1	-	Spain	(Gómez-Canela et al., 2012)
CYT			0.19	0.01	Catalonia	(Franquet-Griell et al., 2015)
		9.2	14	13	Spain	(Martín et al., 2011)
DOX		4.5	<4.3	<5.3	Spain	(Martín et al., 2011)
				0.19	France	(Besse et al., 2012)
			0.343		UK	(Rowney et al., 2009)
				0	UK	(Booker et al., 2014)
				0.16	Spain	(Martín et al., 2014)
			0.17	0.01	Catalonia	(Franquet-Griell et al., 2015)

	<260-1350	-	-	-	Australia	(Mahnik et al., 2007)
	<10	-	-	-	China	(Yin et al., 2010)
5FU	-	-	-	7.91	France	(Besse et al., 2012)
	-	-	-	0.90	UK	(Booker et al., 2014)
	-	-	-	44.1	Spain	(Martín et al., 2014)
	-	-	-	0.01	Catalonia	(Franquet-Griell et al., 2015)
	20,000-122,000	-	-	-	Austria	(Mahnik et al., 2004)
	<15	<15	<15	-	Switzerland	(Tauxe-Wuersch et al., 2006)
	<8600-123,500	-	-	-	Austria	(Mahnik et al., 2007)
	<5-27	-	-	-	Switzerland	(Kovalova et al., 2009)
	-	<38	<21	<34	Spain	(Martín et al., 2011)
FLU	-	-	-	<1.19	France	(Besse et al., 2012)
	-	-	-	0.646	Spain	(Ortiz et al., 2013)
	-	-	-	0.72	Catalonia	(Franquet-Griell et al., 2015)
MET	-	-	-	1.54	France	(Besse et al., 2012)
	-	-	-	0.20	UK	(Booker et al., 2014)
	-	-	-	0	Spain	(Martín et al., 2014)
	-	-	1.10	0.04	Catalonia	(Franquet-Griell et al., 2015)
	-	-	0	<0.044	Italy	(Calamari et al., 2003)
	4-4689	-	-	-	China	(Yin et al., 2010)
	-	<0.1	<0.1	<0.1	Spain	(Martín et al., 2011)
MIT				3.20	France	(Besse et al., 2012)
	-	-	-	0	UK	(Booker et al., 2014)
	-	-	1.32	0.05	Catalonia	(Franquet-Griell et al., 2015)
AMX	-	-	120	-	Italy	(Andreozzi et al., 2004)
	-	-	127.49	-	South Korea	(Kim et al., 2018)
	-	-	280	-	Australia	(Watkinson et al., 2007)

2.1.3 Human risk and ecotoxicological potency

As a broad group of carcinogenic, mutagenic and teratogenic pharmaceuticals, CSDs show detrimental effects on human health or aquatic organisms even at trace levels. CSDs can exhibit adverse effects to the non-target healthy cell, giving rise to undesirable damage to human health. People who suffer from long-term exposure of CSDs may have a high risk of cancer. The preparation and administration of CSDs

induce the structural chromosomal aberrations among occupational medicine nurses (Zhang et al., 2013). In addition, some CSDs are able to restrain DNA synthesis process and suppress cell replication system. For example, AZA has been produced to decrease the risk of organ rejection through suppressing the body's immune system and widely applied in organ transplantation and autoimmune diseases (Lakshmi and Reddy, 1998; Shahrokhian and Ghalkhani, 2009). However, it shows extremely high toxicity by giving rise to severe drug side-effects, such as nausea, fatigue, hair loss and blood disorders. These side-effects commonly occur at the beginning of a treatment, which are met with taking AZA after meals or transient intravenous administration (Göğer et al., 1999; Shahrokhian and Ghalkhani, 2010; Singh et al., 1988).

Though it has been also reported that the long-time exposure to CSDs and their additives can potentially jeopardize the ecosystem, there is a lack of specific regulation and strict control with regard to the CSDs discharge into the real water bodies. Limited environmental risk assessment information is available for the CSDs at this moment, thus the acquired toxicological data are commonly evaluated according to the short-term toxicological experiments of individual pharmaceutical on the aquatic organisms. More efforts should be carried out with regard to the ecotoxicological potency of long-lived exposure to CSDs (Zhang et al., 2013).

2.1.4 Wastewater treatment processes

Conventional wastewater treatment processes may exhibit low removal efficiency towards pharmaceuticals. Therefore, developing effective approaches to remove these biorefractive and recalcitrant pharmaceuticals from contaminated water is urgently required. Advanced wastewater treatment technologies have been investigated for removing pharmaceuticals as shown in **Table 2.3**, such as membrane bioreactor (MBR), electrolysis, ozonation and UV-based technologies.

MBR technology combines membrane filtration with a conventional biological-

activated sludge process as a unified system for secondary wastewater treatment. Mahnik et al. (2007) indicated that FLU and DOX in hospital effluent could be removed effectively using a pilot-scale MBR system through biodegradation and/or adsorption. However, MBR technology becomes inefficient towards less biodegradable CSDs. For example, a low removal rate of 20% for CP degradation was observed in hospital effluent using MBR technology (Kovalova et al., 2012).

Due to the generation of hypochlorite from sodium chloride, electrolysis has been applied to inactivate microorganisms and degrade chemicals. Thus, the cytotoxicity, mutagenicity and antibacterial activity of MET in hospital wastewater could be removed completely within 6 h by electrolysis process (Hirose et al., 2005). However, human carcinogens such as trihalomethanes could be accumulated during the electrolysis process (Zhang et al., 2013).

Ozonation process includes both direct and indirect reactions with the compounds present in aquatic environment. Direct ozonation process can degrade organic compounds efficiently by reacting with their unsaturated bonds. It has been indicated that direct ozonation process could degrade MET and DOX, with second-order rate constants of 0.0267 and 0.3373 min^{-1}, respectively (Somensi et al., 2012). In addition, it has also been reported that direct ozonation process could remove MET from contaminated water efficiently with second-order rate constant of more than 3.6×10^3 M^{-1} s^{-1}, while higher ozone dose and longer reaction time were required for cyclophosphamide degradation with second-order rate constant of 3.3 ± 0.2 M^{-1} s^{-1} (Garcia-Ac et al., 2010). Recently, indirect ozonation processes have been investigated due to the generation of highly effective radicals. Free $HO^{\bullet}$ can be generated through the process and react with compounds effectively, but ozonation is highly affected by the pH and NOM of the water matrix. In addition, the disinfection by-products can also be generated during ozonation process, such as bromate, haloacetaldehydes, and halonitromethanes.

Table 2.3 Removal of pharmaceuticals using advanced wastewater treatment technologies.

Methods	Pharmaceuticals	Matrices	Water treatment / mechanism	Ref
MBR	FLU, DOX, CP	Domestic wastewater, hospital wastewater	Combination of biological treatment and membrane filtration.	(Kovalova et al., 2012; Mahnik et al., 2007)
Electrolysis	MET	Clinic wastewater, urine	Generation of hypochlorite	(Hirose et al., 2005)
Ozonation	CP, MET, DOX, AMX	Deionized water, biologically treated water, drinking water	Selective reaction with unsaturated bonds	(Andreozzi et al., 2005; Garcia-Ac et al., 2010; Kim and Tanaka, 2009; Somensi et al., 2012)
UV photolysis	AZA, CP. CYT, DOX, FLU, 5FU, MET, MIT, AMX	Deionized water	Homolytic bond cleavage	(Jung et al., 2012; Lutterbeck et al., 2016; Miolo et al., 2011; Zhang et al., 2017b)
UV/H_2O_2	AZA, CP, 5FU, AMX	Deionized water, tap water, pre-treated water	Hydrogen abstraction, electron transfer, and electrophilic addition	(Jung et al., 2012; Lutterbeck et al., 2015; Wols et al., 2013; Zhang et al., 2016, 2017a)
UV/PS	AZA	Deionized water	Electron transfer	(Zhang et al., 2016)
UV/O_3	AMX	Deionized water	Hydrogen abstraction, electron transfer, and electrophilic addition	(Moreira et al., 2015)
UV/TiO_2	CP, FLU, AMX	Deionized water	Hydrogen abstraction, electron transfer, and electrophilic addition	(Dimitrakopoulou et al., 2012; Lin and Lin, 2014; Lutterbeck et al., 2015)

2.2 UV treatment technologies

2.2.1 Direct UV photolysis

Conventional water treatment methods are often chemically, operationally, and energy intensive. As a result, UV photolysis has been widely investigated as an alternative technology. UV light is a type of electromagnetic radiation, with a wavelength of 10 to 400 nm. The most common objective of UV technology is to achieve water and air quality standards regulated by the corresponding agencies according to emission ordinances. It has been used in many water treatment plants and wastewater treatment plants to degrade micro-pollutants and control pathogens in water, leading to an efficient water detoxification, disinfection or purification. As a chemical-free technology, UV technology does not require hazardous chemical, nor generate harmful disinfection byproducts. It does not influence the aesthetic quality (e.g., taste and odor) of the treated water, as compared with other process such as chlorination or ozonation (Bolton and Stefan, 2002).

Direct UV photolysis is a process in which organic compounds are able to absorb UV light at a certain wavelength, giving rise to the photocleavage of the chemical bond and subsequent breakdown of the chemical. A molecule with ground state (RX) can be prompted to its electronically excited state ($RX^{\bullet}$) (Equation 2.1), and then react with the present molecular oxygen to form corresponding photoproducts (Equation 2.2). Carbon atoms can be converted into CO_2 or carbonate species such as H_2CO_3, HCO_3^- and CO_3^{2-}, while hydrogen atoms can be transformed into H_2O through complete mineralization.

$$RX + h\nu \rightarrow RX^{\bullet} \rightarrow R^{\bullet} + X^{\bullet} \quad (2.1)$$

$$R^{\bullet} + O_2 \rightarrow RO_2^{\bullet} \rightarrow \text{photoproducts} \quad (2.2)$$

2.2.2 Kinetic analysis

Applying the pseudo first-order kinetics to the UV photolysis reactions, the degradation efficiency of a chemical can be described below (Equations 2.3 and 2.4).

$$-dC/dt = kC \tag{2.3}$$

$$\ln(\frac{C_0}{C}) = kt \tag{2.4}$$

where k is the time-based first-order rate constant (min^{-1}), t is the degradation time (min), C_0 and C are the chemical concentrations before and after degradation (M), respectively.

The photolysis rate of a chemical highly depends on its molar absorption coefficient and quantum yield. The molar absorption coefficient (ε_{254}, $M^{-1}\cdot cm^{-1}$) measures the probability that a chemical absorbs light at UV-254 nm. Quantum yield (Φ_{254}, mol E^{-1}), the ratio of photons that photocleave the compound normalized by the number of photons absorbed at wavelength 254 nm, can be calculated according to Beer-Lambert Law (Equation 2.5):

$$\Phi_{254} = \frac{-dC/dt}{I_0 \times (1-10^{-\varepsilon_{254}LC})} \tag{2.5}$$

where I_0 is the average photonic intensity per volume (E L^{-1} s^{-1}), L is the optical path length (cm), C is the concentration (M) of compound.

$10^{-\varepsilon_{254}LC}$ can be expanded according to Taylor expansion as shown in Equation 2.6.

$$10^{-\varepsilon_{254}LC} = 1 + \frac{10^{-\varepsilon_{254}LC} \times \ln 10 \times (-\varepsilon_{254}LC)}{1!} + \frac{10^{-\varepsilon_{254}LC} \times (\ln 10)^2 \times (-\varepsilon_{254}LC)^2}{2!} + \ldots \tag{2.6}$$

When the compound concentration C is low enough, which leads to a low UV absorbance ($A = \varepsilon_{254}LC < 0.02$), Equation 2.5 can be simplified as

$$10^{-\varepsilon_{254}LC} = 1 + \frac{1 \times 2.303 \times (-\varepsilon_{254}LC)}{1!} + \frac{1 \times (2.303)^2 \times (-\varepsilon_{254}LC)^2}{2!} + \ldots \approx 1 - 2.303\varepsilon_{254}LC \tag{2.7}$$

Therefore, Equation 2.5 can be expressed as:

$$\Phi_{254} = \frac{-dC/dt}{2.303 I_0 \varepsilon_{254} LC} = \frac{-dC/dt}{2.303 q \varepsilon_{254} C} \tag{2.8}$$

where q ($=I_0L$) is the photon flux (E s^{-1} cm^{-2}).

Rearranging Equations 2.3 and 2.8 becomes

$$\Phi_{254} = \frac{k}{2.303 q \varepsilon_{254}} \tag{2.9}$$

2.2.3 UV-based AOPs

Despite the numerous advantages of UV technology, there are certain pharmaceuticals which are stable towards direct UV photolysis. UV-based AOPs are promising advanced water treatment approaches to degrade these recalcitrant pharmaceuticals. UV light can work synergistically with oxidants to generate reactive oxidative radicals such as HO•. The overall photodegradation of target compounds by indirect UV-based AOPs involve the direct UV photolysis, as well as the radical-induced indirect photolysis. The most frequently applied UV-based AOPs to degrade pharmaceuticals include UV/H_2O_2, UV/PS, UV/O_3, UV/TiO_2, etc.

UV/H_2O_2 takes advantage of the homolytic bond cleavage of the O-O bond in H_2O_2, which can lead to the formation of HO• radicals. Non-selective HO• can be promptly generated from H_2O_2 by absorbing UV irradiation at wavelength from 200 nm to 280 nm, which attacks various organic compounds through electron transfer, hydrogen abstraction or electrophilic addition reactions (Baxendale and Wilson, 1957). Due to the high oxidative efficiency of HO•, UV/H_2O_2 has been widely applied in pathogen disinfection and chemical degradation. In addition, as an environmental-friendly approach, UV/H_2O_2 produces negligible oxidation byproducts. However, the degradation efficiency of UV/H_2O_2 is significantly affected by the presence of natural organic matters (NOM) or inorganic anions. In addition, H_2O_2 is relatively expensive and not readily applied at wastewater treatment plants.

$$\text{H-O-O-H} + h\nu \rightarrow 2\text{HO}^{\bullet} \tag{2.10}$$

More recently, UV/PS has also attracted a broad attention in pharmaceutical degradation due to the generation of $SO_4^{\bullet}$ and moderate stability of PS. PS can be homolytically cleaved by UV activation, which primarily generates highly reactive

$SO_4^{\bullet-}$ (Mark et al., 1990). PS has a higher radical production yield (1.4-1.8 mol E^{-1}) compared to H_2O_2 (1.0 mol E^{-1}) (Baxendale and Wilson, 1957), while $SO_4^{\bullet-}$ has a higher oxidizing power (2.5-3.1 V) than that of $HO^{\bullet}$ (2.15-2.8 V) especially at higher pH values. Therefore, UV/PS has been reported to be more effective than $HO^{\bullet}$ in removing specific organic pollutants, such as cyanotoxin cylindrospermopsin (He et al., 2013), antipyrine (Tan et al., 2013), and atrazine (Khan et al., 2014). In addition, UV/PS is less affected by the common water matrix species in the natural water, since it's more selective for electron transfer reactions. However, UV/PS may generate higher potential of oxidation byproducts compared with UV/H_2O_2.

$$^{-}SO_3\text{-}O\text{-}O\text{-}SO_3^{-} + h\nu \rightarrow 2SO_4^{\bullet-} \quad (2.11)$$

For the UV/O_3 process, UV irradiation can result in a cleavage of dissolved ozone, followed by a fast reaction of atomic oxygen with water to form a thermally excited H_2O_2. Subsequently, the excited peroxide decomposes into two $HO^{\bullet}$ (Equations 2.12-2.15). When aqueous ozone is exposed to UV light, it is very efficiently photolyzed to form an exited O atom ($O(^1D)$) which adds to H_2O to form H_2O_2. Ozone has a molar extinction coefficient of 3300 M^{-1} cm^{-1} at 254 nm, which is significantly higher than that of H_2O_2 at this particular wavelength. Direct oxidation by the combination of ozonation and photolysis covers a wide range of pharmaceuticals reactivity and leads to the main advantage of this process. However, due to the cage recombination, only a small proportion of generated H_2O_2 decomposes to $HO^{\bullet}$, resulting in a free $HO^{\bullet}$ quantum yield of only 0.1. Furthermore, both UV lamp and ozone generator need large amounts of electrical energy, resulting in relatively high energy demands for the combination of UV and ozone and low energy efficiency of radical generation.

$$O_3 + h\nu \rightarrow {}^1O_2 + O(^1D) \quad (2.12)$$

$$O(^1D) + H_2O \text{ (gas phase)} \rightarrow 2HO^{\bullet} \quad (2.13)$$

$$O(^1D) + H_2O \text{ (liquid phase)} \rightarrow H_2O_2 \quad (2.14)$$

$$H_2O_2 + 2O_3 \rightarrow 2HO^{\bullet} + 3O_2 \quad (2.15)$$

Over the past decades, heterogeneous photocatalysis based on semiconductors TiO_2 has been widely investigated for removing pharmaceuticals. TiO_2 is usually used as suspended colloidal particles or immobilized on different substrates. An electron is excited to the conduction band, leaving a positively charged hole (h^+) in the valence band (Equations 2.16-2.17). These species can cause oxidative or reductive transformations of water constituents, either directly on the semiconductor surface or via radical reactions. A sufficient amount of dissolved oxygen is necessary for the latter reactions. Advantages of UV/TiO_2 for pharmaceutical removal include low costs of the catalyst itself and easy commercial availability in various crystalline forms and particle characteristics. In addition, the catalyst TiO_2 is non-toxic and photochemically stable. However, the quantum yield of TiO_2 photocatalysis for oxidation and reduction of contaminants is usually very low (Φ = 0.04 mol E^{-1}) due to the fast recombination of electron-hole pairs. As a result, the process is rarely applied in industrial or municipal water treatment facilities because of the low quantum yield for $HO^{\bullet}$ production.

$$TiO_2 + h\nu \rightarrow (e^- + h^+) \quad (2.16)$$

$$h^+ + OH^- \rightarrow HO^{\bullet} \quad (2.17)$$

2.3 QSPR model

QSPR is considered as a regression or classification method used in the chemical sciences, which provides a universal relationship between observed reaction behavior and quantum chemical parameters. QSPR model relates the predictor variables to a categorical value of the response variable. By summarizing a supposed relationship between chemical structures and activity in a data-set of chemicals, QSPR model can deal with the existing data to predict the activities of the untested chemicals.

In recent studies, QSPR models have been widely applied to investigate the correlation between the degradation rate of the pollutants and their molecular

parameters. Kusić et al. (2009) developed a four-variable model to predict the second-order rate constant of 78 aromatic compounds with HO•. Xiao et al. (2014) developed a QSPR model to predict the direct UV photolysis efficiency of 9 trihalomethanes, indicating that the combination of bond strength, electronic effect and steric effect could present the optimized model with R^2=0.95. Generally, most of the researches focused on the compounds with similar structures, which showed limitation in water treatment application. Therefore, to develop a universal QSPR model for a variety of compounds is of great importance.

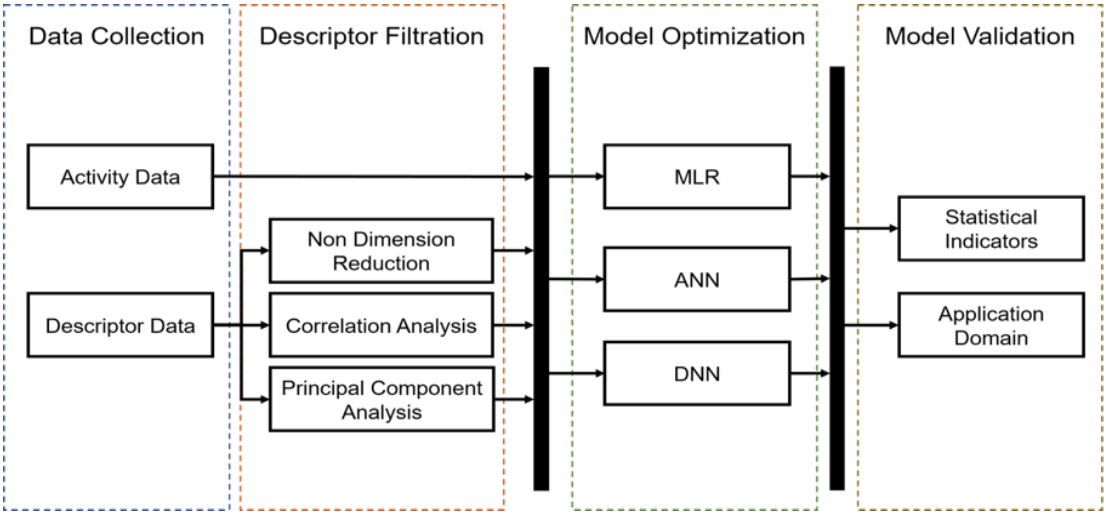

Figure 2.1 The principal steps of QSPR process.

QSPR modeling process consists of four principal steps, including data collection, descriptor filtration, model optimization, and model validation (**Figure 2.1**). The quality of a QSPR model is evaluated based on four criteria, i.e., the quality of input data, the choice of descriptors, the methods for modelling, and the methods for validation.

Table 2.4 The list of descriptors calculated by Dragon.

Block no.	Block name	Descriptors
1	Constitutional	47
2	Ring descriptors	32
3	Topological indices	75
4	Walk and path counts	46
5	Connectivity indices	37

6	Information indices	50
7	2D matrix-based descriptors	607
8	2D autocorrelations	213
9	Burden eigenvalues	96
10	P-VSA-like descriptors	55
11	ETA indices	23
12	Edge adjacency indices	324
13	Geometrical descriptors	38
14	3D matrix-based descriptors	99
15	3D autocorrelations	80
16	RDF descriptors	210
17	3D-MoRSE descriptors	224
18	WHIM descriptors	114
19	GETAWAY descriptors	273
20	Randic molecular profiles	41
21	Functional groups count	154
22	Atom-centred fragments	115
23	Atom-type E-state indices	172
24	CATS 2D	150
25	2D Atom Pairs	1596
26	3D Atom Pairs	36
27	Charge descriptors	15
28	Molecular properties	20
29	Drug-like indices	28
30	CATS 3D	300

Collecting reliable and standardized dataset is the first step to develop QSPR models, which is critical for developing robust models. Two databases are required to be established in this process, including the chemical or biological activity database and the descriptor database. The activity database, such as the second-order rate constant of radicals and chemicals, can be obtained either by experiment or collected from publications. The descriptor database indicates the numerical values that characterize the properties of chemicals. Dragon software has been used as an efficient tool to yield 5270 molecular descriptors, including constitutional, topological, geometrical descriptors, etc (**Table 2.4**). Gaussian software was used to yield the quantum-chemical descriptors, such as dipole moment, Ehomo, Elomo, etc.

Model optimization is to select an algorithm to describe the relations of descriptors and activities. Multiple linear regression (MLR), one of the most frequently used statistical techniques, models the linear relationship between activity data (k values) and multiple independent variables (descriptors) (Jin et al., 2015; Xiao et al., 2015b). The mathematical model for MLR model is described in a form of the linear equation:

$$y = tr(AX) + b \tag{2.19}$$

where y is the final fitting result obtained from the model; X is the high dimension classification matrix obtained from the experimental results; A is the coefficient matrix for regression or classification; b is the offset for model modification; and tr(·) indicates the trace of matrix AX.

Another approximation modeling method, artificial neural network (ANN), is inspired by the biological neural network of animal brains. An ANN model consists of an input layer, one or more hidden layer(s), and an output layer. Hidden neurons (weights) are used to connect the layers and project the input data to nonlinear spaces (**Figure 2.2**). By adjusting the weights, the difference between the predicted and observed data of the model can be decreased so that the model can be trained and optimized accordingly. Due to its ability to model nonlinear processes, ANN have found various applications in a wide range of disciplines since the 1990s. It has been indicated that ANN outperformed MLR in estimating k_{HO}. values for 457 water contaminants (Borhani et al., 2016). Recently, deep neural networks (DNNs), namely ANN with more than one hidden layer, have received an increasing attention in the field of artificial intelligence and machine learning. The predictivity of ANN models can be further improved by using multiple hidden layers (Ma et al., 2015; Song et al., 2017; Winkler and Le, 2017).

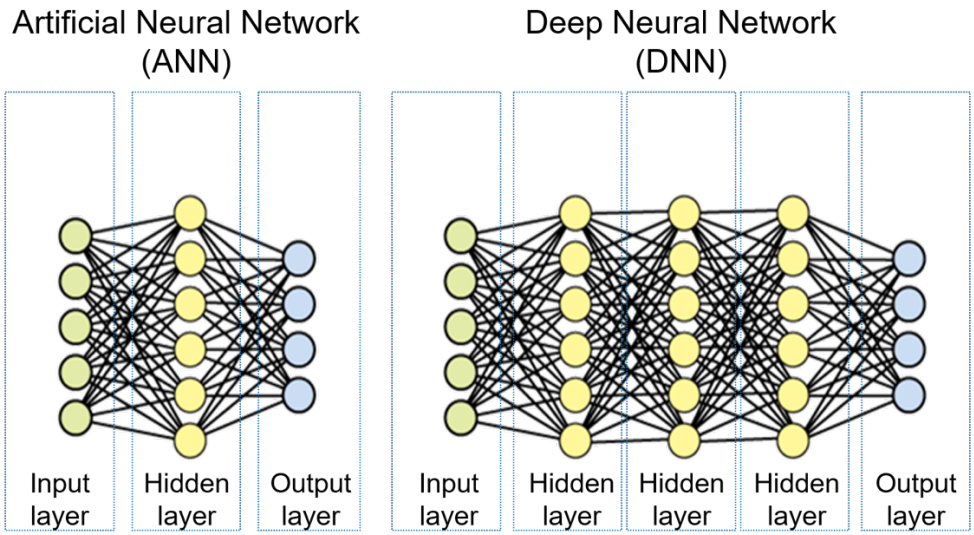

Figure 2.2 The diagram of ANN and DNN.

Model validation, the last step of QSPR modelling, is to verify the predictivity of the generated model. Statistical indicators, such as correlation coefficient, are calculated as the basic criteria for evaluating the performance of the model. In addition, the applicability domain, i.e., the paradigm set by representative compounds for model calibration, is calculated to ensure reliable predictions and avoid inaccurate predictions.

Chapter 3 Materials and methods

3.1 Chemicals and water samples

AZA, CP, CYT, 5FU, FLU, MIT, $NaHCO_3$, $NaNO_3$, Na_2SO_4, NaCl, Na_2HPO_4, NaH_2PO_4, AMX, *para*-chlorobenzoic acid (*p*CBA), *meta*-toluic acid (*m*TA), *tert*-butanol (*t*-BuOH) and humic acid (HA) were provided by Sigma-Aldrich (USA). MET, H_2O_2 (35% stock solution), and methanol were purchased from Merck (Germany). DOX was acquired from Fluka (Switzerland). Atrazine was obtained from AccuStandard (USA). All the chemicals and reagents were used as received without further purification. High purity deionized water was obtained from Milli-Q Water System. Three different types of water samples, including the deionized water, the treated water from a water treatment plant in Singapore, and the secondary effluent from a wastewater treatment plant in Singapore, were used in this research to assess the performance of the photolysis in practical applications. The characteristics of different water types are presented in **Table 3.1**.

Table 3.1 Characteristics of different types of water.

Water type	pH	Turbidity (NTU)	TOC ($mg \cdot L^{-1}$)	Total alkalinity ($mg \cdot L^{-1}$)	Nitrate ($mg \cdot L^{-1}$)	Sulfate ($mg \cdot L^{-1}$)	Chloride ($mg \cdot L^{-1}$)
Deionized water	6.0	<0.1	0.080	<5	<0.05	<0.045	<5
Treated water	8.0	0.22	0.79	13.0	3.20	21.6	10
Secondary effluent	6.7	5.3	10.6	54.9	6.28	45.1	146

3.2 Experimental procedures

Experiments were carried out using a 1-L cylindrical glass photoreactor. A low-pressure Hg lamp (5W, Philips, Netherlands) emitting UV irradiation at 254 nm and a quartz sleeve were placed coaxially in the photoreactor (**Figure 3.1**). An appropriate dose of H_2O_2 or PS was added to the water sample before UV irradiation. The solution pH was adjusted using 0.1 M H_2SO_4 or NaOH. Aliquots were collected at determined

time intervals and stored in amber vials pre-filled with 10 μL methanol to quench any residual oxidants. Independent triplicate runs were conducted in each experiment.

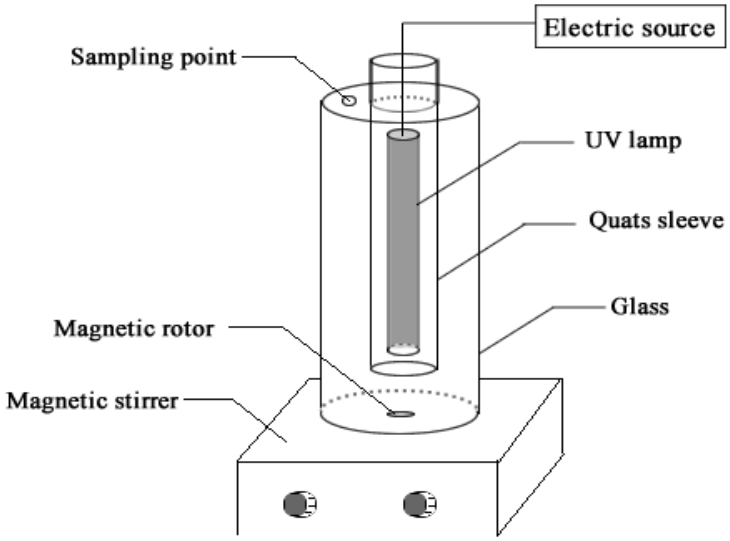

Figure 3.1 Schematic of the photoreactor used in the present study.

3.3 Analytical methods

The TOC of the water sample was determined by a Shimadzu TOC-VCSH analyzer with an ASI-V auto sampler. The concentrations of CSDs were analyzed using a triple quadrupole liquid chromatograph mass spectrometer (LC/MS/MS), which consists of a high-performance liquid chromatograph mass spectrometer module (LCMS-8030, Shimadzu, Japan) and a Shimadzu UFLC system. The whole LC/MS/MS system was controlled by LabSolutions Version 5.42 SP3 software (Shimadzu). A Luna 00C-4256-E0 C-18 LC column (Phenyl-Hexyl 100 Å, 75 mmx 4.6 mm, particle size 3 μm, Phenomenex, Torrance, CA, USA) was used for chromatographic separation of AZA. The sample injection volume was 10 μL and the total flow rate was 0.2 mL·min^{-1}. The mobile phase contained deionized water added with 0.1% formic acid (eluent A) and methanol added with 0.1% formic acid (eluent B). The gradient started with 10% of eluent B for 0.01 min, increased to 50% from 0.01-0.1 min, increased to 90% from 0.1-7 min, increased to 100% from 7-7.1 min, remained at 100% until 9 min, decreased to 10% from 9-9.1 min, then remained at starting condition (10% B) to re-equilibrate the column from 9.1-12 min. Selected

ion mode, LC retention time and optimized MS/MS detection conditions of the target CSDs used in LC/MS/MS are shown in **Table 3.2**. The AMX concentrations and intermediates were analyzed using Agilent 6460 Triple Quadrupole LC/MSMS System, equipped with a 75 mm×4.6 mm Phenomenex C18 column (3 μm particle size). A and B mobile phases were deionized water and acetonitrile both with 0.1% formic acid, respectively, at a flow rate of 0.4 mL min^{-1}. The sample injection volume was 5 μL and the column temperature was 40°C. A linear gradient progressed from 10% (initial conditions) to 90% A in 10 min, and was maintained at 90% A for 3 min. A post-run (2 minutes) was applied after each analysis to ensure the initial mobile-phase composition.

Table 3.2 Ion mode, LC retention time (t_R) and selected MS/MS detection conditions for determination of the target pharmaceuticals.

Compound	Ion mode	t_R (min)	Precursor m/z	Product m/z	Q1 Pre Bias (V)	CE (V)	Q3 Pre Bias (V)
AZA	+	4.188	278.00	142.00	-10.0	-10.0	-16.0
			278.00	232.05	-10.0	-15.0	-27.0
CP	+	5.604	261.10	140.00	-22.0	-20.0	-15.0
			261.10	63.05	-22.0	-40.0	-26.0
CYT	+	1.202	244.10	112.10	-20.0	-15.0	-12.0
			244.10	95.05	-20.0	-45.0	-19.0
DOX	+	4.514	544.20	397.20	-22.0	-15.0	-21.0
			544.20	130.20	-22.0	-15.0	-15.0
MET	+	3.843	455.30	308.15	-13.0	-20.0	-23.0
			455.30	134.05	-13.0	-40.0	-15.0
5FU	-	1.790	129.00	41.95	14.0	25.0	14.0
			129.00	86.10	14.0	25.0	25.0
FLU	-	8.086	275.00	202.05	12.0	25.0	20.0
			275.00	205.05	12.0	25.0	20.0
MIT	-	8.050	321.00	275.10	11.0	15.0	17.0
			321.00	202.05	11.0	30.0	20.0

3.4 Antibacterial activity tests

Agar diffusion tests were used to quantify the antibacterial activity of AMX solution using Oxford penicillin cup method according to the Clinical Laboratory

Standards Institute (CLSI) M100 (2017). Several 8 mm-diameter oxford penicillin cups were placed separately on the agar plate surface, which was cultivated with 10^8 CFU mL^{-1} *Escherichia coli* (ATCC 25922). After spiking with 100 μL of AMX samples into the cups, the plate was incubated at 37℃ for 16 h. The antimicrobial properties of the samples were analyzed by measuring the diameter of inhibition zone. All the media were sterilized by autoclaving at 121 ℃ for 20 min before use.

Growth inhibition tests were conducted to qualify the antibacterial activity of AMX solution using *Escherichia coli* (ATCC 25922) and *Staphylococcus aureus* (ATCC 6538) as Gram-negative bacteria and Gram-positive bacteria, respectively (Wammer et al., 2006). Bacteria with LB broth were first incubated in a shaker (150 rpm, 37 ℃) for 16 h to reach the exponential growth phase. Then 100 μL bacteria were added to test tubes containing 9 mL LB broth and 1 mL AMX sample. The tubes were incubated again for 16 h in the shaker (150 rpm, 37 ℃). Bacterial growth was measured by the absorbance of sample at the wavelength of 600 nm using a UV/VIS spectrophotometer. The absorbance value was converted to growth inhibition by Equation (3.1),

$$I = \frac{A_{\max} - A}{A_{\max} - A_{\min}} \tag{3.1}$$

where $A_{\max}$ is the absorbance of the positive control (i.e., no growth inhibition); $A_{\min}$ is the absorbance of the negative control (i.e., 100% growth inhibition); A is the absorbance of the test sample.

Dose-response relationships were achieved for serially-diluted AMX standards by plotting inhibition versus AMX concentration and fitting the data to Equation 3.2 using GraphPad Prism,

$$I = I_{\min} + \frac{I_{\max} - I_{\min}}{1 + 10^{(\log(EC_{50}/[AMX]))\cdot H}} = I_{\min} + \frac{I_{\max} - I_{\min}}{1 + (EC_{50}/[AMX])^{H}} \tag{3.2}$$

where EC_{50} is the effective AMX concentration yielding 50% growth inhibition of

bacteria, I_{min} and I_{max} are the minimum and maximum growth inhibition values of bacteria for a given data set, respectively; and H is the dimensionless Hill slope to the dose-response relationships.

3.5 Modeling calculations

The kinetic modeling results were analyzed using GraphPad Prism 5 software (GraphPad Software Inc., USA). Molecular orbital calculations were conducted with the optimal conformation, which has a minimum energy obtained at B3LYP/6-31G+ level in a Gaussian 09 system. Structures were optimized at Gaussian Viewer software using Hartree-Fock. The frontier electron densities of AMX were calculated to predict the reaction sites for $HO^{\bullet}$ and $SO_4^{\bullet-}$ attack, respectively.

Chapter 4 Direct and indirect UV photolysis of CSDs

4.1 Introduction

This chapter aims at investigating the photodegradation of CSDs by direct UV irradiation, UV/H_2O_2, and UV/PS processes. The degradation efficiencies of CSDs in each process were evaluated and compared first, followed by the effects of water matrix species, and the real water sample experiments. In addition, the transformation by-products of CSDs in each process were identified to elucidate the potential degradation pathways during processes. The total treatment cost was analyzed to provide an indicator of the cost-effectiveness of the three treatment processes.

4.2 Direct UV photolysis

4.2.1 Degradation of CSDs by direct UV photolysis

As shown in **Figure 4.1(a)**, the photolysis degradation rates of CSDs follow a pseudo-first-order kinetic model, which can be ascribed as follows:

$$\ln(C_0/C) = k_t t \quad (4.1)$$

where C_0 and C are the concentration of CSD before and after direct UV photolysis (μg L^{-1}), respective; k_t is the time-based first-order rate constant for direct UV photolysis (min^{-1}), and t is the degradation time (min).

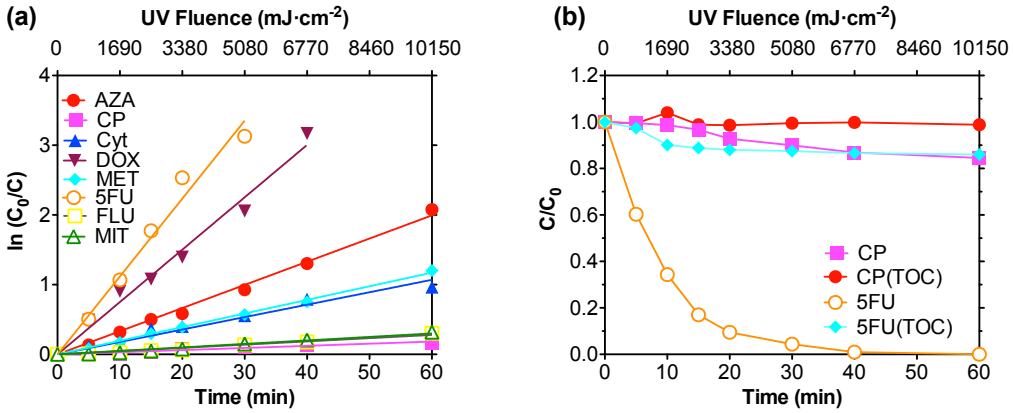

Figure 4.1 Photodegradation of CSDs using direct UV photolysis: (a) linear plots of 8 CSDs, and (b) degradation and mineralization degrees of CP and 5FU.

To allow cross comparison of the findings from this study with those using other chemical pollutants and photoreactors, the fluence-based first-order rate constant k_f (cm^2 mJ^{-1}) was calculated through Equation 4.2, where I_E is the average UV intensity (2.62 mW cm^{-2}). In addition, the degradation half-lives $t_{1/2}$ (min) and the removal rate R(%) of each CSD were also calculated.

$$k_f = k_t/I_E \tag{4.2}$$

$$t_{1/2} = 0.693/k_t. \tag{4.3}$$

$$R(\%) = [1\text{-}\exp(-k_t t)] \times 100 \tag{4.4}$$

As shown in **Table 4.1**, the difference in the degradation rate constants of the investigated CSDs in the single-species and multi-species systems is negligible, which indicates the insignificant competition of the species present in the multi-species medium for the irradiation light. Six of the investigated CSDs are degraded by less than 10% using UV fluence of 400 mJ cm^{-2} (10-fold of the typical water disinfection fluence), indicating the resistance of these CSDs towards direct UV photolysis. The degradation rates of CSDs follow the order: 5FU > DOX > AZA > MET > CYT > MIT ≈ FLU > CP. The degradation rate constant of 5FU (3.32×10^{-2} min^{-1}) is approximately 35 times larger than that of CP (0.31×10^{-2} min^{-1}). However, the complete photodegradation of 5FU is accompanied by a TOC loss of merely 14% after 60 min irradiation. As shown in **Figure 4.1(b)**, 5FU is slightly mineralized within the first 20 min, and then reaches a plateau period. It can be attributed to the two steps in the mineralization process, including the faster degradation of 5FU in the first phase and the slower formation of stable by-products in the second phase. The result also suggests that a large fraction of 5FU is transformed into its intermediate products without complete mineralization.

Table 4.1 shows that the molar absorption coefficients of the eight CSDs at UV 254 nm vary from 7 to 10037 M^{-1} cm^{-1}. The extremely low molar absorption coefficients of CP (7 M^{-1} cm^{-1}) and MIT (300 M^{-1} cm^{-1}) explain their negligible photodegradability at UV-254 nm among all the investigated CSDs. In addition, even though FLU shows relatively large absorbance at UV-254 nm, its extremely low quantum yield of 0.19×10^{-3} mol E^{-1} explains its negligible removal rate of 1.19% at UV fluence of 400 mJ cm^{-2}.

Table 4.1 Time-based first-order rate constant (k_t), half-life ($t_{1/2}$), fluence-based first-order rate constant (k_f), molar extinction coefficient (ε), quantum yield (Φ) of 8 CSDs by direct UV photolysis.

Compound	$k_t \times 10^2$ (min^{-1})		$t_{1/2}$ (min)	$k_f \times 10^4$ ($cm^2\ mJ^{-1}$)	ε ($M^{-1}\ cm^{-1}$)	$\Phi \times 10^3$	R(%) (400 mJ cm^{-2})	
	Single-species	Multi-species					UV	UV/H_2O_2
AZA	3.35	3.32(±0.27)	20.87(±1.70)	2.11(±0.17)	5369	0.80(±0.07)	8.10	60.51
CP	0.31	0.31(±0.03)	223.55(±21.63)	0.20(±0.02)	7	54.83(±5.31)	0.79	64.07
CYT	1.80	1.78(±0.20)	38.93(±4.37)	1.13(±0.13)	4337	0.53(±0.06)	4.43	86.02
DOX	7.58	7.51(±0.45)	9.23(±0.55)	4.78(±0.29)	10037	0.97(±0.06)	17.40	96.59
MET	1.97	1.95(±0.21)	35.54(±3.83)	1.24(±0.13)	1695	1.59(±0.16)	4.84	88.30
5FU	11.1	10.9(±0.37)	6.33(±0.21)	6.97(±0.24)	3506	4.06(±0.14)	24.32	90.36
FLU	0.48	0.47(±0.02)	147.45(±6.27)	0.30(±0.01)	3244	0.19(±0.008)	1.19	65.00
MIT	0.51	0.50(±0.03)	138.60(±8.32)	0.32(±0.02)	300	2.17(±0.13)	1.26	65.50

4.2.2 Effect of water matrix species

The anions that are ubiquitous in natural surface water and wastewater have been investigated, including humic acid (HA), nitrate (NO_3^-), bicarbonate (HCO_3^-), chloride (Cl^-) and sulfate (SO_4^{2-}). Experiments were then carried out with addition of these water matrix species at different concentrations to investigate the reactions between background constituents and UV irradiation and their influence on photodegradation of CSDs.

The experiments were conducted at HA concentrations from 1 to 10 mg L^{-1}. According to **Figure 4.2(a)**, the degradation efficiency of CSDs significantly decreases with addition of HA, indicating that HA is an inhibitor in the photodegradation process. In addition, the impact of scavenging effect strongly depends on the concentration of HA. Low concentration of HA (1 mg L^{-1}) shows insignificant influence on the CSDs photodegradation, while significant inhibition is observed when HA concentration is over 2 mg L^{-1}. The strong inhibition effect of HA may be ascribed to the light attenuation caused by the HA particles, and the undesirable degradation by-products generation during the reaction (Autin et al., 2013). Some studies also reported that HA can act as a promoter in pharmaceutical

degradation under UV photolysis (Lin et al., 2013; Verma and Sillanpää, 2015), which favors the indirect oxidation by generating reactive oxygen species (Chen et al., 2009; De la Cruz et al., 2012). However, the negative effect of HA overwhelms positive effect as observed in this study. The detailed mechanisms of HA-induced photolysis will be discussed in Section 4.3.4.

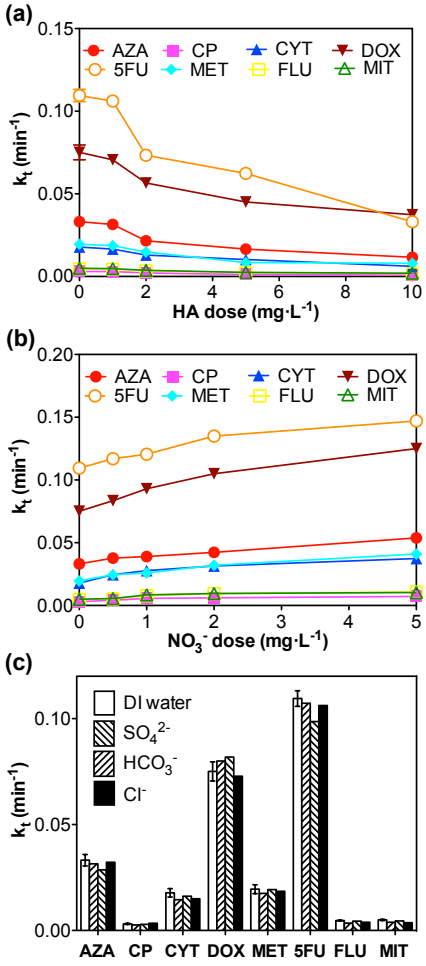

Figure 4.2 Effect of water matrix on CSDs degradation. (a) HA at 1-10 mg L^{-1}, (b) NO_3^- at 0.5-5 mg L^{-1}, (c) HCO_3^-, SO_4^{2-}, and Cl^- at 50 mg L^{-1}.

As a ubiquitous anion in surface water and wastewater, NO_3^- was investigated in the concentration range of 0.5-5 mg L^{-1}. As shown in **Figure 4.2(b)**, the presence of NO_3^- enhances the removal of CSDs. For example, the degradation rate of CP increases from 0.0031 to 0.0042 min^{-1} with addition of 0.5 mg L^{-1} NO_3^-. In addition, the degradation of CSDs is dependent on the concentration. Increasing NO_3^- dose from 0.5 to 5 mg L^{-1} gives rise to the rate constant enhancement of CP from 0.0042 to 0.0072 min^{-1}, which is approximately 2.32 times higher than that obtained in

deionized water. The reason is that NO_3^- can generate $HO^\bullet$ under direct UV photolysis, leading to an increase of the degradation efficiency of CSDs (Equations 4.5-4.9).

$$NO_3^- + h\nu \rightarrow NO_2^- + O \quad (4.5)$$

$$NO_3^- + h\nu \rightarrow O^{\bullet-} + NO_2^\bullet \quad (4.6)$$

$$2NO_2^\bullet + H_2O \rightarrow NO_2^- + NO_3^- + 2H^+ \quad (4.7)$$

$$O + H_2O \rightarrow 2HO^\bullet \quad (4.8)$$

$$O^{\bullet-} + H_2O \rightarrow HO^\bullet + HO^- \quad (4.9)$$

However, the contribution of indirect photolysis by NO_3^- towards some CSDs is insignificant. For example, the degradation rate of Flu increases from 0.109 to 0.147 min^{-1} with addition of 5 mg L^{-1} NO_3^-, which is merely 1.35 times higher than that obtained in deionized water. The reason may be due to that UV is mainly absorbed by NO_3^- at wavelength below 240 nm (**Figure 4.3(a)**). Therefore, the low absorption rate at UV 254 nm leads to a low quantum yield of $HO^\bullet$ production. The detailed mechanisms of NO_3^--induced photolysis will be discussed in Section 4.3.4. Other ions, including HCO_3^-, SO_4^{2-} and Cl^-, show negligible influence on the photodegradation effect of CSDs (**Figure 4.2(c)**). The filtering or screening effect by these ions was negligible, since none of these ions shows obvious UV-254 absorption (**Figure 4.3(b)**).

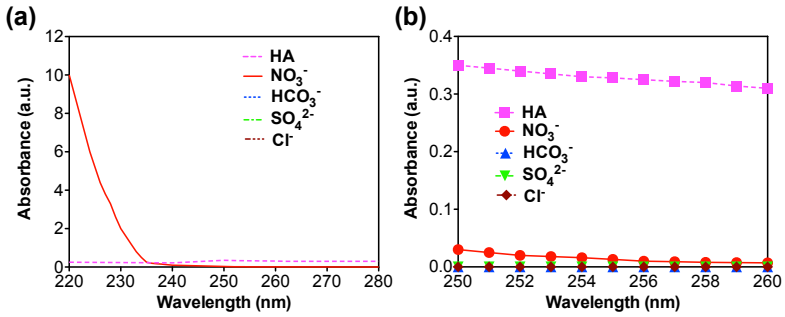

Figure 4.3 UV absorbance of HA (10 mg L^{-1}), NO_3^- (5 mg L^{-1}), HCO_3^- (50 mg L^{-1}), SO_4^{2-} (50 mg L^{-1}) and Cl^- (50 mg L^{-1}) in deionized water in the wavelength range of (a) 220-280 nm and (b) 250-260 nm.

4.2.3 Degradation of CSDs in natural water

Real water samples of treated water from a water treatment plant and secondary effluent from a wastewater treatment plant were used for the assessment of the UV treatment performances. According to **Figure 4.4,** the degradation rates of CSDs in treated water are comparable with those obtained in deionized water, since the low

TOC concentration of less than 1 mg L^{-1} in the treated water exerts negligible influence on CSDs degradation effect. In addition, it can be referred that the detrimental effect caused by HA of 0.79 mg L^{-1} equilibrates the beneficial effect caused by NO_3^- of 3.20 mg L^{-1}.

In comparison, the degradation rates of CSDs decrease dramatically in secondary effluent. The phenomenon is likely due to the high TOC concentration of 10.6 mg L^{-1} in the secondary effluent, which can compete for UV absorption and exert a significant detrimental effect on CSDs photolysis. In addition, UV shielding effect induced by the high turbidity of 5.3 NTU in secondary effluent may also inhibit the UV photolysis and give rise to a scavenging effect on CSDs degradation.

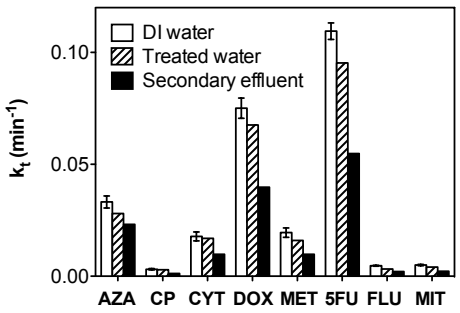

Figure 4.4 Effect of different types of water on CSDs degradation by direct UV photolysis. Error bars represent standard deviations obtained from triplicate datasets.

4.2.4 Proposed degradation pathways

The mass spectrums identified by LC/MS/MS (**Appendices 1-8**) give m/z information to the CSDs derivatives. As a result, the photodegradation pathways of each CSD by UV irradiation are hypothesized and shown in **Table 4.2**. It can be suggested that direct UV photolysis of the CSDs can take place through homolytic or heterolytic bond cleavage and radical generation. The carbon-centered radicals can be formed during the reaction as shown in Equation 4.10, followed by the photodegradation of the chemical.

$$R_3C\text{-}X + h\nu \rightarrow R_3C^{\bullet} + X^{\bullet} \quad (4.10)$$

Since DOM and NO_3^- are ubiquitously present in natural environment, the possible mechanisms were also investigated in indirect DOM-induced and NO_3^--induced photolysis, respectively. 5FU was chosen as the target compound due to its highest photolytic removal rate among the investigated CSDs. The untreated 5FU

solution shows a deprotonated molecule at m/z 129.0 with two ion fragments at m/z 86.1 and 42.0, which corresponds to the cleavage products of CONH group and C_3HNOF (**Appendix 6(a)**). In the direct UV photolysis, the additional peak detected at m/z 103.9 (**Appendix 6(b)**) indicates the nucleophilic ring opening reaction and the potential cleavage site of 5FU. It is suggested that the direct UV photolysis induces the cleavage of aromatic ring in the 5FU via an electronic excitation process. The bond homolysis results in a corresponding carbon-centered radical $5FU^*$. The electron, which transfers from the excited state of 5FU to ground state molecular O_2, leads to the photodegradation of 5FU.

With the addition of NO_3^- to the UV irradiation system, different radical species are generated from the irradiated NO_3^-, such as $HO^\bullet$ and $NO_2^\bullet$ (Equations 4.5-4.9), leading to the addition reaction with the unsaturated site of 5FU (Jo et al., 2011). The additional peaks with m/z 148 (**Appendix 6(c)**) indicate the hydroxylation step during the process, which can be possibly attributed to the saturation of the C5-C6 double bond of 5FU and hydrogenation of the C-6 carbon. In addition, 5FU can also be attacked by $NO_2^\bullet$ to produce the nitrated derivative compound.

With the addition of HA to the system, an electron transfer mechanism was proposed for the photodegradation of 5FU. Besides attenuating UV light intensity by absorbing UV photons, DOM can also give rise to the transformation of chemicals through indirect pathways. As shown in Equation 4.11, the photosensitizer molecule existed in DOM can be excited to its single state ($^1DOM^*$) and triplet state ($^3DOM^*$) by UV irradiation (Xiao et al., 2014). The $^3DOM^*$ are supposed to be the main reactive species in the reaction, and can be deactivated by O_2 to form singlet molecular oxygen ($^1O_2$) through Equation 4.12 (De la Cruz et al., 2012). As high energy form of O_2, $^1O_2$ can react rapidly with a number of organic pollutants. The LC/MS/MS spectrum (**Appendix 6(d)**) reveals that the first step of 5FU degradation is the charge-transfer interaction between excited HA and the N atom of 5FU. A hydrogen atom is then transferred to generate a carbon radical intermediate, and simultaneously leading to the addition of HO group. The degradation pathway of 5FU by UV photolysis was also observed by other researchers (Lutterbeck et al., 2016; Miolo et al., 2011).

$$DOM + h\nu \rightarrow {}^1DOM^* \rightarrow {}^3DOM^* \quad (4.11)$$

$$^{3}DOM^{*} + O_2 \rightarrow DOM + {}^{1}O_2 \quad (4.12)$$

Table 4.2 Proposed degradation pathways of CSDs under UV photolysis.

Compound	Proposed degradation pathway
AZA	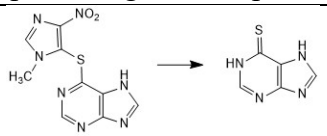
CP	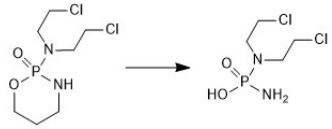
CYT	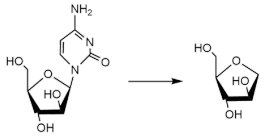
DOX	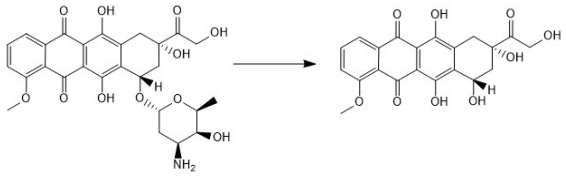
MET	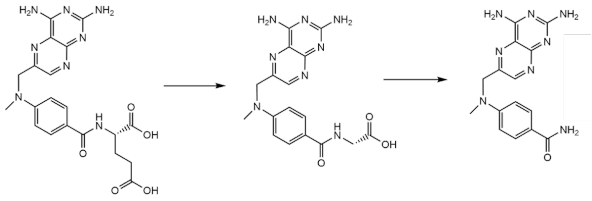
5FU*	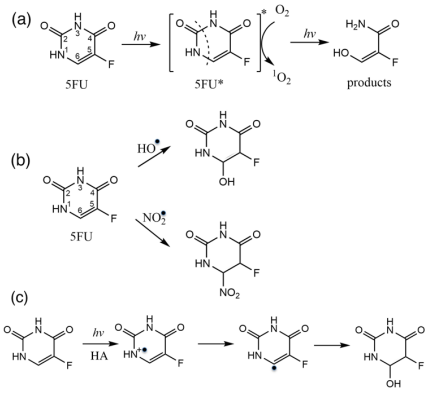
FLU	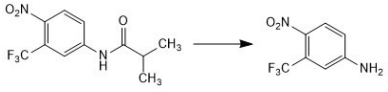
MIT	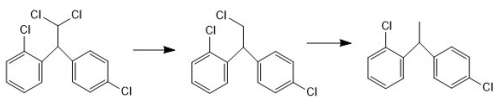

*(a) direct UV photolysis, (b) NO_3^--induced and (c) DOM-induced irradiation

4.2.5 Comparison of CSDs photodegradation by UV/H_2O_2 and UV/PS

Due to the UV resistance of some CSDs, UV/H_2O_2 and UV/PS processes have been investigated as potential alternative technologies. By generating highly reactive species $HO^{\bullet}$ and $SO_4^{\bullet-}$, these UV/AOPs can efficiently oxidize organic pollutants at diffusion-controlled reaction rate. The relatively high oxidant doses of 0.1 mM compared to that of CSDs maintain steady-state level concentrations of highly reactive radicals.

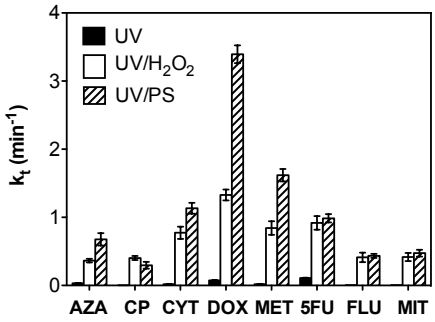

Figure 4.5 Comparison of CSDs degradation using UV, UV/H_2O_2 and UV/PS. [H_2O_2] = [PS] = 0.1 mM.

The combined photodegradation rates of CSDs via direct UV photolysis and radical-induced indirect photolysis in the two systems are represented as pseudo-first-order kinetics. As shown in **Figure 4.5**, compared with direct UV photolysis, the degradation effects of CSDs significantly increase in the two systems. However, the degradation rate constants obtained in each UV-AOPs vary from different CSDs. For most of the investigated CSDs, such as AZA, CYT, DOX and MET, the rate constants of these CSDs obtained in the UV/PS system are much higher than those in the UV/H_2O_2 system. However, the degradation rate constant of CP obtained in the UV/PS system is lower than that in the UV/H_2O_2 system. The reason can be explained as follows. As an electrophilic radical which reacts selectively via electron transfer, $SO_4^{\bullet-}$ selectively attacks certain electron-donating functional groups of CSDs, while $HO^{\bullet}$ attacks non-selectively through electron transfer, hydrogen abstraction or electrophilic addition reactions. As shown in **Table 4.2**, the CSDs which react rapidly with $SO_4^{\bullet-}$ possess a number of electron-donating groups, such as amino (-NH_2) in CYT, hydroxyl (-OH) in DOX, and unsaturated bonds in AZA and MET. As to CP, it contains none of the above-mentioned electron-donating groups. The $^{+}NR_3$ group in

CP has a strong electron-withdrawing inductive effect due to their positive charge. In addition, the function group -Cl in CP is also highly electronegative, which leads to a slow reaction with $SO_4^{\bullet-}$. For other CSDs, such as 5FU, FLU and MIT, they often contain a mixture of electron-donating groups and electron-withdrawing groups. As a result, their degradation rates in the UV/PS and UV/H_2O_2 systems are comparable.

4.3 UV/H_2O_2 process

4.3.1 Degradation of CP and 5FU by UV and UV/H_2O_2 processes

Based on the results, CP and 5FU show the lowest and highest degradation effect towards UV photolysis. As a result, they were chosen as representatives for the following UV/H_2O_2 process investigation. An initial concentration of 1 μM was selected for environmentally relevant reason according to **Table 2.2**. CP shows insignificant photodegradation effect by direct UV photolysis, for UV fluence of 400 mJ cm^{-2} (10-fold of the typical water disinfection fluence) can only result in a CP removal rate of 0.79%, which is further confirmed by its negligible UV-254 absorbance (**Figure 4.6(a)**). The reason is that amides bonds in CP cannot be cleaved efficiently through R-CO or CO-N bond breakage, since the resonance stability between N-C and C-O bonds are extremely high. CP has also been reported to show the lowest photodegradation effect among 30 pharmaceuticals and personal care products (Kim and Tanaka, 2009). In comparison, the degradation rate constant of 5FU (10.9×10^{-2} min^{-1}) is approximately 35 times larger than that of CP (0.31×10^{-2} min^{-1}), as confirmed by its relatively high absorbance at UV-254 nm.

The degradation of CSDs by 0.1 mM H_2O_2 is insignificant (**Figure 4.6(b)**). However, there is a remarkable degradation efficiency improvement of CSDs with addition of 0.1 mM H_2O_2 to UV irradiation system. The removal rate of CP at 400 mJ cm^{-2} increases from 0.79% to 64.07%, which implies the significant contribution of $HO^{\bullet}$ in CP degradation by UV/H_2O_2 process. The first-order rate constants of CP and 5FU in UV/H_2O_2 system are approximately 130 and 8.4 times higher than that in the UV system. Due to its extremely low photolysis effect, CP undergoes fast

photodegradation process in UV/H_2O_2 system due to HO•-assisted indirect photolysis. In comparison, the synergistic effect of both indirect photolysis and direct UV photolysis contributes to the 5FU photodegradation in the UV/H_2O_2 system. In addition, the difference of two CSDs degradation rate constants significantly decreases from 35 times to 2.3 times in UV and UV/H_2O_2 process, respectively. As a result, with the addition of H_2O_2, the required UV fluences to achieve a certain credit of CSDs degradation effect are considerably lower, leading to a significant savings for UV utilities energy costs.

TOC removal was also used as an indicator to evaluate the degree of CSDs mineralization. The TOC removal rates of CP and 5FU are only 15% and 26% after 3 min of UV/H_2O_2 treatment; while their corresponding removal rates reach 72% and 94%, respectively (**Figure 4.6(b)**). The fast photodegradation and slow mineralization of CSDs indicate that transformation products of CSDs are formed without complete mineralization. For example, approximately 21% of the 5FU is mineralized during the first 2 min, while afterwards the mineralization rate slows down relatively receiving 26% until 3 min. The complete degradation and remaining TOC suggest that CSDs are mineralized through two different phases. The parent CSDs will lead to the formation of newly recalcitrant transformation intermediates on the first phase, followed by the generation of final products on the second phase. The proposed mechanisms will be discussed in Section 4.4.7.

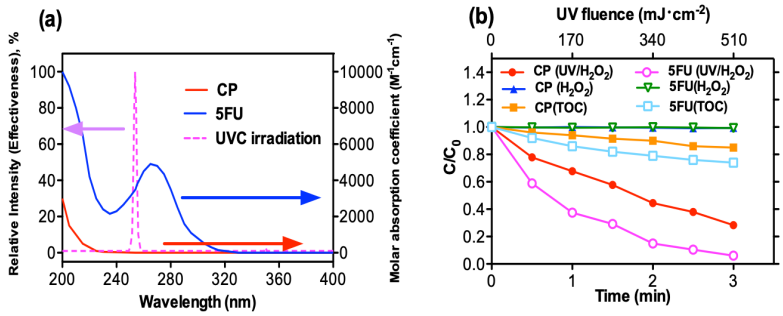

Figure 4.6 (a) UV absorbance of CP and 5FU and relative intensity of UVC irradiation. (b) Degradation and mineralization of CP and 5FU by UV/H_2O_2 process. Experimental conditions: $[CP]_0$ =$[5FU]_0$ =1 μM, $[H_2O_2]$ = 0.1 mM, pH = 7.

4.3.2 Effect of H_2O_2 dose

The effect of H_2O_2 dose were evaluated ranging from 0.01-5 mM. As shown in **Figure 4.7**, the degradation rate constants of CSDs increase proportionally with H_2O_2 dose in the range of 0.01-0.2 mM, which implies that the H_2O_2 dose is a rate-limiting factor at low dose. However, the CSDs degradation rate shows a plateau-type beyond this threshold. The self-scavenging effect of HO• caused by the excess H_2O_2 results in the slower increase of CSDs photodegradation. In addition, excess H_2O_2 over 0.5 mM decreases the CSDs degradation effect insignificantly, instead of increasing it appreciably.

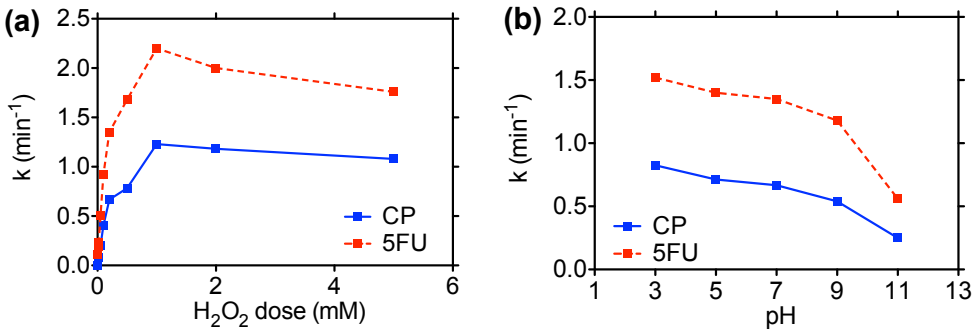

Figure 4.7 Effect of (a) H_2O_2 dose and (b) pH on CSDs degradation. Experimental conditions: $[CP]_0 = [5FU]_0 = 1\ \mu M$.

This phenomenon may be due to the self-scavenging effect of HO•. First, excess H_2O_2 reacts with HO• to produce less effective $HO_2^•$ ($E_{HO_2^•/HO_2^-}$ = 0.79V) at a high rate ($k_{HO^•,H_2O_2} = 2.7 \times 10^7\ M^{-1}\ s^{-1}$, Equation 4.13). In addition, the phenomenon may be also due to the self-decomposition (Equation 4.14) and higher self-recombination rate constant of HO• ($k_{HO^•,HO^•} = 5.5 \times 10^9\ M^{-1}\ s^{-1}$, Equation 4.15) (Buxton et al., 1988).

$$HO^• + H_2O_2 \rightarrow HO_2^• \ (k=2.7 \times 10^7\ M^{-1}s^{-1}) \quad (4.13)$$

$$HO^• \leftrightarrow H^+ + O^{•-} \ (pK_a=11.9) \quad (4.14)$$

$$HO^• + HO^• \rightarrow H_2O_2 \ (k=5.5 \times 10^9\ M^{-1}s^{-1}) \quad (4.15)$$

4.3.3 Economic comparison of UV and UV/H_2O_2 process

In order to determine the optimum H_2O_2 concentration, the total electrical energy per order, EE/O_{total} (\$ m^{-3} $order^{-1}$), was calculated as an equivalent energy-efficiency indicator. It is defined as the total electrical energy required to remove pollutant by one order of magnitude in 1 m^3 polluted water, which involves both electrical energy for UV lamp (EE/O_{UV}) and the equivalent electrical energy for H_2O_2 production (EE/O_{H2O2}), as shown in Equation 4.16. The equivalent electrical energy required for H_2O_2 production is 15 kWh kg^{-1} based on the electricity price of US\$0.1 kWh^{-1} (U.S. Energy Information Administration, 2015), as well as H_2O_2 price of US\$1.5 kg^{-1}:

$$EE/O_{total} = EE/O_{UV} + EE/O_{H2O2} \tag{4.16}$$

$$EE/O_{UV} = \frac{1.45Pt}{V\log\left(\frac{C_i}{C_f}\right)} = \frac{5.57\times10^{-2}P}{Vk}\left(\text{kWh}\cdot\text{m}^{-3}\cdot\text{order}^{-1}\right) \tag{4.17}$$

where P is the UV lamp output power (kW), t is the degradation time (h), V is the volume (m^3) of treated water, k is the first order rate constant (min^{-1}); C_i and C_f are the initial and final concentrations (mg L^{-1}) of CSDs, respectively.

According to **Figure 4.8**, EE/O_{H2O2} becomes dominant when the H_2O_2 dose increases over 0.4 mM, since $(EE/O_{H2O2})/(EE/O_{UV})>1$. The lowest EE/O_{total} is achieved at 0.2 mM for both CP and 5FU degradation. The addition of 0.2 mM H_2O_2 to UV system significantly decreases EE/O_{total} from 92.8 to 0.52 kWh m^{-3} $order^{-1}$for CP, and from 2.55 to 0.31 kWh m^{-3} $order^{-1}$ for 5FU, respectively. However, EE/O_{total} significantly increases with the H_2O_2 dose after the threshold. The opposite phenomenon may be ascribed to the self-scavenging effect and the high cost of H_2O_2. As a result, an optimum H_2O_2 dose of 0.2 mM was selected in the subsequent experiments.

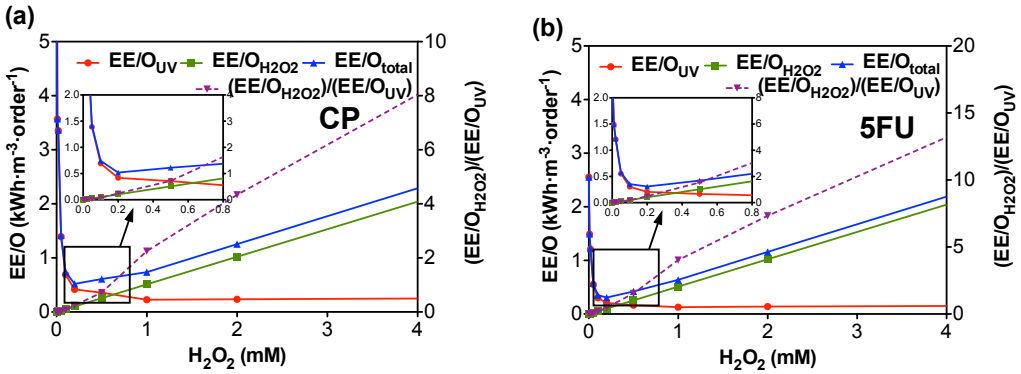

Figure 4.8 EE/O_{total} comparison for (a) CP and (b) 5FU degradation as a function of the H_2O_2 dose. Experimental conditions: $[CP]_0$ =$[5FU]_0$ =1 μM, pH=7.

4.3.4 Effect of pH

Figure 4.7(b) shows the effect of pH in the range of 3 to 11 in the UV/H_2O_2 systems on the CSDs degradation. The degradation efficiencies of CSDs decrease slightly with increasing pH in acidic, neutral and slightly basic solutions, while the decreasing trend becomes significant in basic solution. Four reasons can be attributed to the lower CSDs degradation efficiency at higher pH (Deng et al. 2013, Tan et al. 2012b, Tan et al. 2013). First, the redox potential $E_{HO^{\bullet},H_2O}$ reduces from 2.62 to 2.15 V with pH increasing from 3 to 11 according to Nernst equation (Equation 4.18).

$$E_{HO^{\bullet},H_2O} = E^0_{HO^{\bullet},H_2O} - 0.0059\text{pH} \quad (4.18)$$

Second, less reactive species $O^{\bullet-}$ ($E_{O^{\bullet},H_2O/2HO^{\bullet}}$ =1.78 V) are generated due to $HO^{\bullet}$ dissociation under strong alkaline condition.

$$HO^{\bullet} \leftrightarrow H^+ + O^{\bullet-} \text{ (pKa=11.9)} \quad (4.19)$$

Third, high concentration of OH^- can also scavenge $HO^{\bullet}$ at a high reaction rate (Buxton et al., 1988).

$$HO^{\bullet} + OH^- \rightarrow H_2O + O^{\bullet} \text{ (k=1.2 × 10}^{10}\text{ M}^{-1}\text{s}^{-1}\text{)} \quad (4.20)$$

In addition, HO_2^- becomes the main component form in H_2O_2 with further increasing pH (Equation 4.21). It also acts as $HO^{\bullet}$ scavenger by reacting with $HO^{\bullet}$ at a faster reaction rate ($k_{HO^{\bullet},HO_2^-}$ = 7.5 × 10^9 $M^{-1}s^{-1}$, Equation 4.22) compared with H_2O_2

($k_{H_2O_2,HO_2^-}$ = 2.7 × 10^7 $M^{-1}s^{-1}$, Equation 4.23).

$$H_2O_2 \leftrightarrow HO_2^- + H^+ (pK_a=11.6) \quad (4.21)$$

$$HO^\bullet + HO_2^- \rightarrow HO^- + HO_2^\bullet (k=7.5 \times 10^9\ M^{-1}s^{-1}) \quad (4.22)$$

$$HO^\bullet + H_2O_2 \rightarrow HO_2^\bullet (k=2.7 \times 10^7\ M^{-1}s^{-1}) \quad (4.23)$$

The insignificant variation of CSDs degradation efficiencies in acidic, neutral and slightly basic solutions indicates the application advantage of UV/H_2O_2 compared with other pH-dependent water treatment technologies, such as chlorination, bromination and ozonation. The degradation effect of 5FU reached the maximum at pH 7 using either chlorination or bromination (Li et al., 2015). It has been reported that the ozone depletion rates increased with pH in the range of 6-9 during ozonation process in decarbonated surface water, due to the hydroxide-initiated O_3 decomposition reaction (Elovitz et al., 2000).

4.3.5 Effect of water matrix species

The effect of various naturally ubiquitous water matrix species, including NOM, Cl-, HCO_3^-, NO_3^- and SO_4^{2-}, was investigated using deionized water spiked with various concentrations of matrix species. Based on the natural water characteristics (**Table 3.1**), the concentration range of NOM and various inorganic anions were determined as 0-20 mgL^{-1} and 0-4 mM, respectively. As shown in **Figures 4.9(a) and (b)**, the photodegradation effect of CSDs are considerably inhibited by NOM, HCO_3^- and Cl^-. In addition, NO_3^- shows positive effect, while SO_4^{2-} exhibits negligible influence on CSDs degradation.

NOM, HCO_3^- and Cl^- all show negative effect on CSDs degradation due to their scavenging effect of $HO^\bullet$. HCO_3^- can react with $HO^\bullet$ to form less reactive species with lower redox potential ($E_{CO_3^{\bullet-},CO_3^{2-}}$ = 1.5 V). The lower reaction rate constant ($k_{HO^\bullet,HCO_3^-}$ = 8.5 × 10^6 $M^{-1}s^{-1}$, Equation 4.24) compared with that of NOM ($k_{HO^\bullet,NOM}$

= 2.23 × 10^8 $M^{-1}s^{-1}$, Equation 4.25) leads to a less obvious prohibitive degradation effect of CSDs caused by HCO_3^-. Besides $HO^\bullet$ scavenging effect, NOM can also absorb UV light and reduce UV transmittance meanwhile.

$$HCO_3^- + HO^\bullet \rightarrow CO_3^{\bullet-} + H_2O \ (k=8.5 \times 10^6\ M^{-1}s^{-1}) \quad (4.24)$$

$$NOM + HO^\bullet \rightarrow Products \ (k=2.23 \times 10^8\ M^{-1}s^{-1}) \quad (4.25)$$

Although Cl^- scavenges $HO^\bullet$ at a fast reaction rate ($k_{HO^\bullet,Cl^-}$ = 4.3 × 10^9 $M^{-1}s^{-1}$, Equations 4.26-4.29 (Buxton 88)), additional reactions of $Cl^\bullet$ with H_2O (Equation 4.30) can also produce $HO^\bullet$, giving rise to an increasing photodegradation effect of CSDs (Zhou 12). In addition, the redox potential $E_{Cl^\bullet/Cl^-}$ =2.41 V is also comparable to $E_{HO^\bullet,H_2O}$ = 2.39 V. As a result, Cl^- shows less influence on CSDs degradation compared with NOM or HCO_3^-.

$$Cl^- + HO^\bullet \rightarrow ClOH^{\bullet-} \ (k=4.3 \times 10^9\ M^{-1}s^{-1}) \quad (4.26)$$

$$ClOH^{\bullet-} + H^+ \rightarrow Cl^\bullet + H_2O \ (k=3.0 \times 10^{10}\ M^{-1}s^{-1}) \quad (4.27)$$

$$ClOH^{\bullet-} + Cl^- \rightarrow Cl_2^{\bullet-} + OH^- \quad (k=1.0 \times 10^5\ M^{-1}s^{-1}) \quad (4.28)$$

$$Cl^- + SO_4^{\bullet-} \rightarrow Cl^\bullet + SO_4^{2-} (k=3.1 \times 10^8\ M^{-1}s^{-1}) \quad (4.29)$$

$$Cl^\bullet + H_2O \rightarrow H^+ + HO^\bullet + Cl^- \ (k=2.5 \times 10^5\ M^{-1}s^{-1}) \quad (4.30)$$

In contrast, the addition of NO_3^- slightly increases the degradation effect of CSDs, since NO_3^- can generate additional $HO^\bullet$ under direct UV photolysis (Equations 4.31-4.35).

$$NO_3^- + h\nu \rightarrow NO_2^- + O \quad (4.31)$$

$$NO_3^- + h\nu \rightarrow O^{\bullet-} + NO_2^\bullet \quad (4.32)$$

$$2NO_2^\bullet + H_2O \rightarrow NO_2^- + NO_3^- + 2H^+ \quad (4.33)$$

$$O + H_2O \rightarrow 2HO^\bullet \quad (4.34)$$

$$O^{\bullet-} + H_2O \rightarrow HO^\bullet + HO^- \quad (4.35)$$

Insignificant effect of SO_4^{2-} on CSDs degradation is observed due to its slow

reaction rates with HO• ($k_{HO^{\bullet},SO_4^{2-}}$ =3.5 ×10^5 M^{-1}s^{-1}, Equation 4.36) and relatively high redox potential of the generated radical ($E_{SO_4^{\bullet-},SO_4^{\bullet-}}$ =2.5-3.1 V) (Løgager et al., 1993).

$$SO_4^{2-} + HO^{\bullet} \rightarrow SO_4^{\bullet-} + OH^- \ (k=3.5 \times 10^5\ M^{-1}s^{-1}) \qquad (4.36)$$

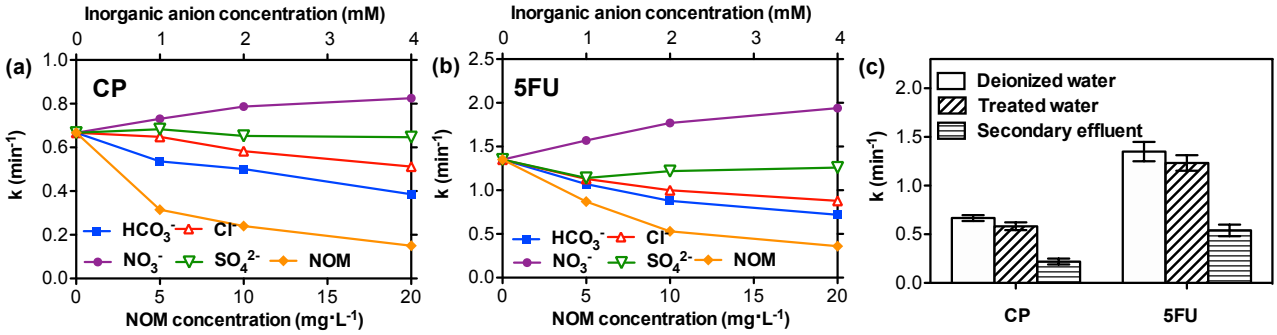

Figure 4.9 Effect of water matrix species on (a) CP and (b) 5FU degradation, and (c) Effect of different water types on CSDs degradation. Experimental conditions: $[CP]_0$ =$[5FU]_0$ =1 μM, $[H_2O_2]$ = 0.2 mM, pH=7.

4.3.6 Degradation of CP and 5FU in natural water

In order to evaluate the UV/H_2O_2 performance in real application, treated water from a water treatment plant and secondary effluent from a wastewater treatment plant were used as natural water samples. The water quality characters of natural water samples are shown in **Table 3.1**. **Figure 4.9(c)** shows that the degradation effect difference of CSDs in treated water and in deionized water is negligible. However, the degradation effect of CSDs decreases considerably in secondary effluent, due to the side-reaction competition between HO• and the background species. High turbidity and high concentration of TOC, HCO_3^- and Cl^- may act as HO• scavengers and inhibit the photodegradation effect.

4.3.7 Proposed photodegradation pathways

The photodegradation pathways of CP and 5FU are proposed in **Figure 4.10**, according to their photodegradation transformation products (TPs) identified from the LC/MS/MS spectra (Appendices 9-10). The untreated CP shows a protonated

molecule at $[M+H]^+$=261.1, while 5FU shows a deprotonated molecule at $[M-H]^-$ =129.0.

In the direct UV photolysis system, CSDs can be photodegraded by bond cleavage. TP-220 ($[M+H]^+$=221), which is 40 Da less than CP, is probably generated by the loss of propyl group chain in CP, while TP-105 ($[M-H]^-$=104) implies the nucleophilic ring opening reaction for 5FU. Direct UV photolysis can cleave the aromatic ring in both CSDs by electronic excitation process, resulting in the generation of corresponding carbon-centered radical followed by the CSDs photodegradation.

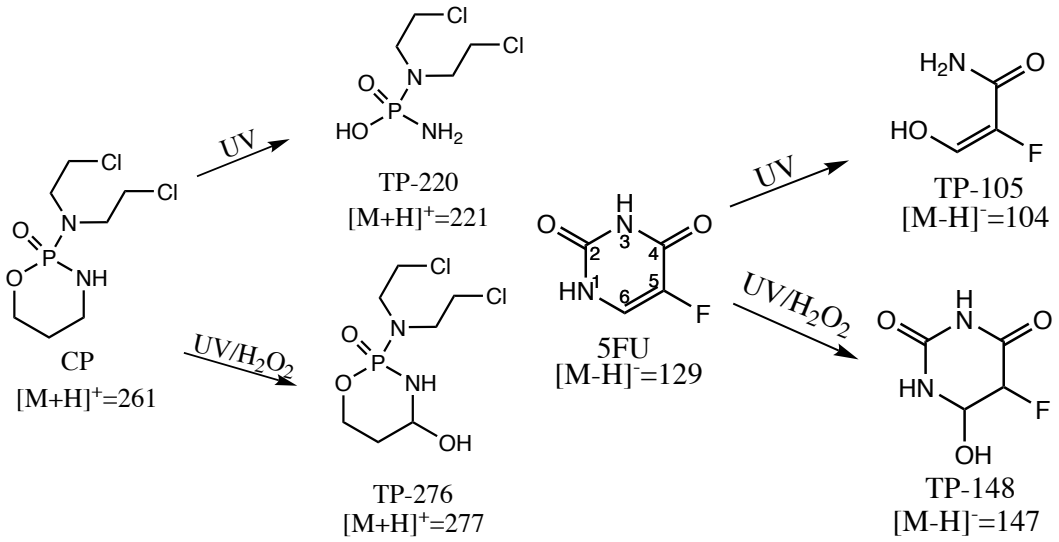

Figure 4.10 Proposed degradation pathways of CP and 5FU by UV and UV/H_2O_2.

In the UV/H_2O_2 system, CSDs photodegradation can be caused by the HO• addition reaction to the unsaturated site. A single hydroxylation pathway on the C-pyrimidine of 5-FU was proposed based on the additional peak of TP-148 ($[M-H]^-$ =147). Compared to parent compound 5-FU, TP-148 shows a cleavage of CONH by uracil hydrogenation, followed by a further hydroxylation on the unoccupied C-6 carbon because of the saturation on the C5–C6 double bond. In addition, TP-276 ($[M+H]^+$=277) is one oxygen atom higher compared with the parent compound CP, indicating the corresponding transformation product formation through a

hydroxylation. The addition of hydroxyl group to CP may occur on either carbon atom of the molecule.

4.4 UV/PS process

4.4.1 Degradation of AZA by UV, UV/H_2O_2, and UV/PS processes

Due to its high photoresistance and toxicity, AZA was chosen as a model representative CSD for the mechanistic and economic comparison of UV/H_2O_2 and UV/PS processes. **Figure 4.11(a**) shows an overlap of AZA absorption and UV lamp emission spectrum over a wavelength range of 200-400 nm. When subjected to UV irradiation, the photoactive aromatic ring in AZA absorbs the UV photon, giving rise to the formation of electronically excited state molecule AZA$^{\bullet}$. The chemical decomposition of AZA$^{\bullet}$ to produce by-products leads to the direct photodegradation of AZA (Khan et al., 2014).

However, the direct photolysis degradation of AZA is insignificant. As shown in **Figure 4.11(b)**, UV fluence of 510 mJ cm^{-2} can only result in an AZA removal of 10%. The reason is probably due to the low quantum yield Φ_{254} of AZA, which is 0.008 mol E^{-1} based on the observed first-order rate constant of 0.033 min^{-1} and the molar absorption coefficient of 5359 M^{-1} cm^{-1} (Equation 4.37).

$$\Phi_{AZA} = \Phi_{atrazine} \frac{k_{AZA}\varepsilon_{atrazine}}{k_{atrazine}\varepsilon_{AZA}} \tag{4.37}$$

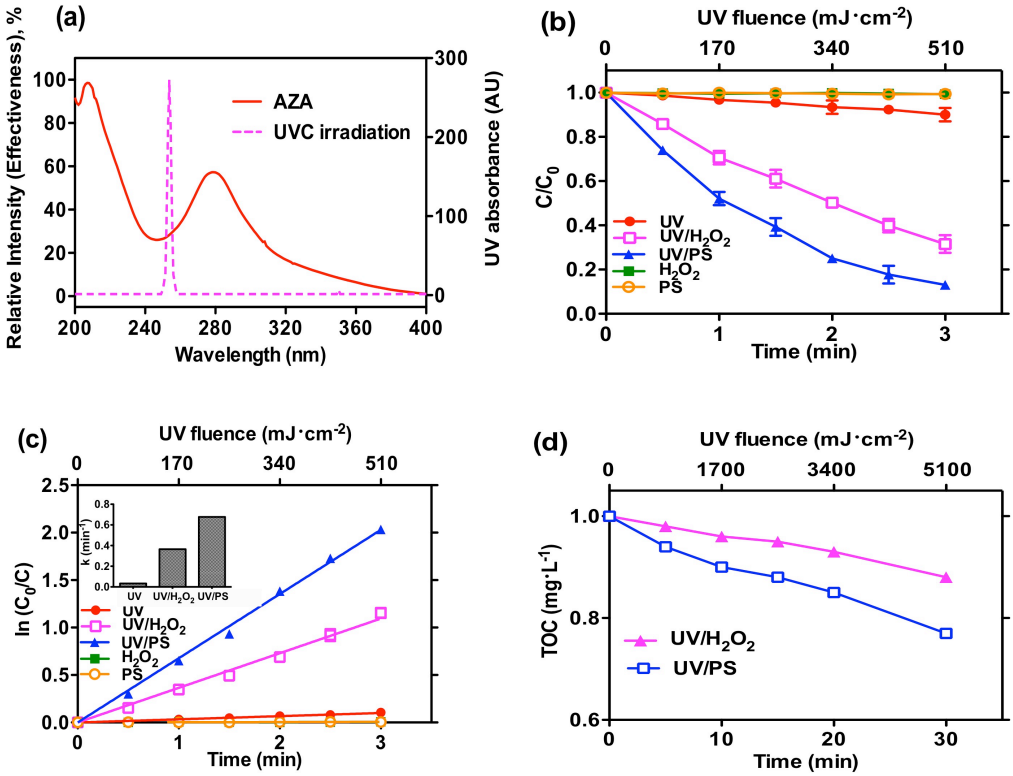

Figure 4.11 (a) UV absorbance of AZA and relative irradiation intensity of UVC irradiation. (b) Degradation of AZA in the H_2O_2, PS, UV, UV/H_2O_2 and UV/PS systems. (c) Linear plots of AZA degradation in the different systems. (d) Mineralization of AZA in terms of TOC removal in the UV-AOP systems. Inset shows the degradation rate constants of AZA. Experimental conditions: $[AZA]_0$ = 3.3 μM, $[H_2O_2]$ = [PS] = 100 μM, pH = 7.

In the control experiment, oxidation of AZA by 100 μM H_2O_2 or PS alone in the dark is negligible (**Figure 4.11(c)**). However, the addition of 100 μM H_2O_2 or PS with UV irradiation significantly increases the degradation efficiency of AZA from 0.033 to 0.365 and 0.677 min^{-1}, respectively. The removal rate of AZA at UV dose of 510 mJ cm^{-2} are 68% and 87% by UV/H_2O_2 and UV/PS, respectively, compared with 10% by direct UV photolysis, indicating the considerable contribution of $HO^{\bullet}$ and $SO_4^{\bullet-}$ radicals in UV-AOPs.

TOC removal, which indicates the degree of AZA mineralization, was evaluated independently in this study. As shown in Figure 4.11d, only 12% and 23% TOC are removed after 30 min irradiation in the UV/H_2O_2 and UV/PS system, respectively,

while AZA is completely removed. UV/PS process is more effective than UV/H_2O_2 process in mineralizing AZA, which is in good agreement with the higher degradation efficiency of AZA observed previously. The result also suggests that a large fraction of AZA is transformed into its intermediate products without complete mineralization.

To compare the reactivity of radicals in AZA degradation, the second-order rate constants of AZA with HO$^{\bullet}$ ($k_{HO^{\bullet},AZA}$) and $SO_4^{\bullet-}$ ($k_{SO_4^{\bullet-},AZA}$) were estimated according to the competition kinetics. The reference compounds, *p*CBA and *m*TA, with their known second-order rate constants with radicals, $k_{HO^{\bullet},pCBA}$ = 5 × 10^9 M^{-1} s^{-1} (Buxton et al., 1988) and $k_{SO_4^{\bullet-},mTA}$ = 2 × 10^9 M^{-1} s^{-1} (Neta et al., 1977), were used in the competition studies. In the UV/PS system, due to the formation of HO$^{\bullet}$ from $SO_4^{\bullet-}$ according to Equations. 4.38-4.39, *t*-BuOH was used as the HO$^{\bullet}$ quenching reagent, for its reactivity with HO$^{\bullet}$ ($k_{HO^{\bullet},t-BuOH}$ = 6 ×10^8 M^{-1} s^{-1}) (Buxton et al., 1988), which is 3-order of magnitude higher than that with $SO_4^{\bullet-}$ ($k_{SO_4^{\bullet-},t-BuOH}$ = 8.4 × 10^5 M^{-1} s^{-1}) (Clifton and Huie, 1989).

$$SO_4^{\bullet-} + H_2O \rightarrow HO^{\bullet} + SO_4^{2-} + H^+ \text{ (pH=7)} \quad (4.38)$$

$$SO_4^{\bullet-} + OH^- \rightarrow HO^{\bullet} + SO_4^{2-} \text{ (pH=11)} \quad (4.39)$$

The apparent first-order rate constant, k_t (s^{-1}), in the UV-AOPs involves direct photolysis rate constant k_d (s^{-1}) and indirect radical-assisted reaction rate constant k_i (s^{-1}) (Equation 4.50), while k_i can be further expressed as a function of the second-order rate constant of radicals with compound k_{rad} (M^{-1} s^{-1}) and the steady-state radical concentration C_{rad} (M) (Equations 4.51-4.52).

$$-\frac{dC}{dt} = k_t C = (k_d + k_i)C \quad (4.50)$$

$$k_{i,AZA} = k_{rad,AZA}C_{rad} = k_{t,AZA} - k_{d,AZA} \quad (4.51)$$

$$k_{i,ref} = k_{rad,ref}C_{rad} = k_{t,ref} - k_{d,ref} \quad (4.52)$$

where $k_{t,AZA}$ and $k_{t,ref}$ are the first-order observed photolysis rate constants (s^{-1}) of AZA and reference compound, respectively; $k_{i,AZA}$ and $k_{i,ref}$ are the first-order indirect photolysis rate constants (s^{-1}) of AZA and reference compound, respectively; $k_{d,AZA}$ and $k_{d,ref}$ are the first-order direct photolysis rate constants (s^{-1}) of AZA and reference compound, respectively.

By integrating Equations 4.51-4.52, k_{rad} can be expressed as:

$$k_{HO^{\bullet},AZA} = \frac{k_{t,AZA} - k_{d,AZA}}{k_{t,pCBA} - k_{d,pCBA}} k_{HO^{\bullet},pCBA} \quad (4.53)$$

$$k_{SO_4^{\bullet-},AZA} = \frac{k_{t,AZA} - k_{d,AZA}}{k_{t,mTA} - k_{d,mTA}} k_{SO_4^{\bullet-},mTA} \quad (4.54)$$

where $k_{HO^{\bullet},AZA}$ and $k_{SO_4^{\bullet-},AZA}$ are the second-order rate constants (M^{-1} s^{-1}) of $HO^{\bullet}$ and $SO_4^{\bullet-}$ with AZA, respectively; $k_{HO^{\bullet},pCBA}$ is the second-order rate constants (M^{-1} s^{-1}) of $HO^{\bullet}$ with *p*CBA and $k_{SO_4^{\bullet-},mTA}$ is the second-order rate constants (M^{-1} s^{-1}) of $SO_4^{\bullet-}$ with *m*TA.

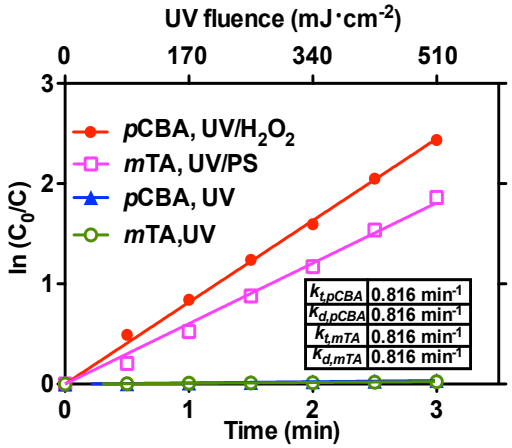

Figure 4.12 Degradation of *p*CBA and mTA in the UV, UV/H_2O_2 and UV/PS systems. Experimental conditions: $[pCBA]_0 = [mTA]_0 = 3.3$ μM, $[H_2O_2] = [PS] = 100$ μM, pH = 7.

The linear plots for the reference compound degradation in the UV/H_2O_2 and UV/PS systems are shown in **Figure 4.12**. The determined second-order rate constants of AZA with $HO^{\bullet}$ and $SO_4^{\bullet-}$ ($k_{HO^{\bullet},AZA}$ and $k_{SO_4^{\bullet-},AZA}$) are 1.86×10^9 M^{-1} s^{-1}

and 2.16×10^9 M^{-1} s^{-1}, respectively. Since the derived second-order rate constants in the two UV-AOP systems are comparable, other factors can contribute to the significant difference of AZA degradation rate observed in **Figure 4.11**. The radical quantum yield of PS (Φ_{254} = 1.4-1.8 mol E^{-1}, ε_{254} = 20.0 M^{-1} cm^{-1}) (Mark 90) is much larger than that of H_2O_2 (Φ_{254} = 1.0 mol E^{-1}, ε_{254} = 19.6 M^{-1} cm^{-1}) (Baxendale 57), giving rise to a higher radical production yield. In addition, due to the short $HO^{\bullet}$ lifetime of 100 ns, reactions can only occur in close proximity to the $HO^{\bullet}$ generation site in the UV/H_2O_2 system (Kasiri and Khataee, 2012; Zoschke et al., 2012). In contrast, $SO_4^{\bullet-}$ has a much longer lifetime of up to 30-40 μs, allowing its reaction with pollutants in well-mixed solution at near diffusion-controlled rates (Antoniou et al., 2010).

4.4.2 Effect of oxidant dose

The effects of oxidant dose on the AZA degradation in the range of 10 to 100 μM ($[Oxidant]_0$ / $[AZA]_0$ = 3 to 30) in the UV/H_2O_2 and UV/PS systems are shown in **Figures 4.13(a)** and **(b)**, respectively. The insets of **Figures 4.13(a)** and **(b)** show that the first-order degradation rate constants of AZA increase linearly with the increasing oxidant dose. In the UV/H_2O_2 system, $k_t = 0.0032[H_2O_2] + 0.033$, while in the UV/PS system, $k_t = 0.0062[PS] + 0.033$. The rate constant of AZA increases from 0.043 to 0.365 min^{-1} in the UV/H_2O_2 system, and from 0.068 to 0.677 min^{-1} in the UV/PS system, with oxidant dose increasing from 10 to 100 μM. This phenomenon indicates that the oxidant dose is a rate-limiting factor in the UV-AOP processes at a low dose.

Excessive oxidant, however, can result in an unproductive consumption of oxidant. **Figure 4.13(c)** compares the degradation efficiency of AZA with high oxidant dose ranging from 100 to 2000 μM ($[Oxidant]_0$ / $[AZA]_0$ = 30 to 600). In the UV/PS process, the degradation rate of AZA remains increasing non-linearly with the PS dose, which indicates no significant inhibiting effect of PS. However, in the

UV/H_2O_2 process, a plateau-type of AZA degradation rate is observed when the H_2O_2 concentration is over 500 μM. The much slower AZA degradation improvement with the increasing H_2O_2 dose indicates a self-scavenging effect of $HO^{\bullet}$ by the excess H_2O_2.

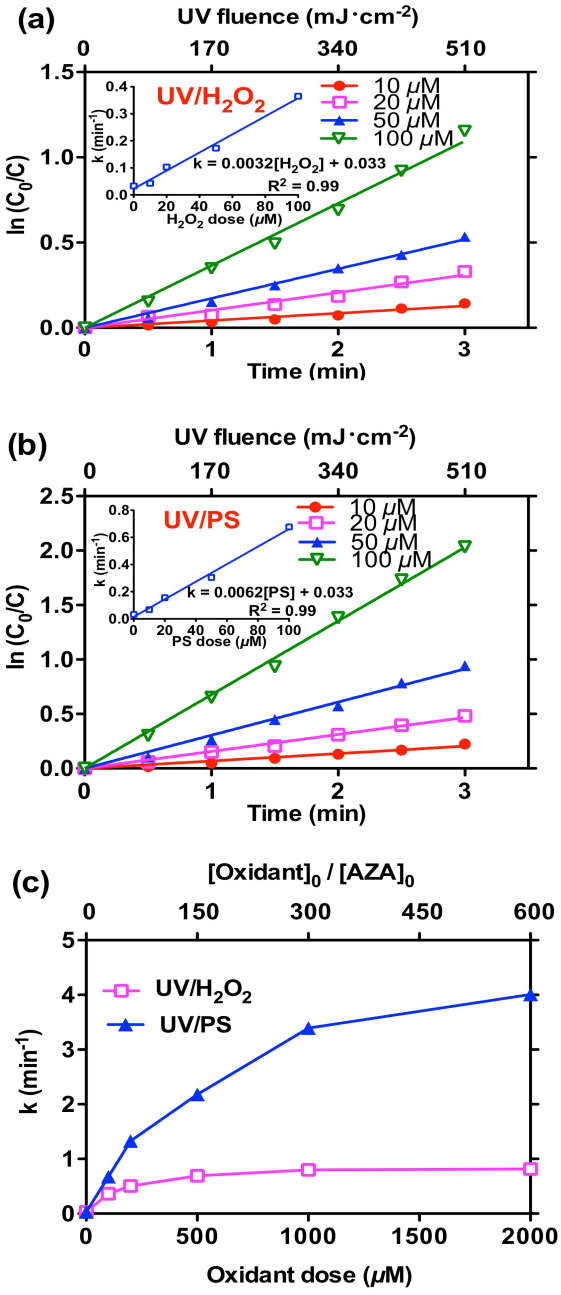

Figure 4.13 Effect of oxidant dose on AZA degradation rate: (a) [H_2O_2] = 10-100 μM, (b) [PS] = 10-100 μM, **(c)** [H_2O_2] = [PS] = 100-2000 μM. Inset shows the effect of degradation rate constants as a function of oxidant dose. Experimental conditions: $[AZA]_0$ = 3.3 μM, pH=7.

This phenomenon can be explained as follows. First, excess H_2O_2 can act as $HO^{\bullet}$ scavenger and generate $HO_2^{\bullet}$ with lower redox potential ($E_{HO_2^{\bullet}/HO_2^-}$ =0.79V) (Oppenländer, 2003). The self-scavenging of $HO^{\bullet}$ by H_2O_2 is much more obvious than that of $SO_4^{\bullet-}$ by $S_2O_8^{2-}$ (Kwon et al., 2015), for the rate constant of $HO^{\bullet}$ with H_2O_2 ($k_{HO^{\bullet},H_2O_2}$ = 2.7 × 10^7 $M^{-1}s^{-1}$, Equation 4.55) (Buxton et al., 1988) is almost 40 times higher than that of $SO_4^{\bullet-}$ with $S_2O_8^{2-}$ ($k_{SO_4^{\bullet-},S_2O_8^{2-}}$ = 6.6 × 10^5 $M^{-1}s^{-1}$, Equation 4.56) (Neta et al., 1988). Besides, the higher self-recombination rate constant of $HO^{\bullet}$ ($k_{HO^{\bullet},HO^{\bullet}}$ =5.5 × 10^9 $M^{-1}s^{-1}$, Equation 4.57) (Buxton et al., 1988)) compared with that of $SO_4^{\bullet-}$ ($k_{SO_4^{\bullet-},SO_4^{\bullet-}}$ =3.1 × 10^8 $M^{-1}s^{-1}$, Equation 4.58) (Neta et al., 1988) can also account for the inhibition phenomenon.

$$HO^{\bullet} + H_2O_2 \rightarrow HO_2^{\bullet} \ (k=2.7 \times 10^7\ M^{-1}s^{-1}) \quad (4.55)$$

$$SO_4^{\bullet-} + S_2O_8^{2-} \rightarrow SO_4^{2-} + S_2O_8^{-\bullet} \ (k=6.6 \times 10^5\ M^{-1}s^{-1}) \quad (4.56)$$

$$HO^{\bullet} + HO^{\bullet} \rightarrow H_2O_2 \ (k=5.5 \times 10^9\ M^{-1}s^{-1}) \quad (4.57)$$

$$SO_4^{\bullet-} + SO_4^{\bullet-} \rightarrow S_2O_8^{2-} \ (k=3.1 \times 10^8\ M^{-1}s^{-1}) \quad (4.58)$$

4.4.3 Effect of pH

Experiments were carried out to evaluate the effect of pH ranging from 3 to 11. As shown in **Figure 4.14**, the impact of pH on direct UV photolysis of AZA is negligible, whereas the degradation efficiency of AZA decreases with the increasing pH in both UV-AOPs.

In the UV/H_2O_2 system, the degradation efficiency of AZA decreases with the increasing pH mainly due to the reduction of $HO^{\bullet}$ oxidation power. As derived from Nernst equation, the redox potential $E_{HO^{\bullet}/H_2O}$ reduces from 2.62 to 2.15 V with pH increasing from 3 to 11. There is a dissociation of $HO^{\bullet}$ at high pH, giving rise to a relatively low reactive radical $O^{\bullet-}$ ($E_{O^{\bullet},H_2O/2OH^{\bullet}}$ =1.78 V) (Buxton et al., 1988). In

addition, alkaline condition also favors the reaction of OH^- and $HO^\bullet$ (Buxton et al., 1988). Less reactive radical, $O^{\bullet-}$, can be generated accordingly, and acts as a strong $HO^\bullet$ scavenger. When pH further increases to 11.6, the predominant form of H_2O_2 in the solution is the hydroperoxide anion HO_2^-, (Tan et al., 2013)), which has a much higher UV_{254} absorption coefficient (240 $M^{-1}cm^{-1}$) than H_2O_2 (19.6 $M^{-1}cm^{-1}$) (Baxendale and Wilson, 1957). HO_2^- can react with $HO^\bullet$ at a 280-time higher rate constant ($k_{HO^\bullet,HO_2^-}$ = 7.5 × 10^9 $M^{-1}s^{-1}$ (Christensen et al., 1982)) compared with H_2O_2 ($k_{H_2O_2,HO_2^-}$ = 2.7 × 10^7 $M^{-1}s^{-1}$ (Buxton et al., 1988)). The scavenging effects of $O^{\bullet-}$ and HO_2^- both account for the lower AZA degradation efficiency at higher pH.

$$HO^\bullet \leftrightarrow H^+ + O^{\bullet-} \ (pK_a=11.9) \quad (4.59)$$

$$HO^\bullet + OH^- \rightarrow H_2O + O^{\bullet-} \ (k=1.2 \times 10^{10}\ M^{-1}s^{-1}) \quad (4.60)$$

$$H_2O_2 \leftrightarrow HO_2^- + H^+ \ (pK_a=11.6) \quad (4.61)$$

$$HO^\bullet + HO_2^- \rightarrow HO^- + HO_2^\bullet \ (k=7.5 \times 10^9\ M^{-1}s^{-1}) \quad (4.62)$$

In the UV/PS system, the degradation efficiency of AZA remains approximately constant in acidic and neutral solutions, and then significantly decreases in basic solutions. This phenomenon can be explained as $SO_4^{\bullet-}$ being the dominant radical species in acidic and neutral solutions, for the negligible reaction between $SO_4^{\bullet-}$ and H_2O (Neta et al., 1977). With further increasing pH, $HO^\bullet$ is generated via the reaction between $SO_4^{\bullet-}$ and OH^-, and gradually plays a dominant role (Neta et al., 1977). As discussed before, $HO^\bullet$ shows a slower rate towards AZA degradation, resulting in an obvious decrease of AZA degradation efficiency under alkali conditions.

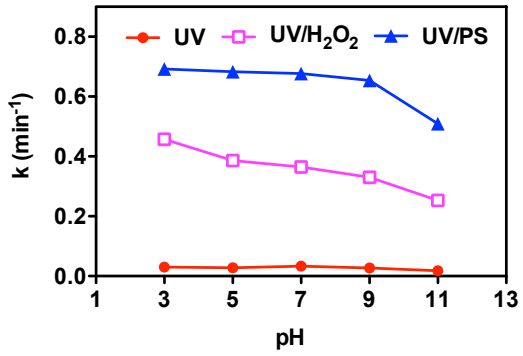

Figure 4.14 Effect of solution pH on AZA degradation rate in the UV, UV/H_2O_2 and UV/PS systems. Experimental conditions: $[AZA]_0$ = 3.3 μM, $[H_2O_2]$ = [PS] = 100 μM.

4.5.5 Effect of water matrix species

As shown in **Figure 4.15**, the presence of HA leads to a significant decrease of AZA degradation efficiency in the three processes. The main reason can be explained as NOM absorbing UV photons and thus reduces UV transmittance in the photoreactor. Compared with the control, the addition of 10 mg L^{-1} HA decreases AZA degradation rate constant from 0.365 to 0.172 min^{-1} (53% reduction) and from 0.677 to 0.384 min^{-1} (43% reduction) in the UV/H_2O_2 and UV/PS systems, respectively. It indicates that the inhibitory effect of NOM in the UV/H_2O_2 system is stronger compared with that in the UV/PS system. The plausible reason can be due to NOM also acting as a radical scavenger with a faster reaction rate with $HO^{\bullet}$ ($k_{HO^{\bullet},NOM}$ = 2.23 × 10^8 $M^{-1}s^{-1}$) (David Gara et al., 2009), which is 37 times larger than that with $SO_4^{\bullet-}$ ($k_{SO_4^{\bullet-},NOM}$ = 6 × 10^6 $M^{-1}s^{-1}$) (Westerhoff et al., 2007). The lower scavenging effect of NOM in the UV/PS system is probably due to the high selectivity of $SO_4^{\bullet-}$ towards AZA.

$$NOM + HO^{\bullet} \rightarrow Products\ (k=2.23 \times 10^8\ M^{-1}s^{-1}) \quad (4.63)$$

$$NOM + SO_4^{\bullet-} \rightarrow Products\ (k=6 \times 10^6\ M^{-1}s^{-1}) \quad (4.64)$$

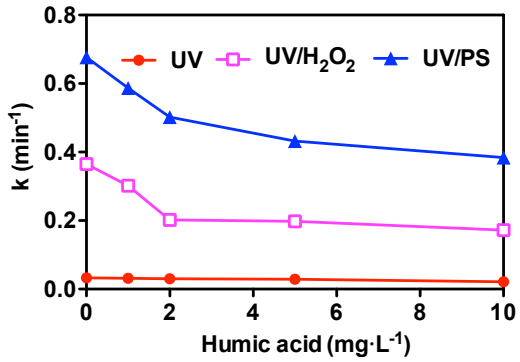

Figure 4.15 Effect of NOM on AZA degradation rate. Experimental conditions: $[AZA]_0$ = 3.3 μM, $[H_2O_2]$ = [PS] = 100 μM, pH=7.

Since inorganic anions, such as chloride (Cl^-), bicarbonate (HCO_3^-), nitrate (NO_3^-) and sulfate (SO_4^{2-}), are ubiquitous in natural water, an investigation was conducted to examine the effect of inorganic anions on AZA photodegradation at neutral condition. As shown in **Figure 4.16**, the degradation efficiencies in both AOPs are significantly inhibited by HCO_3^-, followed by Cl^-, while NO_3^- and SO_4^{2-} exhibits negligible influence.

The significant inhibitive effect of AZA photodegradation induced by HCO_3^- is due to the reaction of HCO_3^- with radicals. The addition of 4 mM HCO_3^- reduces the AZA degradation rate by 49% and 35% in the UV/H_2O_2 and UV/PS systems, respectively, indicating the stronger inhibition effect of HCO_3^- in the UV/H_2O_2 system. The plausible reason can be explained as follows. HCO_3^- can be converted to CO_3^{2-} to reach the HCO_3^--CO_3^{2-} equilibration, and both HCO_3^- and CO_3^{2-} greatly competes with radicals as strong scavengers. The reaction rate of HCO_3^- with $HO^\bullet$ ($k_{HO^\bullet,HCO_3^-}$ = 8.5 × 10^6 $M^{-1}s^{-1}$) (Buxton et al., 1988) is 3 times higher than with $SO_4^{\bullet-}$ ($k_{SO_4^{\bullet-},HCO_3^-}$ = 2.8 × 10^6 $M^{-1}s^{-1}$) (Huie and Clifton, 1990), while the reaction rate of CO_3^{2-} with $HO^\bullet$ ($k_{HO^\bullet,CO_3^{2-}}$ = 3.9 ×10^8 $M^{-1}s^{-1}$) (Buxton et al., 1988) is approximately 65 times higher than that of CO_3^{2-} with $SO_4^{\bullet-}$ ($k_{SO_4^{\bullet-},CO_3^{2-}}$ = 6.1 × 10^6 $M^{-1}s^{-1}$) (Zuo et al., 1999).

As a result, the influence of HCO_3^- is less significant in the UV/PS system.

$$H_2O + CO_2 \leftrightarrow HCO_3^- + H^+ \text{ (pKa=6.37)} \quad (4.65)$$

$$HCO_3^- \leftrightarrow CO_3^{2-} + H^+ \text{ (pKa=10.33)} \quad (4.66)$$

$$HCO_3^- + HO^\bullet \rightarrow CO_3^{\bullet-} + H_2O \text{ (k=8.5 } \times 10^6 \text{ } M^{-1}s^{-1}) \quad (4.67)$$

$$CO_3^{2-} + HO^\bullet \rightarrow CO_3^{\bullet-} + OH^- \text{ (k=3.9 } \times 10^8 \text{ } M^{-1}s^{-1}) \quad (4.68)$$

$$HCO_3^- + SO_4^{\bullet-} \rightarrow HCO_3^\bullet + SO_4^{2-} \text{ (k=2.8 } \times 10^6 \text{ } M^{-1}s^{-1}) \quad (4.69)$$

$$CO_3^{2-} + SO_4^{\bullet-} \rightarrow CO_3^{\bullet-} + SO_4^{2-} \text{ (k=6.1 } \times 10^6 \text{ } M^{-1}s^{-1}) \quad (4.70)$$

The presence of Cl^- exhibits negative influence on AZA degradation rate in both UV-AOP systems. Cl^- can trap both $HO^\bullet$ and $SO_4^{\bullet-}$ to form less reactive species ($ClOH^{\bullet-}$, $Cl^\bullet$ and $Cl_2^{\bullet-}$) depending on the pH condition and species concentrations, resulting in a decreased AZA degradation efficiency (Buxton et al., 1988; Neta et al., 1988). In addition, Cl^- reacts with $SO_4^{\bullet-}$ at a much slower reaction rate ($k_{SO_4^{\bullet-},Cl^-} = 3.1 \times 10^8 \text{ } M^{-1}s^{-1}$) (Chawla and Fessenden, 1975) compared with that of $HO^\bullet$ ($k_{HO^\bullet,Cl^-} = 4.3 \times 10^9 \text{ } M^{-1}s^{-1}$) (Buxton et al., 1988), which explains the influence of 4 mM Cl^- is less significant in the UV/PS system (31% reduction in k_t) than in the UV/H_2O_2 system (25% reduction in k_t). Further reactions of $Cl^\bullet$ in water and $ClOH^{\bullet-}$ decomposition can also lead to the yield of $HO^\bullet$, resulting in an enhanced AZA degradation efficiency. Therefore, the influence of Cl^- is less significant than that of HCO_3^-, despite the fast reaction rate constants of Cl^- with both radicals. The negligible influence of NO_3^- and SO_4^{2-} can be ascribed to their slow reaction rates with radicals (Buxton et al., 1988; Logager et al., 1993; Neta et al., 1988).

$$Cl^- + HO^\bullet \rightarrow ClOH^{\bullet-} \text{ (k= 4.3 } \times 10^9 \text{ } M^{-1}s^{-1}) \quad (4.71)$$

$$ClOH^{\bullet-} + H^+ \rightarrow Cl^\bullet + H_2O \text{ (k= 3 } \times 10^{10} \text{ } M^{-1}s^{-1}) \quad (4.72)$$

$$ClOH^{\bullet-} + Cl^- \rightarrow Cl_2^{\bullet-} + OH^- \text{ (k= 1.0 } \times 10^5 \text{ } M^{-1}s^{-1}) \quad (4.73)$$

$$ClOH^{\bullet-} \rightarrow Cl^- + HO^\bullet \ (k = 6.0 \times 10^9\ M^{-1}s^{-1}) \quad (4.74)$$

$$Cl^- + SO_4^{\bullet-} \rightarrow Cl^\bullet + SO_4^{2-} \ (k = 3.1 \times 10^8\ M^{-1}s^{-1}) \quad (4.75)$$

$$Cl^\bullet + H_2O \rightarrow H^+ + HO^\bullet + Cl^- \ (k = 2.5 \times 10^5\ M^{-1}s^{-1}) \quad (4.76)$$

$$NO_3^- + SO_4^{\bullet-} \rightarrow NO_3^\bullet + SO_4^{2-} \ (k = 5 \times 10^4 \quad (4.77)$$

$$SO_4^{2-} + HO^\bullet \rightarrow SO_4^{\bullet-} + OH^- \ (k = 3.5 \times 10^5 \quad (4.78)$$

$$SO_4^{2-} + SO_4^{\bullet-} \rightarrow S_2O_8^{2-} + e_{aq}^- \quad (4.79)$$

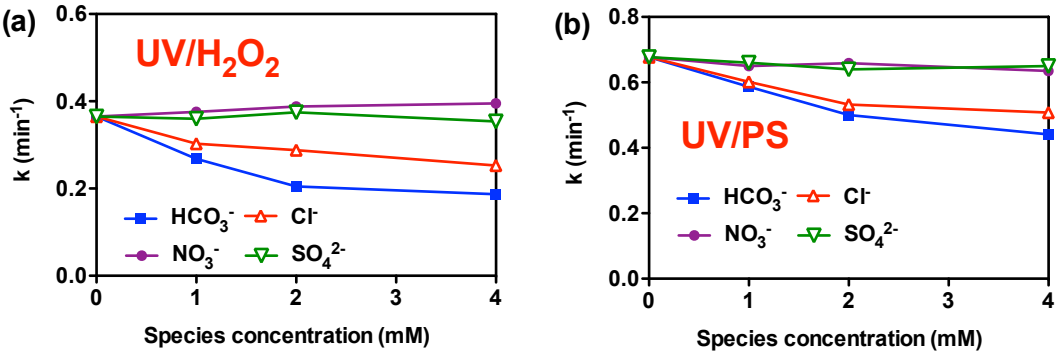

Figure 4.16 Effect of inorganic anions on AZA degradation rate in the (a) UV/H_2O_2 and (b) UV/PS systems. Experimental conditions: $[AZA]_0$ = 3.3 μM, $[H_2O_2]$ = [PS] = 100 μM, pH=7.

4.5.6 Degradation of AZA in natural water

The AZA degradation efficiency in two different types of real water, namely treated water from a water treatment plant and secondary effluent from a wastewater treatment plant, was used to assess the performance of the three treatment processes in practical applications. The characteristics of different water types are presented in **Table 3.1**. As shown in **Figure 4.17**, the degradation rate of AZA in treated water is comparable to that in deionized water, but decreases significantly in secondary effluent, which suggests the competing side reactions of radicals with the background species of secondary effluent. UV shielding effect induced by the high turbidity of secondary effluent (5.3 NTU) may inhibit the UV photolysis of H_2O_2 and PS, while

its high TOC concentration (10.6 mg L^{-1}) and Cl^- concentration (146 mg L^{-1}) may also result in radical scavenging effects.

The AZA degradation rate constant decreases by a factor of 2.7 and 1.9 in the SE for UV/H_2O_2 and UV/PS treatment, respectively, indicating that AZA degradation is less affected in the UV/PS system. The result is consistent with preceding discussion on the impact of water matrices. As a result, UV/PS is more suitable than UV/H_2O_2 for treating waters containing with high TOC or total dissolved solids.

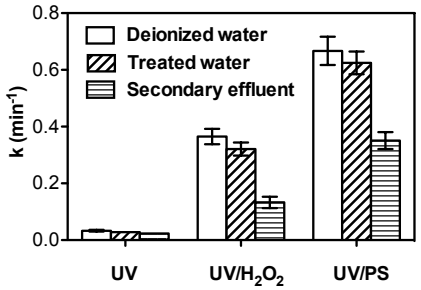

Figure 4.17 Effect of different types of water on AZA degradation rate. Experimental conditions: $[AZA]_0$ = 3.3 μM, $[H_2O_2]$ = [PS] = 100 μM.

4.5.7 Proposed degradation pathways

$HO^{\bullet}$ attacks various organic compounds non-selectively through electron transfer, hydrogen abstraction or electrophilic addition reactions (Baxendale and Wilson, 1957), while $SO_4^{\bullet-}$ is more selective for electron transfer reactions (Buxton et al., 1988). As a result, the degradation by-products generated in the two UV-AOPs are different. Based on the by-products identified by LC/MS/MS (Appendix 11), the potential AZA degradation pathways are proposed in **Figure 4.18**, namely hydroxylation (+16 Da) and demethylation (-14 Da). As shown in Appendix 11, the detection of intermediates with an m/z of 294 indicates that AZA hydroxylation can take place in the presence of either $HO^{\bullet}$ or $SO_4^{\bullet-}$. $HO^{\bullet}$ can attack carbon atom at the purine ring to form hydroxyl adduct $(AZA\text{-}OH)^{\bullet}$, followed by the deprotonation to form AZA=O. During a $SO_4^{\bullet-}$-induced oxidation, electron transfer is typically the major oxidation mechanism (Antoniou et al., 2010). $SO_4^{\bullet-}$ can attack AZA to form

radical cation $AZA^{\bullet+}$ by electron transfer, followed by the formation of AZA=O through deprotonation and oxidization (**Figure 4.19**).

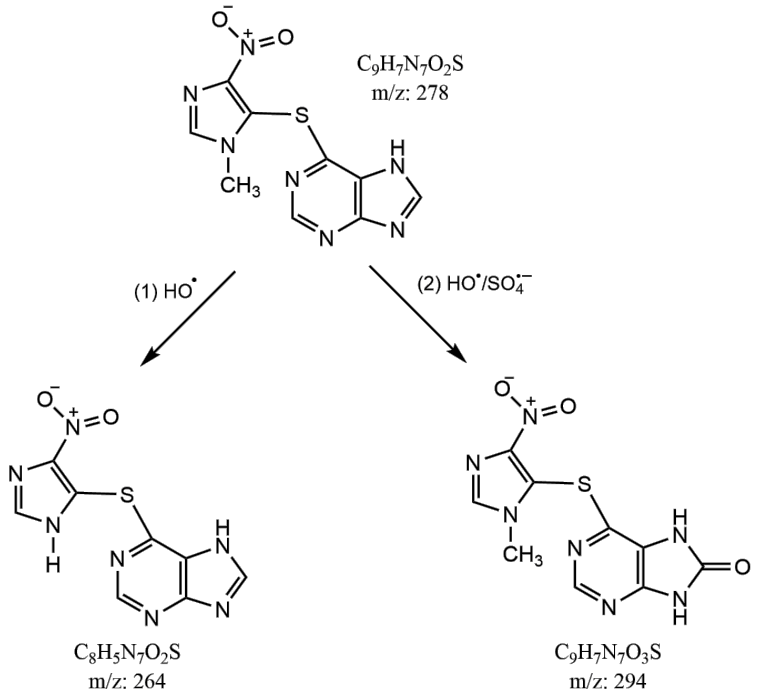

Figure 4.18 Proposed degradation pathways of AZA through its reaction with $HO^{\bullet}$ and $SO_4^{\bullet-}$.

In addition, another intermediate with an m/z of 264 is also detected in the UV/H_2O_2 system, which indicates another pathway for AZA degradation via $HO^{\bullet}$ oxidation. Carbon-centered radical is generated through the hydrogen abstraction by $HO^{\bullet}$ from the methyl side chain. Therefore, AZA photodegradation by $HO^{\bullet}$ may also involve an electron release and hydrolysis, leading to the generation of AZA hydroxymethyl intermediate compound. The resulting demethylated compound is formed due to the elimination of hydroxymethyl groups from the intermediate (**Figure 4.19**) (Sunil Paul et al., 2014).

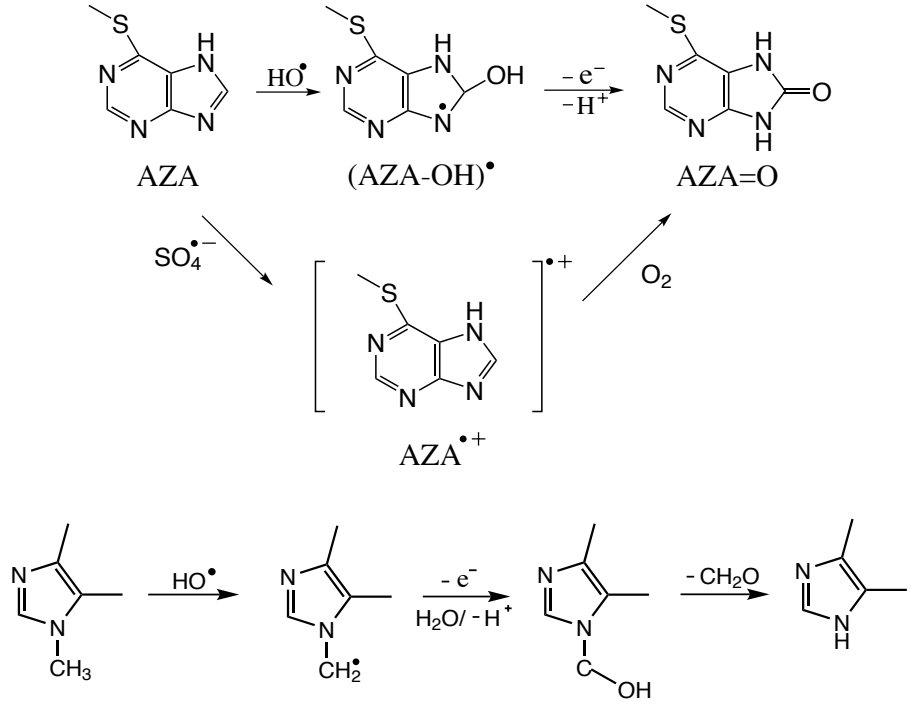

Figure 4.19 Mechanism of the hydroxylation and demethylation.

4.5.8 Economic comparison of UV/H_2O_2 and UV/PS processes

Total cost per order (*Cost/O*$_{total}$) is utilized in this study as an indicator of the cost-effectiveness of the three treatment processes. *Cost/O*$_{total}$ ($\cdot m^{-3} \cdot order^{-1}$) is defined as the total cost required to remove a specific pollutant by one order of magnitude in 1 m^3 polluted water, which includes the cost of electrical energy (*Cost/O*$_{UV}$) and oxidants (*Cost/O*$_{ox}$). *Cost/O*$_{ox}$ is calculated from the oxidant dose and the oxidant price, while *Cost/O*$_{UV}$ is determined according to the electrical energy per order (*EE/O*$_{UV}$) with an additional 45% real UV system application maintenance cost (Khan et al., 2014):

$$Cost/O_{total} = Cost/O_{UV} + Cost/O_{ox} \tag{4.80}$$

$$EE/O_{UV} = \frac{1.45Pt}{V\log(\frac{C_i}{C_f})} = \frac{5.57\times10^{-2}P}{Vk}(\mathrm{kWh\cdot m^{-3}\cdot order^{-1}}) \tag{4.81}$$

$$Cost/O_{UV}\ (\$\cdot m^{-3}\cdot order^{-1}) = EE/O_{UV}\ (kWh\cdot m^{-3}\cdot order^{-1}) \times \text{electricity cost}\ (\$\cdot kWh^{-1}) \tag{4.82}$$

where P is the UV lamp output power (kW), t is the degradation time (h), V is the volume (m^3) of treated water, k is the first order rate constant (min^{-1}); C_i and C_f are the initial and final concentrations ($mg \cdot L^{-1}$) of AZA, respectively.

Table 4.3 Economic comparison for AZA degradation in the UV, UV/H_2O_2 and UV/PS systems in deionized water, treated water, and secondary effluent. Experimental conditions: $[AZA]_0$ = 3.3 μM , $[H_2O_2]$ = [PS] = 100 μM.

	Deionized water			Treated water			Secondary effluent		
	UV	UV/H_2O_2	UV/PS	UV	UV/H_2O_2	UV/PS	UV	UV/H_2O_2	UV/PS
k (min^{-1})	0.033	0.365	0.677	0.028	0.321	0.625	0.023	0.133	0.351
EE/O_{UV} ($kWh \cdot m^{-3} \cdot order^{-1}$)	8.44	0.76	0.41	9.94	0.87	0.45	12.10	2.09	0.79
$Cost/O_{UV}$ ($\$ \cdot m^{-3} \cdot order^{-1}$)*	0.844	0.076	0.041	0.994	0.087	0.045	1.210	0.209	0.079
$Cost/O_{ox}$ ($\$ \cdot m^{-3} \cdot order^{-1}$) **	0	0.002	0.026	0	0.002	0.026	0	0.002	0.026
$Cost/O_{total}$ ($\$ \cdot m^{-3} \cdot order^{-1}$)	0.844	0.078	0.067	0.994	0.089	0.071	1.210	0.211	0.105

*Electricity price: US\$0.10 kWh^{-1} (U.S. Energy Information Administration, 2015)

**Chemical price: US\$1.5 kg^{-1} for H_2O_2 and US\$0.74 kg^{-1} for PS (Zhang et al., 2014)

According to **Table 4.3**, the addition of 100 μM H_2O_2 or PS to UV photoreactor significantly decreases the $Cost/O_{total}$ from 0.844 to 0.078 or 0.067 $\$ \cdot m^{-3} \cdot order^{-1}$, namely 11-time or 13-time decrease, respectively. The $Cost/O_{total}$ for the UV/PS process in deionized water, treated water, and secondary effluent are 0.067, 0.071 and 0.105 $\$ \cdot m^{-3} \cdot order^{-1}$, respectively, at an oxidant dose of 100 μM.

Figure 4.20 indicates that oxidant concentration shows a significant effect on the $Cost/O_{total}$. For example, the $Cost/O_{total}$ significantly reduces from 0.844 to 0.056 $\$ \cdot m^{-3} \cdot order^{-1}$ with increasing PS concentration from 0 to 200 μM, and increases to 0.359 $\$ \cdot m^{-3} \cdot order^{-1}$ with further increase of PS concentration to 2000 μM. The reasons for the reverse trend may be due to the self-scavenging of the oxidant as well as the high chemical cost. The $Cost/O_{total}$ for the UV/PS process is relatively lower

than that for the UV/H_2O_2 process at low oxidant dose, and becomes higher when the oxidant dose is over 200 μM. Since low oxidant dose is sufficient for a complete degradation of the target pollutant, UV/PS process is more cost-efficient than UV/H_2O_2 process.

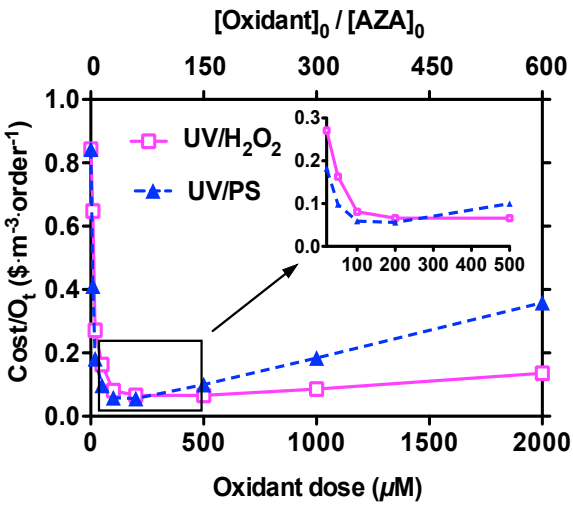

Figure 4.20 Cost/O_{total} comparison for AZA degradation for the UV/AOP processes in deionized water as a function of the oxidant molar concentration. Experimental conditions: $[AZA]_0$ = 3.3 μM, pH=7.

4.6 Conclusions

This chapter compares the photodegradation of eight CSDs by direct UV photolysis, UV/H_2O_2, and UV/PS processes. The relatively low removal efficiency of CSDs indicates that direct UV photolysis exhibits insignificant degradation effect towards most of the CSDs. UV combined with oxidants to form highly reactive radicals could be the more effective strategy for elimination of CSDs in water. The degradation effect of CSDs increases linearly with the increasing oxidant dose at low level, while the excess H_2O_2 can act as radical scavengers. NOM shows negative effect on direct UV photodegradation, while the addition of NO_3^- increases the photodegradation effect of chemicals by generating HO•. In contrast, the degradation efficiency of CSDs is significantly affected by the pH, NOM, HCO_3^-, and Cl^- in both UV-AOP systems. Compared with UV/H_2O_2, UV/PS is less affected by the common water matrix species in the natural water. The mechanism of UV photolysis is to

induce the cleavage of aromatic ring in the compound, while the mechanisms of NO_3^--induced and DOM-induced photolysis are through radical addition reaction and electron transfer reaction, respectively. Hypothetical degradation pathways of UV/AOPs are also proposed based on the identified by-products. The total treatment cost per order for the three treatment systems are compared, indicating that UV/PS system is the most cost-effective process among the three UV-based technologies for AZA degradation.

Chapter 5 Comparison of amoxicillin photodegradation by UV/H_2O_2 and UV/persulfate: Reaction kinetics, degradation pathways, and antibacterial activity

5.1 Introduction

Previous chapter simply investigates the degradation efficiency of UV, UV/H_2O_2 and UV/PS for CSDs photodegradation in water. This chapter provides a more systematic comparison of UV/H_2O_2 and UV/PS processes on AMX degradation, including the reaction kinetics, degradation pathways, and antibacterial activity. AMX was chosen as a target compound because of its frequent use and high toxicity. The degradation efficiency of AMX during UV/H_2O_2 and UV/PS processes was calculated. The respective contributions of UV, $HO^{\bullet}$, and $SO_4^{\bullet-}$ in the UV/PS process were also determined. The degradation pathways of AMX by UV/AOPs were proposed according to the LC/MSMS results substantiated with the frontier electron densities calculation. The antibacterial activity of AMX in the two UV/AOP systems was evaluated.

5.2 Reaction kinetics

5.2.1 Degradation of AMX by UV, UV/H_2O_2, and UV/PS processes

According to **Figure 5.1**, AMX can be insignificantly removed by direct UV photolysis, which can be ascribed by its low quantum yield of 9.74×10^{-3} mol E^{-1}. However, the first-order rate constant of AMX in the UV photolysis system increases significantly from 0.09 to 0.73 and 1.22 min^{-1}, with the addition of 500 μM H_2O_2 or PS, respectively. The TOC removal of AMX after 30 min treatment also increases from 4.7% (UV photolysis) to 15.2% (UV/H_2O_2) and then to 28.7% (UV/PS). The effect of the initial oxidant concentrations was also evaluated and compared. Overall, the degradation efficiency of AMX follows the order of UV/PS > UV/H_2O_2 > UV

photolysis.

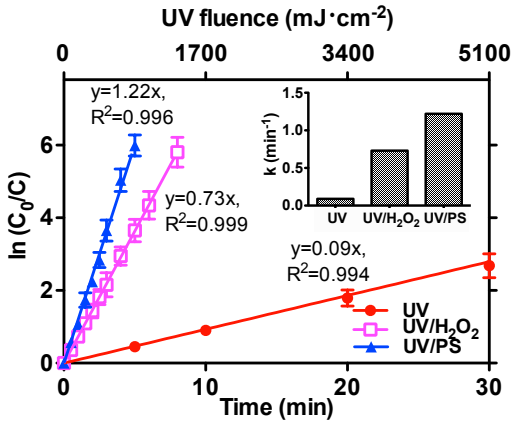

Figure 5.1 Degradation of AMX by UV, UV/H_2O_2, and UV/PS processes. Experimental conditions: $[AMX]_0$ = 20 μM, $[H_2O_2]$ = [PS] = 500 μM, pH = 7.

5.2.2 Second-order rate constants of AMX with HO• and $SO_4^{\bullet-}$

The degradation of AMX in the UV/H_2O_2 system can be expressed according to the pseudo-first-order kinetics (Equation 5.1):

$$-\frac{d[\mathrm{AMX}]}{dt} = k_{\mathrm{obs,UV/H_2O_2,AMX}}[\mathrm{AMX}] \tag{5.1}$$

where $k_{\mathrm{obs,UV/H_2O_2,AMX}}$ is the overall first-order rate constant for AMX degradation in the UV/H_2O_2 system (s^{-1}).

The overall degradation of AMX consists direct UV photolysis and indirect HO•-assisted photolysis in the UV/H_2O_2 system (Equation 5.2), which can be further expressed according to the second-order rate constant of AMX and HO• (Equation 5.3).

$$k_{\mathrm{obs,UV/H_2O_2,AMX}} = k_{\mathrm{obs,UV,AMX}} + k_{\mathrm{obs,HO^\bullet,AMX}} \tag{5.2}$$

$$k_{\mathrm{obs,UV/H_2O_2,AMX}} = k_{\mathrm{obs,UV,AMX}} + k_{\mathrm{HO^\bullet,AMX}}[\mathrm{HO^\bullet}]_{\mathrm{UV/H_2O_2}} \tag{5.3}$$

where $k_{\mathrm{obs,UV,AMX}}$ is the first-order rate constant for AMX degradation by direct UV

photolysis in the UV/H_2O_2 system (s^{-1}); $k_{obs,HO^{\bullet},AMX}$ is the first-order rate constant for AMX degradation by indirect $HO^{\bullet}$-assisted photolysis in the UV/H_2O_2 system (s^{-1}); $k_{HO^{\bullet},AMX}$ is the second-order rate constant of $HO^{\bullet}$ reacting with AMX ($M^{-1}s^{-1}$); $[HO^{\bullet}]_{UV/H_2O_2}$ is the steady-state concentration of $HO^{\bullet}$ in the UV/H_2O_2 system (M).

*p*CBA was used as the reference compound in the parallel studies to determine $k_{HO^{\bullet},AMX}$, on the basis of its known second-order rate constant with $HO^{\bullet}$ ($k_{HO^{\bullet},pCBA}$ = 5×10^9 M^{-1} s^{-1}) (Buxton et al., 1988). The degradation of *p*CBA in the UV/H_2O_2 system can be expressed as Equation 5.4.

$$k_{obs,UV/H_2O_2,pCBA} = k_{obs,UV,pCBA} + k_{HO^{\bullet},pCBA}[HO^{\bullet}]_{UV/H_2O_2} \quad (5.4)$$

$$k_{HO^{\bullet},AMX} = \frac{k_{obs,UV/H_2O_2,AMX} - k_{obs,UV,AMX}}{k_{obs,UV/H_2O_2,pCBA} - k_{obs,UV,pCBA}} k_{HO^{\bullet},pCBA} \quad (5.5)$$

where $k_{obs,UV,pCBA}$ and $k_{obs,UV/H_2O_2,pCBA}$ are the first-order rate constants for *p*CBA degradation in the UV and UV/H_2O_2 systems, respectively (s^{-1}); $k_{HO^{\bullet},pCBA}$ is the second-order rate constant of $HO^{\bullet}$ reacting with *p*CBA (M^{-1} s^{-1}).

The degradation of AMX in the UV/PS system can be expressed according to the pseudo-first-order kinetics (Equation 5.6):

$$-\frac{d[AMX]}{dt} = k_{obs,UV/PS,AMX}[AMX] \quad (5.6)$$

where $k_{obs,UV/PS,AMX}$ is the overall first-order rate constant of AMX in UV/H_2O_2 system (s^{-1}).

Due to the co-occurrence of both $HO^{\bullet}$ and $SO_4^{\bullet-}$ in the UV/PS system (Equation 5.7), The overall degradation of AMX consists direct UV photolysis, as well as indirect $HO^{\bullet}$-assisted and $SO_4^{\bullet-}$-assisted photolysis in the UV/PS system (Equation 5.8), which can be further expressed according to Equation 5.9.

$$SO_4^{\bullet-} + H_2O \rightarrow HO^{\bullet} + SO_4^{2-} + H^+ \text{ (pH=7)} \quad (5.7)$$

$$k_{obs,UV/PS,AMX} = k_{obs,UV,AMX} + k_{obs,HO^{\bullet},AMX} + k_{obs,SO_4^{\bullet-},AMX} \quad (5.8)$$

$$k_{obs,UV/PS,AMX} = k_{obs,UV,AMX} + k_{HO^{\bullet},AMX}[HO^{\bullet}]_{UV/PS} + k_{SO_4^{\bullet-},AMX}[SO_4^{\bullet-}]_{UV/PS} \quad (5.9)$$

where $k_{obs,UV,AMX}$ is the first-order rate constant for AMX degradation by direct UV photolysis in the UV/PS system (s^{-1}), $k_{obs,HO^{\bullet},AMX}$ and $k_{obs,SO_4^{\bullet-},AMX}$ are the first-order rate constants for AMX degradation by indirect $HO^{\bullet}$-assisted and $SO_4^{\bullet-}$-assisted photolysis in the UV/PS system, respectively (s^{-1}), $k_{SO_4^{\bullet-},AMX}$ is the second-order rate constant of $SO_4^{\bullet-}$ reacting with AMX ($M^{-1}\ s^{-1}$), $[HO^{\bullet}]_{UV/PS}$ and $[SO_4^{\bullet-}]_{UV/PS}$ are the steady-state concentrations of $HO^{\bullet}$ and $SO_4^{\bullet-}$ in the UV/PS system, respectively (M).

Even though $SO_4^{\bullet-}$ is predominant in the UV/PS system, the degradation effect of $OH^{\bullet}$ oxidation cannot be neglected. As a result, *t*-BuOH was used as the $HO^{\bullet}$ quenching reagent in the UV/PS system, since its reactivity with $HO^{\bullet}$ ($k_{HO^{\bullet},t-BuOH} = 6 \times 10^8\ M^{-1}\ s^{-1}$) is 3-order of magnitude higher than that with $SO_4^{\bullet-}$ ($k_{SO_4^{\bullet-},t-BuOH} = 8.4 \times 10^5\ M^{-1}\ s^{-1}$) (Clifton and Huie, 1989). Due to the scavenging of $HO^{\bullet}$ using *t*-BuOH in the UV/PS system, Equation 5.9 can be simplified to Equation 5.10.

$$k_{obs,UV/PS,AMX} = k_{obs,UV,AMX} + k_{SO_4^{\bullet-},AMX}[SO_4^{\bullet-}]_{UV/PS} \quad (5.10)$$

*m*TA, with a known second-order rate constant with $SO_4^{\bullet-}$ ($k_{SO_4^{\bullet-},mTA} = 2 \times 10^9\ M^{-1}\ s^{-1}$) (Neta et al., 1977), was used as the reference compound in the parallel studies to determine $k_{SO_4^{\bullet-},AMX}$. Similarly, the degradation of *m*TA in the UV/PS system can be expressed as Equations 5.11 and 5.12,

$$k_{\text{obs,UV/PS,}m\text{TA}} = k_{\text{obs,UV,}m\text{TA}} + k_{SO_4^{\bullet-},m\text{TA}}[SO_4^{\bullet-}]_{\text{UV/PS}} \quad (5.11)$$

$$k_{SO_4^{\bullet-},\text{AMX}} = \frac{k_{\text{obs,UV/PS,AMX}} - k_{\text{obs,UV,AMX}}}{k_{\text{obs,UV/PS,}m\text{TA}} - k_{\text{obs,UV,}m\text{TA}}} k_{SO_4^{\bullet-},m\text{TA}} \quad (5.12)$$

where $k_{\text{obs,UV,}m\text{TA}}$ and $k_{\text{obs,UV/PS,}m\text{TA}}$ are the first-order rate constants for *m*TA degradation in the UV and UV/PS systems, respectively (s^{-1}); $k_{SO_4^{\bullet-},m\text{TA}}$ is the second-order rate constant of $SO_4^{\bullet-}$ reacting with *m*TA ($M^{-1}\ s^{-1}$).

According to Equations 5.5 and 5.12, $k_{HO^{\bullet},\text{AMX}}$ *and* $k_{SO_4^{\bullet-},\text{AMX}}$ are determined to be $3.9 \times 10^9\ M^{-1}\ s^{-1}$ and $3.5 \times 10^9\ M^{-1}\ s^{-1}$, respectively (**Figure 5.2**), which are typical for antibiotics (Dail and Mezyk, 2010; Rickman and Mezyk, 2010). Due to the comparable second-order rate constants in the two UV/AOP systems, other factors can be ascribed to the significant difference of AMX degradation efficiency. First of all, $SO_4^{\bullet-}$ has a longer lifetime (30-40 μs) compared with that of $HO^{\bullet}$ (in the order of 100 ns) (Buxton et al., 1988). $HO^{\bullet}$ can react with many constituents with almost diffusion-controlled rate constant and therefore, it is considered to be a non-selective oxidant with a short lifetime, while $SO_4^{\bullet-}$ is more selective. In addition, the quantum yield and the molar absorption coefficient of PS (Φ_{254} = 1.4-1.8 mol E^{-1}, ε_{254} = 20.0 $M^{-1}\ cm^{-1}$) are much higher compared with those of H_2O_2 (Φ_{254} = 1.0 mol E^{-1}, ε_{254} = 19.6 $M^{-1}\ cm^{-1}$) under UV-254 irradiation, leading to a higher radical production.

In order to evaluate the efficiency of the two UV/AOP processes, the degradation kinetics of AMX with $HO^{\bullet}$ and $SO_4^{\bullet-}$ were compared with other treatment processes at neutral pH. As shown in **Table 5.1**, the second-order rate constants of

AMX with various oxidants are in the order of $HO^{\bullet}$ > $SO_4^{\bullet-}$ > bromine > ozone > chlorine > Fe(VI), suggesting that $HO^{\bullet}$ and $SO_4^{\bullet-}$ are among the most effective technologies for AMX removal. Similar trends have also been found by Lee and von Gunten for the oxidation of phenol, aniline, glycine, dimethylamine, and trimethylamine (Lee and Gunten, 2010).

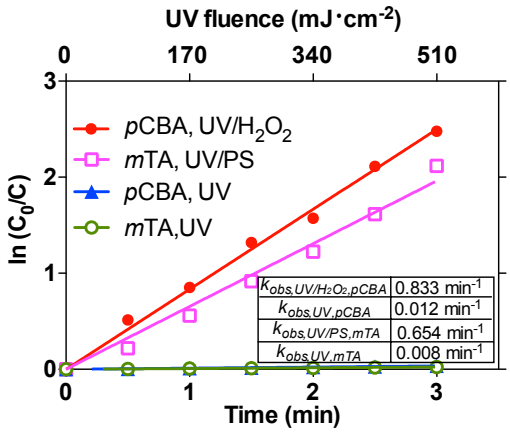

Figure 5.2 Degradation of *p*CBA and *m*TA in the UV, UV/H_2O_2 and UV/PS systems. Experimental conditions: $[AMX]_0 = [pCBA] = [mTA] = 20\ \mu M$, $[H_2O_2] = [PS] = 500\ \mu M$, pH = 7. *t*-BuOH was used as the $HO^{\bullet}$ quenching reagent in the UV/PS system.

Table 5.1 Second-order rate constant of AMX with various oxidants at pH 7.

Oxidant	Second-order rate constant ($M^{-1}s^{-1}$)	Reference
Ferrate(VI)	771	(Karlesa et al., 2014)
Ozone	1.5×10^6	(Andreozzi et al., 2005)
Chlorine	1.19×10^5	(Acero et al., 2010)
Bromine	6.7×10^6	(Benitez et al., 2011)
$HO^{\bullet}$	3.9×10^9	this study
$SO_4^{\bullet-}$	3.5×10^9	this study

5.2.3 Respective contribution of UV, $HO^{\bullet}$, and $SO_4^{\bullet-}$ in the UV/PS process

Since $HO^{\bullet}$ can be produced from $SO_4^{\bullet-}$ and takes part in degrading chemicals in the UV/PS system (He et al., 2014; Xiao et al., 2016), a series of experiments were

conducted to quantify the respective contribution of UV, $HO^{\bullet}$, and $SO_4^{\bullet-}$ in the UV/PS system. NB was chosen as a probe compound to quantify the average steady-state concentration of $HO^{\bullet}$ in the UV/PS system, since its second-order rate constant with $HO^{\bullet}$ ($k_{HO^{\bullet},NB} = 3.9 \times 10^9\ M^{-1}\ s^{-1}$) is 3-orders of magnitude higher than that with $SO_4^{\bullet-}$ ($k_{SO_4^{\bullet-},NB} < 10^6\ M^{-1}\ s^{-1}$) (Buxton et al., 1988; Neta et al., 1988). In addition, *m*TA was used as a probe compound to calculate the average steady-state concentration of $SO_4^{\bullet-}$ in the UV/PS system, since its second-order rate constant with either $HO^{\bullet}$ or $SO_4^{\bullet-}$ is both around $10^9\ M^{-1}\ s^{-1}$ ($k_{HO^{\bullet},mTA} = 7.6 \times 10^9\ M^{-1}\ s^{-1}$ and $k_{SO_4^{\bullet-},mTA} = 2 \times 10^9\ M^{-1}\ s^{-1}$). According to the observed first-order rate constant for NB and *m*TA degradation (**Figure 5.3**), the average steady-state concentration of $HO^{\bullet}$ and $SO_4^{\bullet-}$ were determined to be 1.2×10^{-12} M and 4.1×10^{-12} M in the UV/PS system, respectively (Equations 5.13-5.16). The observed first-order rate constant for AMX degradation by direct UV photolysis, indirect $HO^{\bullet}$-assisted and $SO_4^{\bullet-}$-assisted photolysis in the UV/PS system ($k_{obs,UV,AMX}$, $k_{obs,HO^{\bullet},AMX}$ and $k_{obs,SO_4^{\bullet-},AMX}$) are calculated to be 0.09, 0.28, and 0.86 min^{-1}, respectively. As a result, the percentage contributions of UV photolysis, $HO^{\bullet}$ and $SO_4^{\bullet-}$ for AMX degradation are 7.3%, 22.8%, and 69.9%, respectively. The result shows a predominant contribution of $SO_4^{\bullet-}$ compared with that of UV photolysis and $HO^{\bullet}$, though the contribution of $HO^{\bullet}$ for AMX degradation in the UV/PS system is also non-negligible.

$$k_{obs,UV/PS,NB} = k_{obs,UV,NB} + k_{HO^{\bullet},NB}[HO^{\bullet}]_{UV/PS} + k_{SO_4^{\bullet-},NB}[SO_4^{\bullet-}]_{UV/PS} \quad (5.13)$$

$$[HO^{\bullet}]_{UV/PS} = \frac{k_{obs,UV/PS,NB} - k_{obs,UV,NB}}{k_{HO^{\bullet},NB}} \quad (5.14)$$

$$k_{obs,UV/PS,mTA} = k_{obs,UV,mTA} + k_{HO^{\bullet},mTA}[HO^{\bullet}]_{UV/PS} + k_{SO_4^{\bullet-},mTA}[SO_4^{\bullet-}]_{UV/PS} \quad (5.15)$$

$$[SO_4^{\bullet-}]_{UV/PS} = \frac{k_{obs,UV/PS,mTA} - k_{obs,UV,mTA} - k_{HO^{\bullet},mTA}[HO^{\bullet}]_{UV/PS}}{k_{SO_4^{\bullet-},mTA}} \quad (5.16)$$

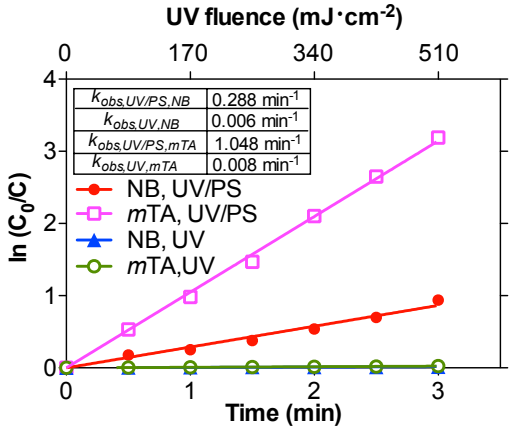

Figure 5.3 Degradation of NB and *m*TA in the UV and UV/PS systems. Experimental conditions: $[AMX]_0 = [NB] = [mTA] = 20\ \mu M$, [PS] = 500 μM, pH = 7.

5.3 Proposed degradation pathway

In order to investigate the degradation mechanism of AMX in the UV/H_2O_2 and UV/PS systems, the degradation pathways of AMX are proposed on the basis of the experimental evidence substantiated with theoretical calculation. The mass spectrum of AMX solution before and after UV/AOP treatment are shown in **Appendix 12**. The by-products identified via LC/MSMS indicate three possible degradation pathways (**Figure 5.4(a)**), including hydroxylation (+16 Da), hydrolysis (+18 Da), and decarboxylation (-44 Da).

The intermediate with m/z of 382 indicates the mono-hydroxylation of AMX. Since hydroxylation can occur at various positions of AMX, theoretical calculations were applied to provide valuable insights into the degradation mechanism as a supplement of LC/MSMS observation. The computational analysis indicates that the

sulfur atom in the thioether molecule of AMX is susceptible to be attacked by electrophilic species (**Figure 5.5(b)**), while the benzene ring is the region exposed to nucleophilic attack (**Figure 5.5(c)**). On the basis of the Frontier Orbital Theory, $SO_4^{\bullet-}$ usually attacks at the regions susceptible to electrophilic species, while $HO^{\bullet}$ attacks at the regions susceptible to both electrophilic and nucleophilic species (An et al., 2015). As a result, it can be inferred that sulfur atom on the thioether groups is susceptible to both $HO^{\bullet}$ and $SO_4^{\bullet-}$ attack, while benzene ring is the reasonable site for $HO^{\bullet}$ attack. Other publications also suggest that $HO^{\bullet}$ oxidation mainly attacks the peripheral aromatic-ring of beta-lactam antibiotics, while $SO_4^{\bullet-}$ oxidation is more inclined to occur adjacent to the beta-lactam moiety (Sharma et al., 2013; Song et al., 2008).

Figures 5.4(b) and **(c)** show the mechanism of the two hydroxylated by-products generation. $HO^{\bullet}$ and $SO_4^{\bullet-}$ are expected to attack the sulfur atom on the thioether groups to yield sulfur centered radical cation by electron transfer. The radicals can be further deprotonated to generate α-thioether radicals, followed by oxidation to yield sulfoxide TP1 (**Figure 5.4(b)**). In comparison, $HO^{\bullet}$ can attack the aromatic ring of the side chain to yield hydroxyl radical, which can be further oxidized to form monohydroxy AMX TP2 (**Figure 5.4(c)**). Moreover, TP1 and TP2 can be further hydroxylated to form the monohydroxy AMX sulfoxide TP3 with m/z of 398 (**Figure 5.4(a)**).

The hydrolysis by-product TP4 with m/z of 384 corresponds to the penicilloic acid ($C_{16}H_{21}N_3O_6S$), which is formed by opening the strained four-membered beta-lactam ring of AMX. The decarboxylation product TP5 with m/z of 340 corresponds to the penicilloic acid derivative ($C_{15}H_{21}N_3O_4S$), which is generated by the subsequent release of the carboxyl group from the penicilloic acid. TP4 can also be hydroxylated at sulfur atom and aromatic ring to generate TP6 and TP7, respectively (Szabó et al., 2016b; Trovó et al., 2011).

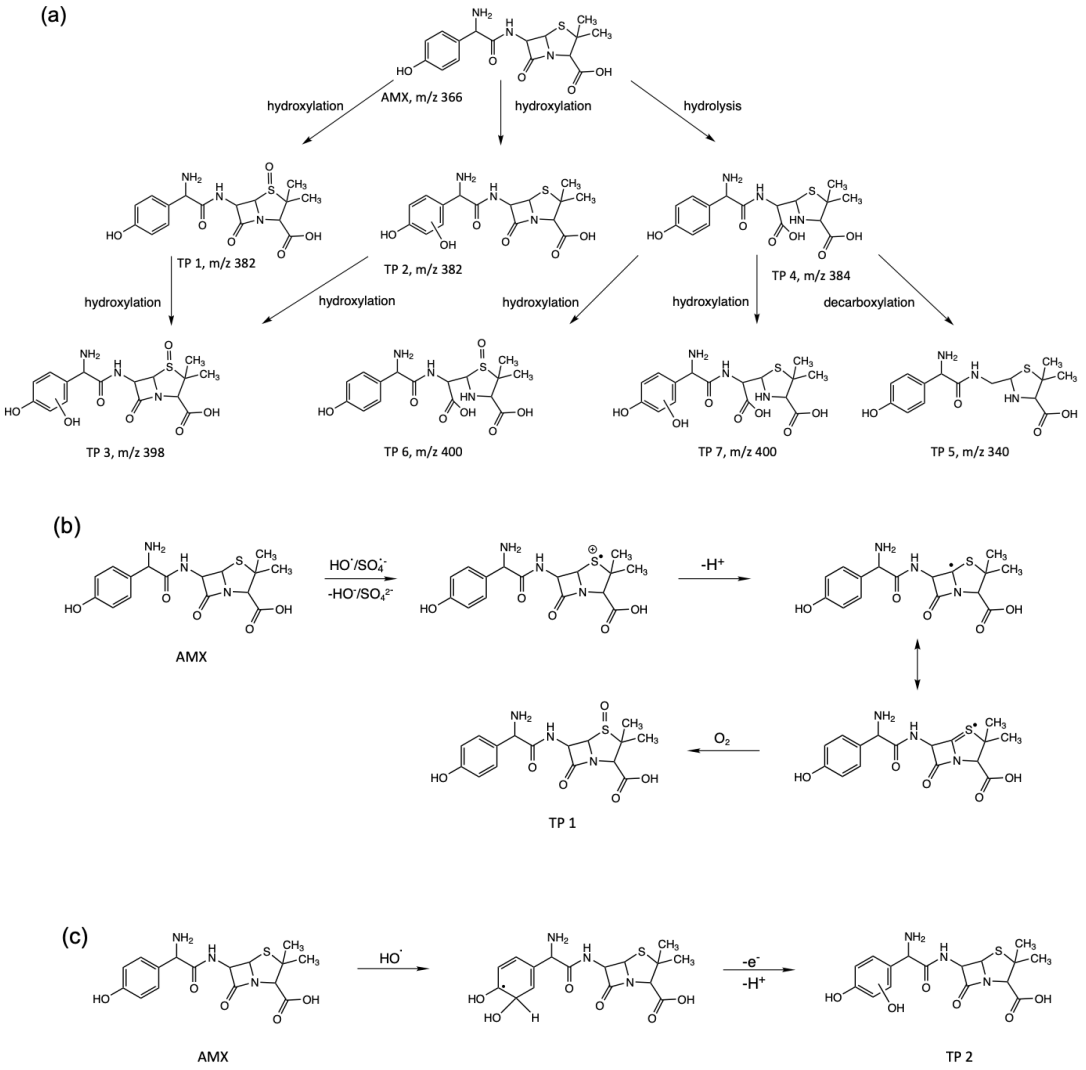

Figure 5.4 Proposed pathway of (a) AMX degradation, (b) TP 1 generation, and (c) TP 2 generation in the UV/H_2O_2 and UV/PS systems.

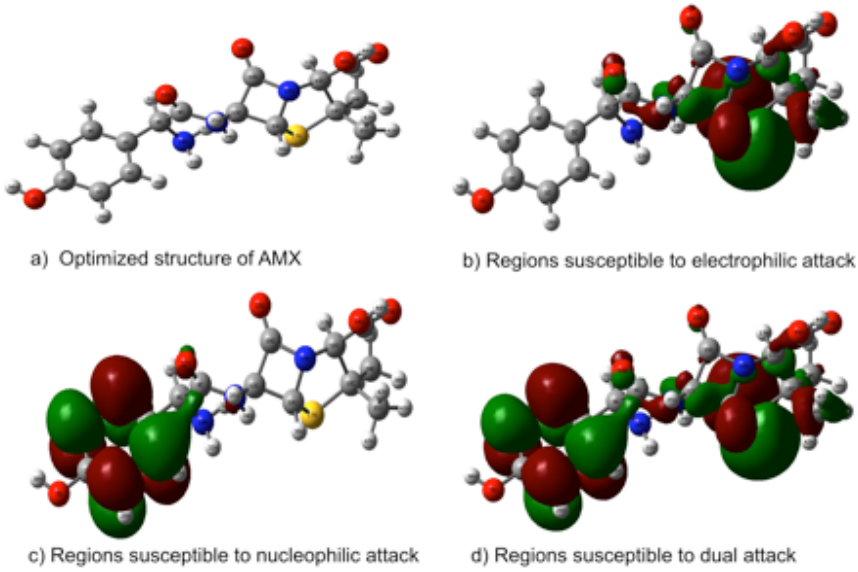

Figure 5.5 Frontier electron densities of AMX for nucleophilic, electrophilic, and dual attack.

5.4 Antibacterial activity

5.4.1 Agar diffusion test

Agar diffusion tests against *E. coli* were conducted using 8 mm-diameter oxford cups to reveal the antibacterial potency change of the AMX degradation by-products after 5 min of UV, UV/H_2O_2, and UV/PS treatment (**Figure 5.6**). The inhibition zone of the UV-treated sample changes insignificantly compared to that of the untreated sample. This can be ascribed by the low degradation efficiency of AMX by direct UV photolysis. In comparison, the inhibition zones significantly disappear for the samples treated after UV/H_2O_2 or UV/PS processes, indicating a complete antibacterial potency removal of AMX by UV/AOPs. In order to achieve quantitative results, a series of growth inhibition tests were carried out.

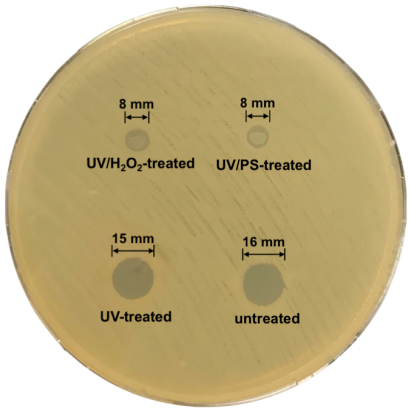

Figure 5.6 Agar diffusion test of untreated, UV-treatment, UV/H_2O_2-treated and UV/PS-treated AMX samples against *E. coli*

5.4.2 Growth inhibition test

Figure 5.7(a) compares the growth inhibition of *E. coli* in the presence of untreated AMX and UV/AOP-treated AMX as a function of AMX concentration. Any by-products in the treated samples that retain antibacterial activity would cause the deviation of inhibition curve from the untreated sample. The agreement in the three data sets and the similar EC_{50} values of the three curves suggest that both UV/H_2O_2 and UV/PS treatment can reduce the antibacterial activity of AMX solution significantly. The unreacted AMX is the only cause of the antibacterial activity for the UV/AOP-treated AMX. A similar observation can be found in *S. aureus* experiment as shown in **Figure 5.7(b)**. The much lower EC_{50} value of *S. aureus* (0.50 mg L^{-1}) compared to that of *E. coli* (6.78 mg L^{-1}) shows that *S. aureus* is more susceptible to AMX. After UV/H_2O_2 treatment for 4 min, AMX solution no longer inhibits the growth of *E. coli*, whereas its effect against *S. aureus* is significant. The reason may be ascribed to the extra outer membrane of Gram-negative bacteria as the diffusion barrier, which causes less vulnerability of *E. coli* towards AMX (Szabó et al., 2016a).

The significant decrease of antibacterial activity is consistent with the degradation pathway. The sulfoxides products (TP1 and TP3) can induce the beta-lactam ring-opening, leading to the antibacterial activity elimination of the solution

(Szabó et al., 2016b). The carbon centered radicals can be generated as the intermediates of the sulfoxide products, which are located adjacent to the beta-lactam ring. As a result, the electron transfer reaction may occur at the electron-deficient carbon in the four-membered ring, leading to the opening of the lactam ring. Dodd et al. (2010) also reported the antibacterial activity elimination of two beta-lactam antibiotics during $HO^{\bullet}$ oxidation. Although TP2 may retain antibacterial activity due to the intact beta-lactam ring, it can react with the radicals to form the monohydroxy AMX sulfoxide TP3 readily. A significant removal of antibacterial activity can be achieved with sufficient reaction time. As to the hydrolysis products (TP4, TP5, and TP6), the opening of their beta-lactam ring results in a decrease in the antibacterial activity (He et al., 2014). Therefore, the products of AMX possess much lower antibacterial activity after UV/H_2O_2 or UV/PS treatment, indicating that these two technologies are effective in removing AMX as well as eliminating its antibacterial activity during water treatment. The results of the antibacterial activity provide a more comprehensive understanding of the AMX degradation effect in the UV/AOP systems. Jung et al. (2012) found that the antibacterial activity of AMX treated by UV/H_2O_2 process increased at first, but then decreased after a contact time of 20 min. However, Pereira et al. (2014) found that solar photocatalytic oxidation can degrade AMX as well as eliminate its antibacterial activity completely. This can be ascribed to the various degradation pathways of AMX in different systems.

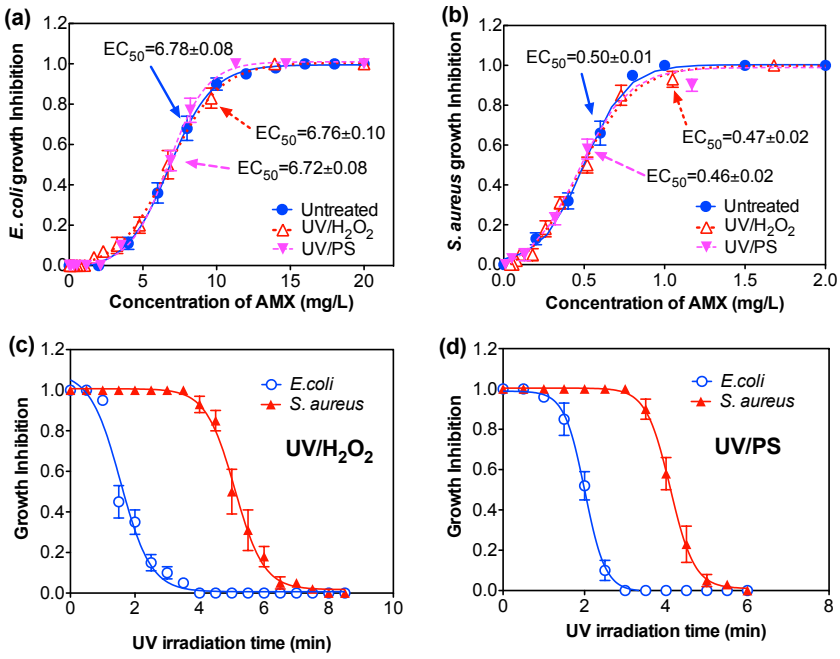

Figure 5.7 Changes in bacterial inhibition as a function of AMX concentration for (a) *E. coli* and (b) *S. aureus*; and changes in bacterial inhibition as a function of UV irradiation time under (c) UV/H_2O_2 and (d) UV/PS treatment.

5.5 Conclusion

This chapter investigated the reaction kinetics, degradation pathways and antibacterial activity of AMX in the UV/H_2O_2, and UV/PS systems. Direct UV irradiation causes insignificant photolysis of AMX, while the addition of oxidant increases the degradation efficiency of AMX significantly. $SO_4^{\bullet-}$ accounts for 69.9% of observed AMX losses in the UV/PS system, indicating a non-negligible contribution of $HO^{\bullet}$. The degradation of AMX is negatively affected with addition of HA, Cl^-, and HCO_3^- in both UV/AOP systems, while UV/PS process is less influenced by the water matrix compared with UV/H_2O_2 process. Hydroxylation (+16 Da), hydrolysis (+18 Da), and decarboxylation (-44 Da) are the main proposed AMX degradation pathways in the UV/AOP systems. The frontier electron density results indicate that $SO_4^{\bullet-}$ mainly attacks AMX at the sulfur atom on the thioether groups, while $HO^{\bullet}$ can attack AMX at both sulfur atom and benzene ring. The products of AMX after UV/AOPs treatment possess significantly lower antibacterial activity.

Chapter 6 QSPR prediction for the hydroxyl and sulfate radical oxidation of micropollutants using artificial neural networks

6.1 Introduction

The aim of this chapter is to establish QSPR models to predict the second-order rate constant of radicals ($k_{HO^{\bullet}}$ and $k_{SO_4^{\bullet-}}$) for micropollutants using artificial neural networks. Two databases were established for QSPR modeling, including an activity database and a descriptor database. 128 micropollutants were collected from the published papers and randomly divided into the training, validation, and test set. 5286 descriptors were generated from the software to develop the model. Multiple linear regression (MLR) models show low predictivity in this study. In comparison, artificial neural network (ANN) and deep neural network (DNN) models can predict the dataset accurately. Three descriptor filtration approaches were evaluated and compared, including non-dimension-reduction (NDR) approach, correlation analysis (CA) approach, and principal component analysis (PCA) approach. The most predictive models were validated using applicability domain (AD) and visualized in the Williams plot. The models developed in this study show good robustness and high reliability, indicating that ANN and DNN models can be used to evaluate the degradation of micropollutants by $HO^{\bullet}$ and $SO_4^{\bullet-}$ in water. To our knowledge, it is the first attempt to apply DNN approach in predicting the degradation efficiency of micropollutants.

6.2 QSPR modeling procedures

6.2.1 Data collection

Collecting reliable and standardized dataset is the first step to develop QSPR models. In this study, a total of 128 micropollutants were selected to establish an activity database and a descriptor database. The training (70%), validation (15%) and

test (15%) sets were used to train the model, determine when to terminate the training process, and assess the performance of the developed model, respectively (Jiang et al., 2016). The activity database, namely the second-order degradation rate constants between micropollutants and radicals ($k_{HO^{\bullet}}$ and $k_{SO_4^{\bullet-}}$), was obtained from published literatures and transformed logarithmically. The transformed $k_{HO^{\bullet}}$ and $k_{SO_4^{\bullet-}}$ values range from 2.3 $\times 10^7$ to 3.15 $\times 10^{10}$ $M^{-1}s^{-1}$ and 1.4$\times$ 10^4 to 8.12 $\times$ 10^{10} M^{-1} s^{-1}, respectively (**Appendix 13**) (Acero et al., 2018; Borhani et al., 2016; Buxton et al., 1988; Chen et al., 2015, 2018; Chu et al., 2016; Criquet and Leitner, 2015; Deshpande et al., 2004; Duan et al., 2017; Fang et al., 2018; Gao et al., 2015; Haag and David Yao, 1992; He et al., 2013; Ismail et al., 2017; Khan et al., 2017; Lian et al., 2017; Liu et al., 2015; Lu et al., 2018; Luo et al., 2019, 2016; Lutze et al., 2015; Mahdi-Ahmed and Chiron, 2014; Nihemaiti et al., 2018; Ocampo-Pérez et al., 2010; Rickman and Mezyk, 2010; Shah et al., 2013; Song et al., 2008; Toth et al., 2012; Wang et al., 2018; Xiao et al., 2016; Xie et al., 2015; Yang et al., 2017; Ye et al., 2017b; B.-T. Zhang et al., 2015; R. Zhang et al., 2015; Zhou et al., 2017b, 2017a).

The descriptor dataset, namely the numeral values that characterize properties of molecules, was calculated using computer programs. Dragon 7.0 software was used to yield a total of 5270 molecular descriptors, including constitutional, topological, geometrical descriptors, etc. Gaussian 09W was used to calculate 10 quantum-chemical descriptors, including the dipole moment (x, y, z, total), the energy of the highest occupied molecular orbital (E_{homo}), the energy of the lowest unoccupied molecular orbital (E_{lumo}), the energy gap between E_{homo} and E_{lumo} (HLG), the most negative charge on a main-chain carbon atom ($q(C)_{max}$ and $q(C)_{min}$), and the most positive partial charge on a main-chain hydrogen atom ($q(H^+)$). Material Studio 7.0 was used to calculate the other 6 quantum-chemical descriptors, namely the Fukui indices for nucleophilic, electrophilic, and $HO^{\bullet}$ attack ($f(+)_x$, $f(+)_n$, $f(-)_x$, $f(-)_n$, $f(0)_x$, and $f(0)_n$). The three-dimensional geometries of micropollutants molecular structure

was established by ChemBio Office 2014 software. Density functional theory (DFT) M06-2X/6-31++G(d,p) basis set was applied to optimize the structure of compounds and calculate the total energy of the geometry in the software. The solvent effects were taken into account using the SMD solvation model.

6.2.2 Descriptor filtration

Putting all the raw data into the modelling and optimization stage without any pre-stage processes is the easiest way to build a QSPR model. However, the descriptors with poor correlation to the activity dataset or high collinearity may give rise to the risk of model overfitting. Since some generated descriptors may exhibit poor correlation with activity or collinearity with other descriptors, it is of significance to reduce the dimension of descriptors in sophisticated computations. By selecting the appropriate and interpretable ones from the vast database, descriptor filtration can reduce the complexity in dealing with unnecessary descriptors as well as decrease the risk of over-training, which can be further divided into internal filtration approaches and external filtration approaches.

In this chapter, we compared the performances of three filtration methods, including non-dimension-reduction (NDR), correlation analysis (CA), and principal component analysis (PCA). CA was used as an external filtration method, which selected the descriptors according to the statistical relationship between the descriptor values and k values. Two sets of nine descriptors with the highest correlation coefficient to $k_{HO^{\cdot}}$ or $k_{SO_4^{\cdot-}}$ were selected as statistically effective descriptors, respectively. Their correlation matrixes are shown in **Tables 6.1 and 6.2**, indicating the low correlation of the selected descriptors. PCA, as an internal filtration, screened the descriptors based on the collinearity analysis and projects the vast dimensionality of descriptors into a low number of principal components. Nine principal components were used as a new set of input variables, which preserve 99% explanation of the total variance.

Table 6.1 Correlation matrix of selected descriptors for $k_{HO^{\bullet}}$ model.

	Me	nHM	piPC03	IC3	C-001	C-016	MLOGP	HLG	$f(-)_n$
Me[a]	1.0000								
nHM[b]	0.1943	1.0000							
piPC03[c]	-0.1753	0.2668	1.0000						
IC3[d]	-0.2185	0.2336	0.8838	1.0000					
C-001[e]	-0.4826	-0.1554	0.1387	0.1902	1.0000				
C-016[f]	-0.1717	-0.0773	0.0724	0.0808	-0.0549	1.0000			
MLOGP[g]	-0.4711	0.3491	0.4373	0.3594	0.2182	0.0546	1.0000		
HLG[h]	-0.0161	-0.0950	-0.0655	-0.0815	0.0818	0.0609	-0.0702	1.0000	
$f(-)_n$[i]	0.3495	-0.0779	-0.6238	-0.6207	-0.2634	-0.1174	-0.3279	0.0746	1.0000

[a] Me is mean atomic Sanderson electronegativity (scaled on C atom),

[b] nHM is number of heavy atoms,

[c] piPC03 is molecular multiple path count of order 3,

[d] IC3 is Information Content index (neighborhood symmetry of 3-order),

[e] C-001 is number of CH_3R/CH_4,

[f] C-016 is number of =CHR,

[g] MLOGP is Moriguchi octanol-water partition coeff. (logP),

[h] HLG is the energy gap between the homo and lumo channel,

[i] $f(-)_n$ is the minimum Fukui index for electrophilic attack,

Table 6.2 Correlation matrix of selected descriptors for $k_{SO_4^{\bullet-}}$ model.

	Se	Sp	nHM	N%	nRNHR	nRSR	MLOGP	E_{homo}	$f(-)_n$
Se[a]	1.0000								
Sp[b]	0.6142	1.0000							
nHM	0.2415	0.3769	1.0000						
N%[c]	0.1177	0.1604	0.0911	1.0000					
nRNHR[d]	0.4476	0.3613	-0.1299	-0.0916	1.0000				
nRSR[e]	0.2346	0.3238	0.2052	0.1479	-0.0698	1.0000			
MLOGP	0.3042	0.4235	0.3491	0.0364	0.1290	0.0854	1.0000		
E_{homo}[f]	0.4086	0.4200	-0.0517	0.0001	0.1191	0.1093	0.2633	1.0000	
$f(-)_n$	-0.5638	-0.5370	-0.0779	-0.1857	-0.2009	-0.1315	-0.3279	-0.2949	1.0000

[a] Se is sum of atomic Sanderson electronegativities (scaled on C atom),

[b] Sp is sum of atomic polarizabilities (scaled on C atom),

[c] N% is percentage of N atoms,

[d] nRNHR is number of secondary amines (aliphatic),

[e] nRSR is number of sulphides,

[f] E_{homo} is the acronym for energy of highest occupied molecular orbital.

6.2.3 Model optimization

In this study, MLR, ANN, and DNN were used as training algorithms to optimize the models. MLR models established linear relationship between selected descriptors and response variables (k values), which were evaluated by the coefficient of determination (R^2). ANN models were designed with three layers, namely one input layer, one hidden layer, and one output layer. The numbers of neurons for the ANN input and output layer were determined by the number of input descriptors and response variables, respectively. The optimal number of neurons in the hidden layer was determined using an exhaustive search from 1 up to 32. The correlation coefficient of overall dataset (R_{all}) was used as the main statistical indicator, while the correlation coefficient of training, test, validation ($R_{training}$, R_{test} and $R_{validation}$) were also taken into account. Same processes were applied to DNN models with two and three hidden layers (Jiang et al., 2016).

6.2.4 Model validation

The applicability domain (AD) and outliers of QSPR model were identified to evaluate the predictivity of the developed models and visualized in a Williams plot. AD refers to the theoretical region where the developed QSPR model could make reliable predictions, which can avoid the inaccurate predictions for compounds outside the domain. Williams plot is the plot of standardized cross-validated residuals versus leverage (h), which shows simple and straightforward graphical evaluation of both structurally influential chemicals and response outliers. Chemicals which fall outside the AD in a QSPR model are regarded as outliers. The leverage of a compound refers to its distance from the centroid of X, which is calculated as $h_i = x_i^T(X^TX)^{-1}x_i$, where x_i is the descriptor vector of the considered compound, X is the descriptor matrix derived from the descriptor values of the training set. The leverage threshold h^* is calculated as $h^* = 3(p+1)/n$, where p is the number of descriptors, and n is the number of the training compounds. A compound with $h > h^*$ seriously

influences the regression performance, but it is not necessarily an outlier if its standardized residual is small. Moreover, a value of 3 for a standardized residual is commonly applied as a cut-off value for accepting predictions, since points that lie ±3 standardized residual from the mean cover 99% of the normally distributed data. Outliers may be caused by the measurement error or the heavy-tailed distribution of the samples.

6.3 QSPR modeling results

6.3.1 Results of MLR model

Figure 6.1 shows the predicted $k_{HO^{\bullet}}$ and $k_{SO_4^{\bullet-}}$ models generated by MLR using (a) all the descriptors, (b) descriptors filtered by CA, and (c) descriptors extracted by PCA. The fairly low R^2 values indicate poor statistical predictions of the MLR. MLR model is built based on several assumptions, including the linear relationship between the predicted variables and the explanatory variables, as well as the low correlation between each explanatory variable. However, these mentioned assumptions may not be satisfied by the dataset in this study, leading to a failure of the model training. As a result, MLR was excluded from the stepwise model investigations and comparisons.

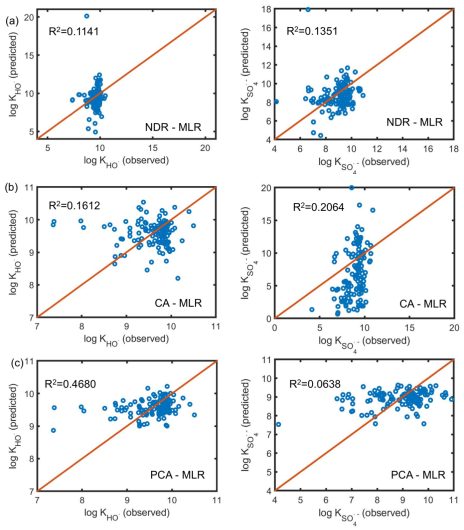

Figure 6.1 Performance of MLR models using (a) all the descriptors, (b) descriptors filtered by CA, and (c) descriptors extracted by PCA.

6.3.2 Comparison of the description filtration approaches trained by ANN

ANN models were developed using all the descriptors, descriptors filtered by CA, and descriptors extracted by PCA, respectively. R values of training, validation, test, and overall dataset were summarized in **Table 6.3**. The results of the neuron number screening and the details of the optimized model performance can be found in **Appendices 14-17** and **Figures 6.2- 6.7**.

Table 6.3 Comparison of model performance generated by ANN with various descriptor filtration approaches.

Method	$k_{HO^\bullet}$				$k_{SO_4^{\bullet-}}$			
	$R_{training}$	$R_{validation}$	R_{test}	R_{all}	$R_{training}$	$R_{validation}$	R_{test}	R_{all}
NDR-ANN	0.6531	0.6775	0.3572	0.5499	0.6199	0.8985	0.1352	0.5892
CA-ANN	0.8736	0.8552	0.9718	0.8567	0.8708	0.9251	0.8252	0.8255
PCA-ANN	0.9956	0.5734	0.4560	0.7018	0.8428	0.7955	0.3926	0.7944

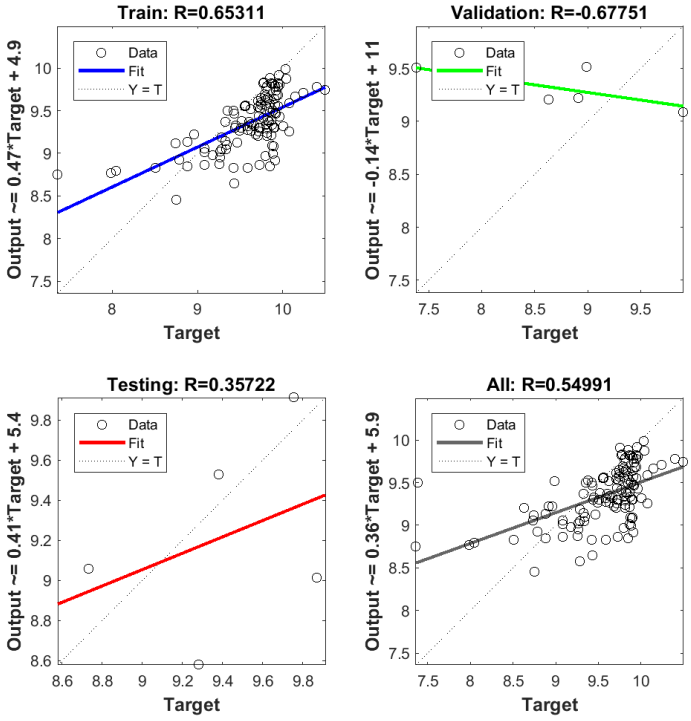

Figure 6.2 $k_{HO^\bullet}$ model generated by NDR-ANN.

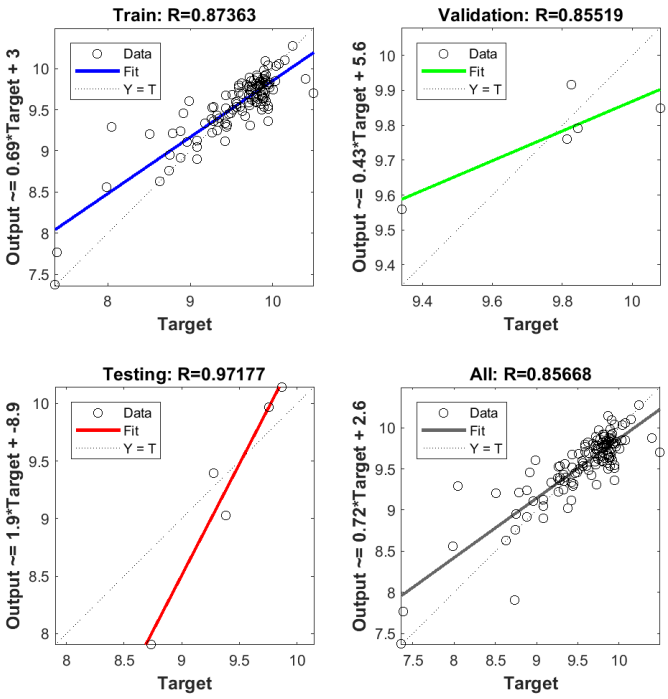

Figure 6.3 k_{HO}. model generated by CA-ANN.

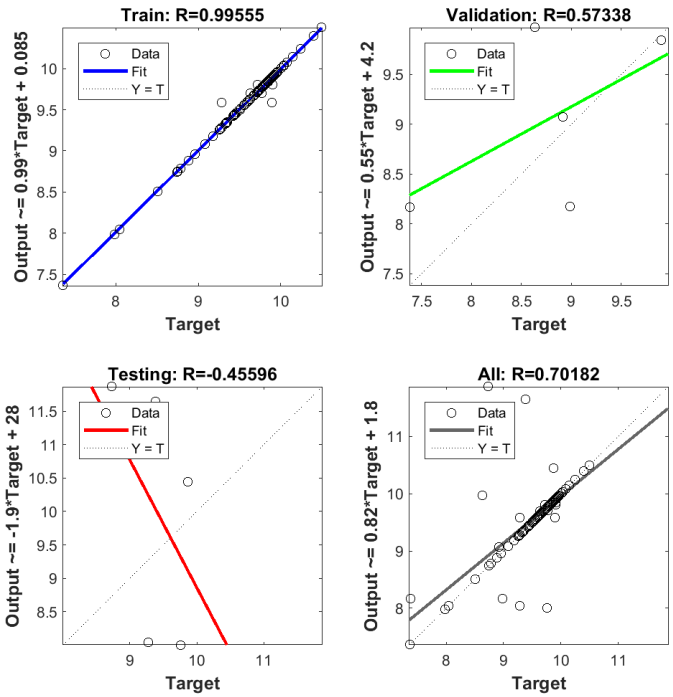

Figure 6.4 k_{HO}. model generated by PCA-ANN.

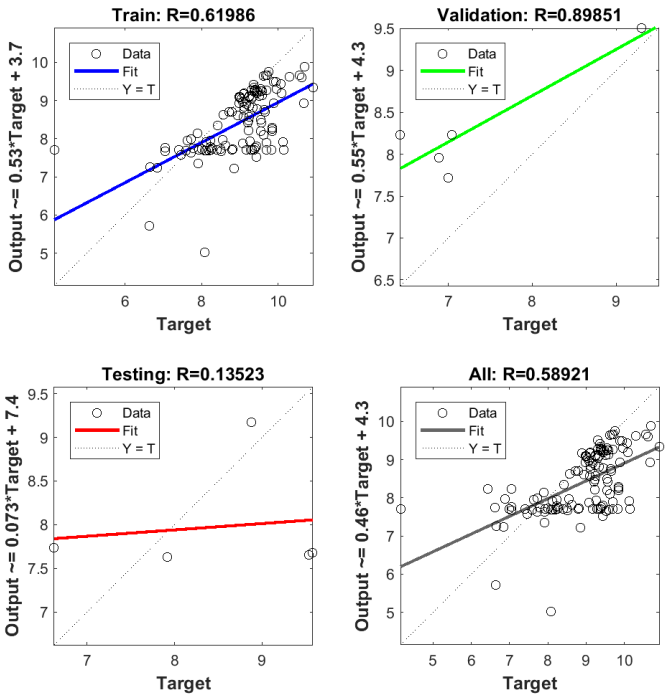

Figure 6.5 $k_{SO_4^{\bullet-}}$ model generated by NDR-ANN.

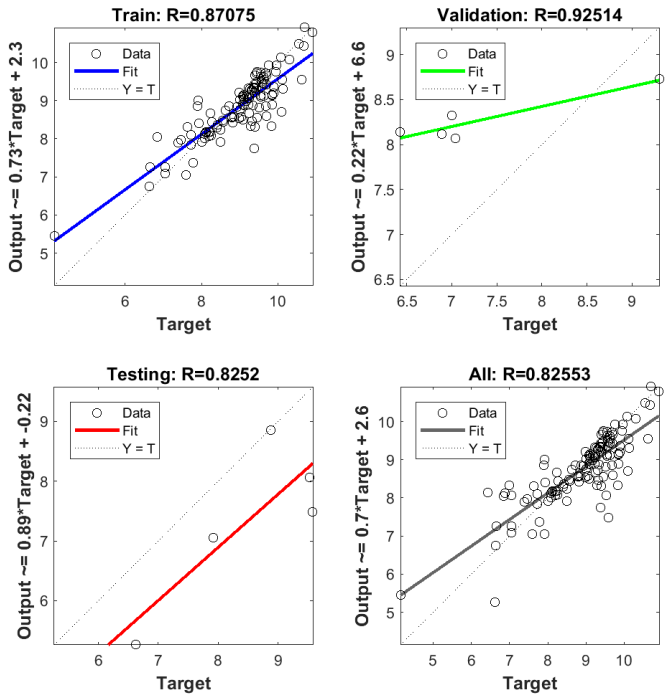

Figure 6.6 $k_{SO_4^{\bullet-}}$ model generated by CA-ANN.

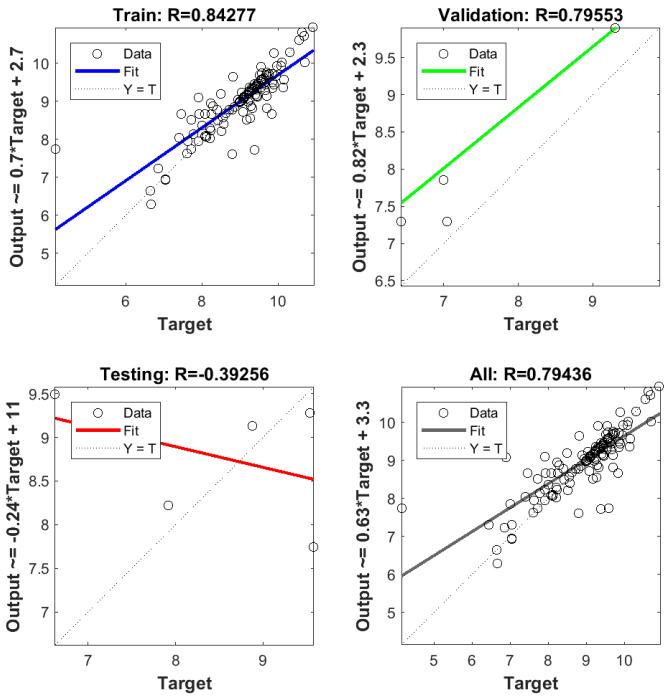

Figure 6.7 $k_{SO_4^{2-}}$ model generated by PCA-ANN.

As can be seen, the models using all the descriptors (NDR-ANN) show poor overall accuracy, with R_{all} of 0.5499 and 0.5892 for the two models, respectively. This indicates an overfitting on the training set, i.e., the insufficient robustness of the obtained model. The reason can be explained as NDR models contain the whole information in raw data to avoid any unnecessary lost, thus it's only applicable for a sufficiently small dataset with relatively good statistical properties. However, the redundant descriptors in this study may involve natural biases and uncertainties, leading to the risk of the mathematical modelling overfitting. Thus, NDR was excluded from the stepwise model investigations.

In comparison, CA-ANN and PCA-ANN models perform well for the overall dataset. CA-ANN model perform better on the overall dataset (R_{all}=0.8567 and 0.8255 for the two models) than PCA-ANN model (R_{all}=0.7018 and 0.7944 for the two models) for both models. The reason may be that CA filtration method identifies the potential collinearity between the descriptors, and removes the unnecessary

descriptors. As a result, the selected descriptors are mostly related to the target data. As to the PCA method, it extracts a new set of descriptors from the raw data, and captures most statistical characters. However, the bias from the raw data may be remained in the newly generated descriptors.

In addition, CA-ANN method exhibits a reasonable goodness-of-fit in the training set, and a stable predictability in the validation and test set. In comparison, PCA-ANN method yields a comparable or even higher statistical robustness in the training set but rather poor predictability in the validation and test set. The reason may be that the hyper-parameter of the model, such as the hidden layer number, has not reached its premium situation. As a result, CA-ANN and PCA-ANN methods with multiple hidden layers were investigated accordingly.

6.3.3 Comparison of ANN and DNN models

In this section, the developed ANN models with one hidden layer were extended to DNN models with multiple hidden layers. The training process was similar to the ANN training process by applying extremum seeking to search for the optimized structure (neuron number and hidden layer number). **Appendices 14-17** and **Figures 6.8-6.15** show detailed training, testing and validation results of the two predicted $k_{HO^\bullet}$ and $k_{SO_4^{\bullet-}}$ models generated by DNN with 2 or 3 hidden layers, using descriptors filtered by CA or PCA. The comparison of R values of various models generated by DNN is summarized in **Table 6.4**.

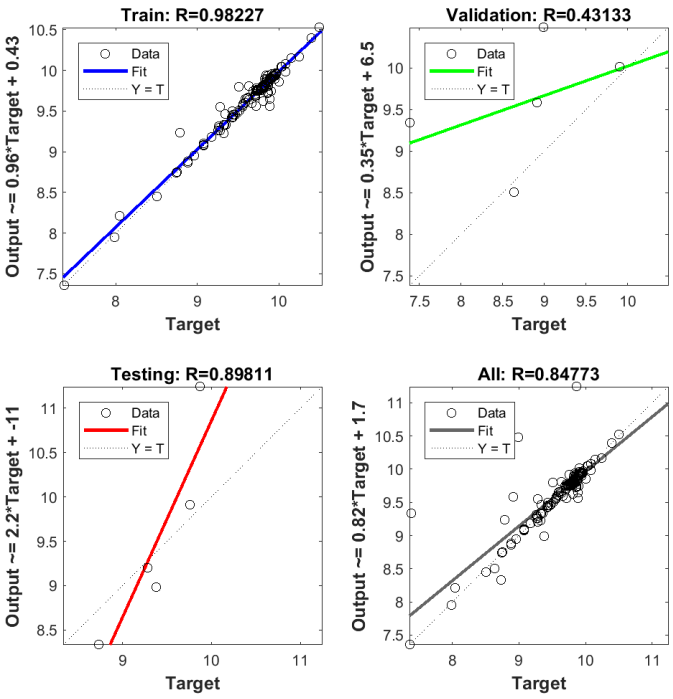

Figure 6.8 k_{HO}. model generated by CA-DNN (2 hidden layers).

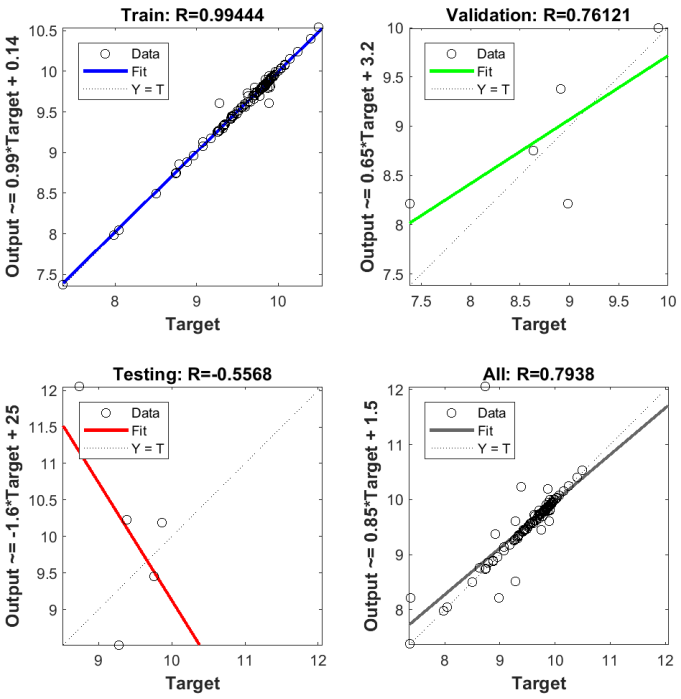

Figure 6.9 k_{HO}. model generated by PCA-DNN (2 hidden layers).

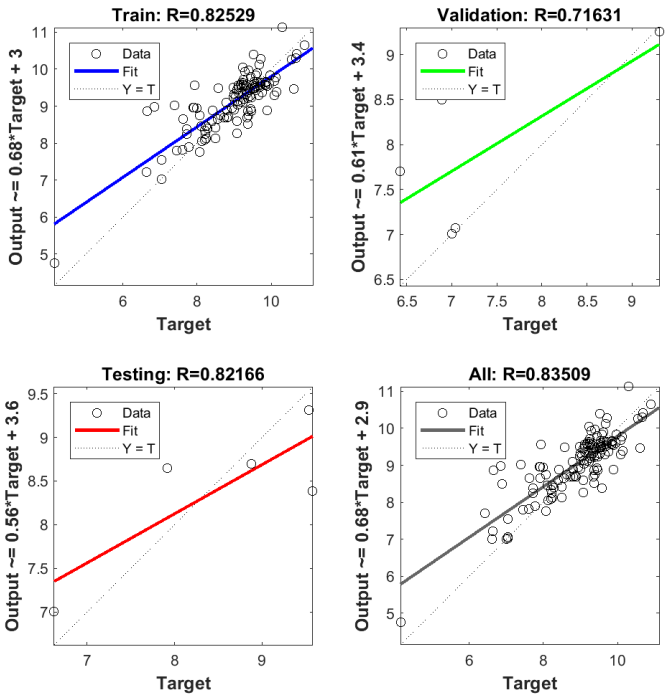

Figure 6.10 $k_{SO_4^{\cdot-}}$ model generated by CA-DNN (2 hidden layers).

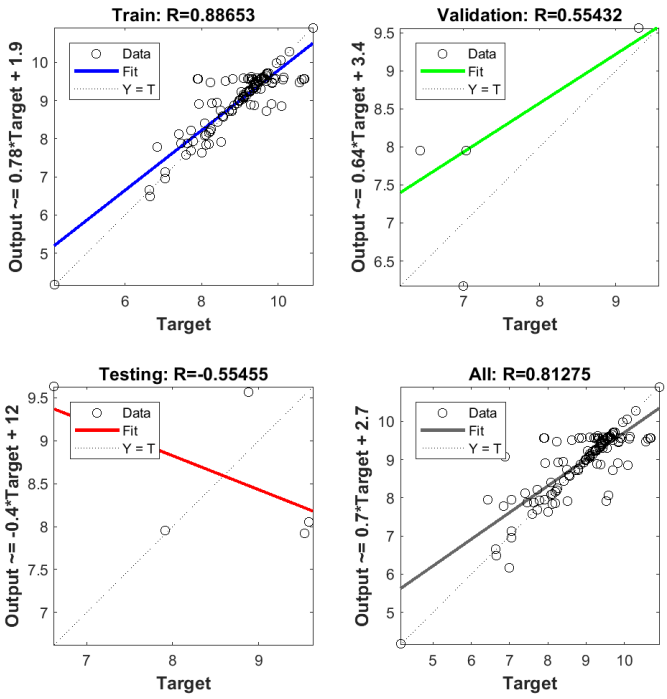

Figure 6.11 $k_{SO_4^{\cdot-}}$ model generated by PCA-DNN (2 hidden layers).

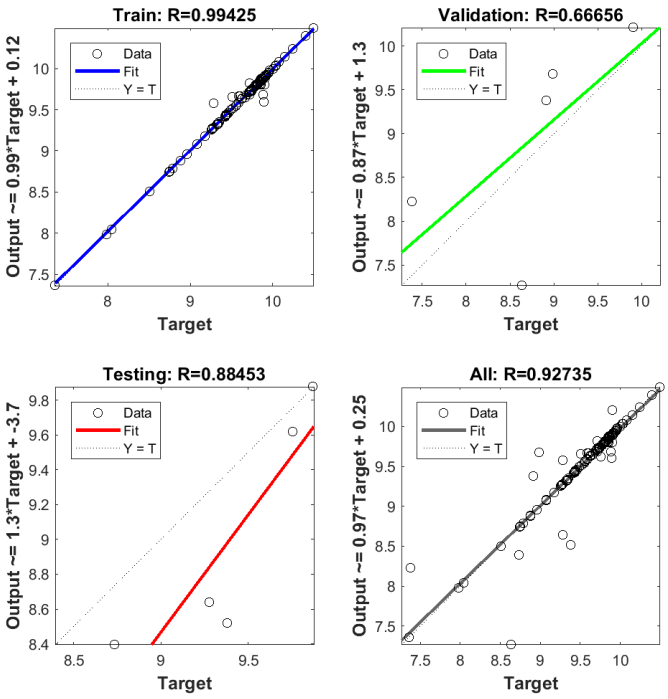

Figure 6.12 k_{HO}. model generated by CA-DNN (3 hidden layers).

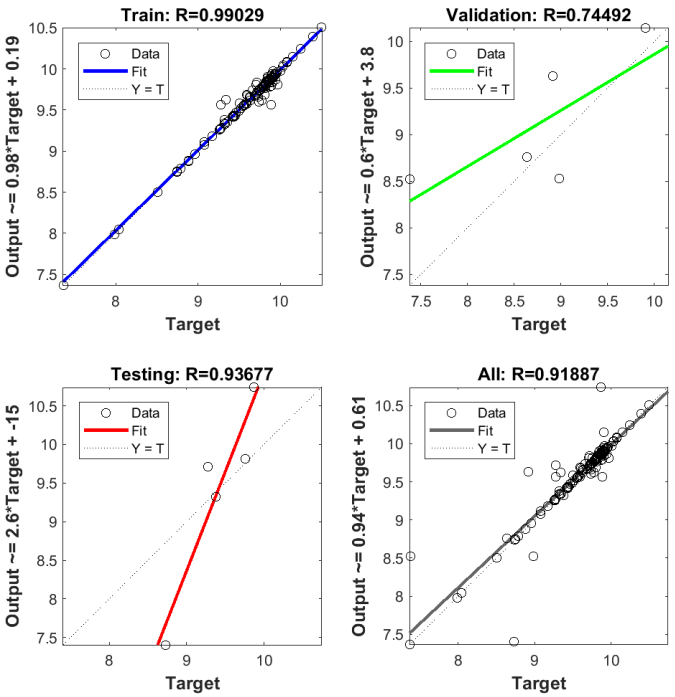

Figure 6.13 k_{HO}. model generated by PCA-DNN (3 hidden layers).

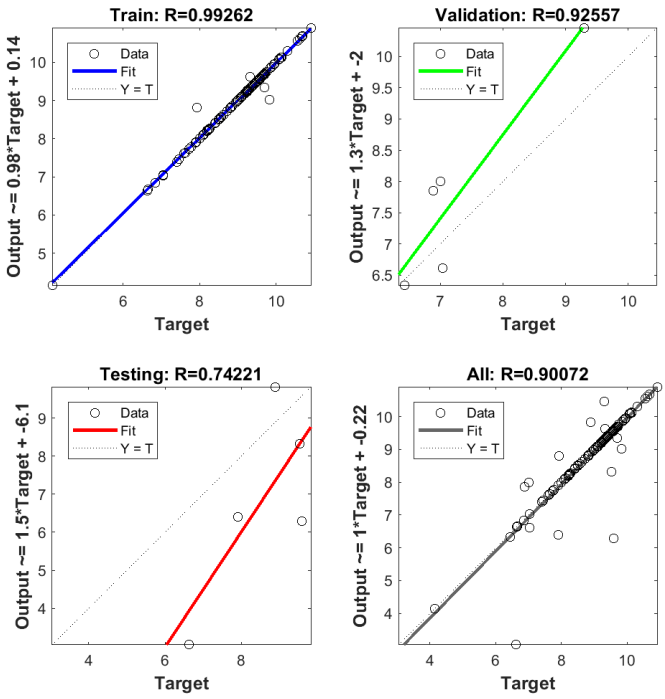

Figure 6.14 $k_{SO_4^{2-}}$ model generated by CA-DNN (3 hidden layers).

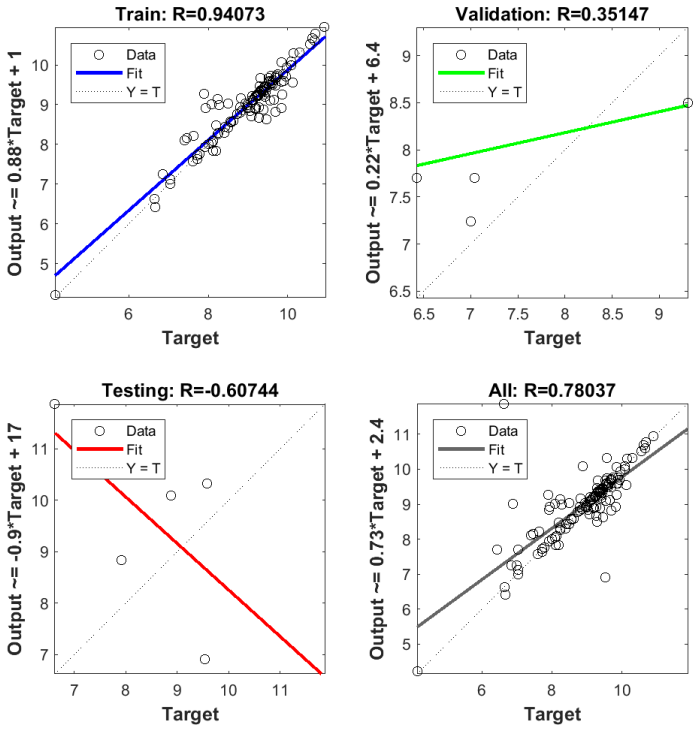

Figure 6.15 $k_{SO_4^{2-}}$ model generated by PCA-DNN (3 hidden layers).

As can be seen, the descriptors selected by CA show a better predictivity than that extracted by PCA using the modelling method with same hidden layer number. For example, for $k_{HO^{\bullet}}$ model, the R_{all} values of CA-DNN (2 hidden layers) and PCA-DNN (2 hidden layers) are 0.8477 and 0.7938, respectively; while that of CA-DNN (3 hidden layers) and PCA-DNN (3 hidden layers) are 0.9274 and 0.9189, respectively, which is consistent with the ANN results.

In addition, CA-DNN with 3 hidden layers exhibit better performance than CA-DNN with 2 hidden layers and CA-ANN for both models. This may be attributed to the additional layers can transform composition of features from input and lower hidden layers, thus exhibiting more predictive power in modelling. Since the dataset used in this study is relatively small (128 compounds and 9 selected descriptors), the difference of ANN and DNN models may become more significant when dealing with larger datasets.

Table 6.4 Comparison of model performance generated by DNN with various descriptor filtration approaches.

Method	$k_{HO^{\bullet}}$				$k_{SO_4^{\bullet-}}$			
	$R_{training}$	$R_{validation}$	R_{test}	R_{all}	$R_{training}$	$R_{validation}$	R_{test}	R_{all}
CA – DNN (2 hidden layers)	0.9823	0.4313	0.8981	0.8477	0.8253	0.7163	0.8217	0.8351
PCA – DNN (2 hidden layers)	0.9944	0.7612	0.5568	0.7938	0.8865	0.5543	0.5546	0.8128
CA – DNN (3 hidden layers)	0.9943	0.6666	0.8845	**0.9274**	0.9926	0.9256	0.7422	**0.9007**
PCA – DNN (3 hidden layers)	0.9903	0.7449	0.9368	0.9189	0.9407	0.3515	0.6074	0.7804

6.3.4 Applicability domain

Williams plots demonstrate the AD of the QSPR models, which is assessed using the standardized residuals and leverages. The $k_{HO^{\bullet}}$ and $k_{SO_4^{\bullet-}}$ models were selected based on the R value of overall dataset (**Table 6.4**), i.e., CA-DNN with 3 hidden

layers for both models. As shown in **Figure 6.16**, the horizontal dash lines are the standardized residual equal to ±3 covering 99% of normally distributed data, while the vertical dash line is set at warning leverage (h^*) value of 0.234. The AD is located in the region of $0 < h < 0.234$ and $-3 < R < 3$. The compounds located in the AD results in a valid model. The compounds with $|R| > 3$ and $h < h^*$ are referred as Y axis outlier points, which are not satisfactorily accurate. The compounds with $h > h^*$ and $-3 < R < 3$ are referred as "good high leverage" model points. The compounds with $h > h^*$ and ($R > 3$ or $R < -3$) are referred as "bad high leverage" model points.

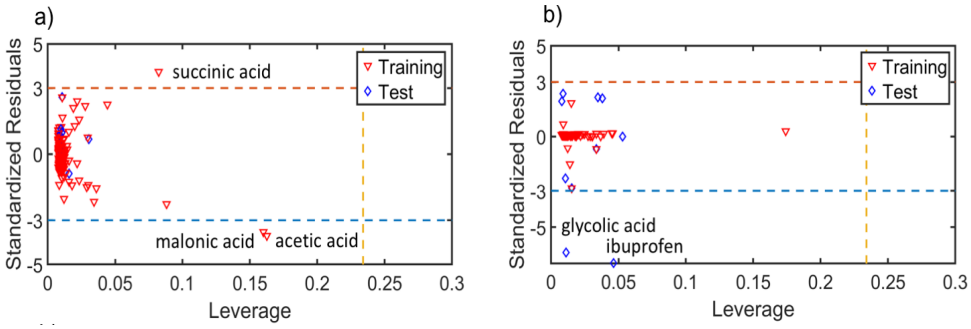

Figure 6.16 Williams plot of standardized residual and hat leverage for training set and validation set for (a) $k_{HO^\bullet}$ model and (b) $k_{SO_4^{\bullet-}}$ model using CA-DNN with 3 hidden layers.

Figure 6.16 shows the Williams plot of $k_{HO^\bullet}$ and $k_{SO_4^{\bullet-}}$ model generated by CA-DNN with 3 hidden layers. As can be seen, the leverage values of all the compounds from the training and test set are lower than the warning leverage. However, three chemicals (succinic acid, malonic acid, and acetic acid) from training set of $k_{HO^\bullet}$ model and two chemicals (glycolic acid and ibuprofen) from test set of $k_{SO_4^{\bullet-}}$ model exceed the standardized residual of 3. The reason for the outlier may be due to the selected descriptors cannot show some relevant structural feature in these chemicals, since most of the compounds that caused problem are acids. These acids can react with radicals by another mechanism (i.e., the decarboxylation of the acid group) and cause the change of the kinetics. Another reason may be due to the inaccurate experimental data obtained from the publications (Borhani et al., 2016).

With outliers identified and removed, the models developed in this study (**Figure 6.16**) show good robustness and high reliability. The leverage of chemicals based on the selected models are shown in **Appendix 17**.

6.3.5 Descriptors interpretation

In this study, the $k_{HO^{\bullet}}$ and $k_{SO_4^{\bullet-}}$ models involve two sets of 9 descriptors, as shown in **Table 6.1**. The descriptors selected for the models can give information on the mechanism of the radical reaction.

For the descriptors of $k_{HO^{\bullet}}$ model, C-001 characterizes the number of CH_3R or CH_4, which suggests the H-atom abstraction mechanism of $HO^{\bullet}$ reaction. H-atom abstraction can take place by withdrawing electrons from the C-H bond (Luo et al., 2017). C-016 refers to the number of functional group =CHR, which suggests the radical addition of reaction of $HO^{\bullet}$. $HO^{\bullet}$ can degrade the chemical by reacting with its double bond. The descriptor piPC03 refers to the molecular multiple path count of order 3, which encodes significant information on structural bonds specifications. The structural information can influence the reactivity of the radical and the reaction rate (Kusić et al., 2009). IC3 refers to the information content index (neighborhood symmetry of 3-order). It is also a structural measurement of the complexity per vertex, as determined by the pairwise equivalent atoms in an H-filled molecule (Li et al., 2018). MLogP refers to the Moriguchi octanol-water partition coefficient. It quantifies the hydrophobicity of the chemicals and influences the electrophilic reactivity of chemical reaction accordingly (Luo et al., 2017). The quantum-chemical descriptor $f(-)_n$ is the measurement of affinity for the electrophilic attack. By determining the electrophilic ability of a chemical, it is significant for the electron-transfer controlled reactions (Huang et al., 2015; Xiao et al., 2015a). The descriptor nHM refers to the number of heavy atoms. The heavy atoms (such as phosphorus, sulfur, and halogen atoms) can cause electron-donating/withdrawing effect that influence the reactivity of the radical (Li et al., 2018; Ye et al., 2017a). HLG, namely

the gap between E_{homo} and E_{lumo}, has been reported as a key indicator in radical oxidation reactions by influencing the degree of electron transfer reactions (Xiao et al., 2015a). It directly relates to the ionization potential and exhibits high correlation with the radical reactivity. Me characterizes the mean of atomic Sanderson electronegativity (scaled on C atom). Electronegativity is defined as the tendency or power of an atom to attract electrons. Molecule with high electronegativity requires extremely high energy to withdraw the electron, thus impedes with the radical-induced electron transfer (Jin et al., 2015).

For the descriptors of $k_{SO_4^{\bullet-}}$ model, N% characterizes the percentage of nitrogen in a chemical. Compounds with nitrogen atoms exhibit higher reaction rate with $SO_4^{\bullet-}$ due to the electron transfer by forming two-center three electron (2c-3c) adducts (Xiao et al., 2015a). The descriptor nRNHR characterizes the number of secondary amines (aliphatic) in a chemical. Since amine functional group is electron-rich moiety, compounds with amine groups tend to react with $SO_4^{\bullet-}$ by electron transfer pathway (Luo et al., 2018). Another functional group descriptor nRSR characterizes the number of sulfides in a chemical. Chemicals containing sulfur atoms can react with $SO_4^{\bullet-}$ by electron transfer, leading to the oxidation of S-atom to a sulfoxide or sulfone group (Ye et al., 2017a). This conclusion is consistent with the result that compounds with sulfide group exhibits a high reaction rate with $SO_4^{\bullet-}$ (Ye et al., 2017b). In addition, Sp characterizes the sum of atomic polarizabilities (scaled on C atom). The polarizability is an electronic descriptor, which is determined by both molecule size and number of valence electrons. The compound with high polarizability has a high rate constant of $SO_4^{\bullet-}$, which is confirmed by previous publications (Kusić et al., 2009). Previous researches have reported a strong relationship between polarizability and second-order rate constant for $HO^{\bullet}$ oxidation (Luo et al., 2018; Yang et al., 2016). E_{homo} is a molecular orbital descriptor that directly relates to ionization potential and exhibit high correlation with the radical reactivity. Compounds with high E_{homo} are

susceptible to be attacked by strong electrophile species to get oxidized eventually. It has also been reported as a key indicator in radical oxidation reactions by the electron transfer route. Se characterizes the sum of atomic Sanderson electronegativity (scaled on C atom), which relates to the electron-transfer mechanism, similar as the descriptor Me. Three descriptors, including MLogP, nHM, and nHM, are existed in both models, which are related to electron-transfer mechanism as mentioned.

As a result, the selected descriptors indicate the three reaction pathways for the $HO^{\bullet}$ oxidation with chemicals, namely hydrogen atom abstraction, radical addition to double bond or aromatic system, and electron transfer. In comparison, the electrophilic radical $SO_4^{\bullet-}$ tends to react with electron-rich moiety groups directly through electron-transfer mechanism. Luo et al. (2018) investigated the Gibbs free energy of the single electron transfer reactions for aromatic contaminants with $SO_4^{\bullet-}$ and $HO^{\bullet}$, indicating that $SO_4^{\bullet-}$ is more inclined to accept electrons from organic compounds and react with contaminants through single electron transfer channel.

6.4 Limitation and implication

The reliability of QSPR model is highly dependent on both quantity and quality of the data source. The quantity of the dataset used in this study is relatively small due to the limited available resource. In addition, to ensure the consistency of the dataset, the data is expected to be collected under the same experimental condition, i.e., the same lab and the same analysts. However, it is impossible to achieve due to the intensive effort needed, which may lead to the inconsistency of the data. The QSPR models in this study can be further improved by training with a larger and more reliable database from future research.

ANN and DNN models, with a large number of hidden neurons and hidden layers, are regarded as “black-box” models. Therefore, it is difficult to

straightforwardly interpret the contribution of each input descriptor (Cho et al., 2011). Besides, these methods are complicated and time-consuming to calculate compared with linear regression methods. However, due to their ability of learning the underlying non-linear relations between input and output, modelling complex input-output relationships, ANN and DNN models can generate better predictions than linear regression methods. Instead of taking the place of lab experimental measurement, QSPR models developed in this study are expected to play a more significant role in supplementing, extending, and promoting our future understanding of micropollutant issues at this stage.

6.5 Conclusions

In this chapter, QSPR models were developed for predicting the second-order rate constant between micropollutants with $HO^{\bullet}$ and $SO_4^{\bullet-}$. NDR, CA, and PCA approaches were investigated and compared as descriptor filtration methods. The descriptors selected by CA always show a better predictivity than that extracted by PCA using same modelling method. The poor accuracies of MLR models indicate that linear models are not suitable for predicting both $k_{HO^{\bullet}}$ and $k_{SO_4^{\bullet-}}$ values using data in this study. ANN and DNN models trained with the same data set are more predictive than the MLR models. CA-DNN models with additional hidden layers exhibit more predictive power in modelling than CA-ANN models. The best $k_{HO^{\bullet}}$ and $k_{SO_4^{\bullet-}}$ models with the highest predictivity and reliable application domain are CA-DNN (3 hidden layers) models. According to the selected descriptors, it can be inferred that $HO^{\bullet}$ oxidation tends to react with chemicals through hydrogen atom abstraction, radical addition, and electron transfer, while $SO_4^{\bullet-}$ is more inclined to react with contaminants through single electron transfer channel. The ANN and DNN models developed in this study can be used as a predicting tool for the degradation of the newly emerging micropollutants.

Chapter 7 Conclusions and recommendations

7.1 Overall conclusion

The major conclusion of this research can be summarized as follows:

- **Degradation efficiency** UV photolysis generally exhibits insignificant degradation effect towards most micropollutants. Six of the investigated CSDs are degraded by less than 10% using UV fluence of 400 $mJ \cdot cm^{-2}$(10-fold of the typical water disinfection fluence). The degradation rates of micropollutants increase significantly with the addition of H_2O_2 or $S_2O_8^{2-}$ under UV irradiation, due to the generation of non-selective $HO^{\bullet}$ or selective $SO_4^{\bullet-}$. The addition of 100 μM H_2O_2 or PS with UV irradiation significantly increases the AZA degradation efficiency from 0.033 to 0.365 and 0.677 min^{-1}, respectively. For CSDs with electron-donating groups, the degradation rate constants obtained in the UV/PS system are much higher than that in the UV/H_2O_2 system, such as AZA, CYT, DOX and MET. However, the degradation rate constant of CP obtained in the UV/PS system is lower than that in the UV/H_2O_2 system, since $SO_4^{\bullet-}$ reacts selectively via electron transfer. The degradation effect of CSDs increases linearly with the increasing oxidant dose at low level, while the excess H_2O_2 can act as radical scavengers.
- **Effect of water matrix** NOM shows negative effect on direct UV photodegradation, while the addition of NO_3^- increases the photodegradation effect of chemicals by generating $HO^{\bullet}$. The degradation efficiency of micropollutants is significantly affected by the pH, NOM, HCO_3^-, and Cl^- in both UV/AOP systems. Compared with UV/H_2O_2, UV/PS is less affected by the common water matrix species in the natural water.

- **Degradation mechanism** Direct UV photolysis can remove the chemicals in water through the cleavage of their aromatic ring, while NO_3^--induced and DOM-induced photolysis are through radical addition reaction and electron transfer reaction, respectively. As to UV/AOP systems, $HO^{\bullet}$ attacks various organic compounds mainly through electron transfer, hydrogen abstraction or electrophilic addition reactions, while $SO_4^{\bullet-}$ selectively attacks certain functional groups of chemicals by electron transfer.
- **Toxicity analysis** The products of AMX after UV/AOP treatment do not retain any significant ability to inhibit the growth of *E. coli* or *S. aureus.* The removal of antibacterial activity is consistent with the degradation pathway. This indicates that both UV/H_2O_2 and UV/PS processes are effective in removing AMX as well as eliminating its antibacterial activity during water treatment.
- **Economic analysis** The economic costs of both UV/AOPs decrease significantly with the increasing oxidant concentration at low level. UV/PS process is more cost-effective for AZA degradation compared with UV/H_2O_2 process due to the high cost of H_2O_2.
- **QSPR modelling** MLR models show low predictivity to model data with nonlinearity, while ANN and DNN models trained with the same data set are more predictive and can be used to evaluate the degradation effect of micropollutants by $HO^{\bullet}$ and $SO_4^{\bullet-}$ in water. The descriptors selected by CA always show better predictivity than that extracted by PCA using same modelling method. The prediction performance of the both models follow the sequence of DNN models with 3 hidden layers > DNN models with 2 hidden layers > ANN models with 1 hidden layer, although the discrepancy between the three methods are insignificant.

7.2 Recommendation for future work

7.2.1 Investigation of various UV-AOPs

The photodegradation of micropollutants has been investigated using direct and indirect UV photolysis in this study. Photodegradation of micropollutants with various innovative UV-based AOPs is recommended to be further investigated and compared, such as UV/PMS, UV/chlorine, UV/O_3, and UV/TiO_2. The second-order rate constant of various radicals with micropollutants can also be estimated.

7.2.2 Toxicity test of the photodegradation intermediates

Various intermediates may be generated along with the micropollutant photodegradation and mineralization, leading to a possibility of higher toxicity of the solution. As a result, a systematic toxicity screening test is of great significance for evaluating the water treatment in real application, including the acute toxicity test (using *Vibrio fischeri*), ecotoxicity test (using algae, crustacean cladoceran, bacteria), genotoxicity test (using bacterial reverse mutation assay), phototoxicity test (using Balb/c 3T3 mouse fibroblasts), chronic toxicity test (using Daphnia, Fathead minnow, Green algae, Amphipod), etc.

7.2.3 Further study on QSPR model

Instead of taking the place of lab experimental measurement, QSPR models developed in this study are expected to play significant roles in supplementing, extending, and promoting our future understanding of micropollutant issues at this stage. The QSPR models developed in this study can be further improved by training with a larger and more reliable database from future research, since the reliability of QSPR models is highly dependent on both quantity and quality of the data source.

Firstly, the quantity of the dataset used in this study is relatively small due to the limited available resource. The amount of micropollutants tested in this study is also insufficient. A wider range of micropollutants, with different physical and chemical properties, can be considered in the future work.

Secondly, the quality of the dataset used in this study can be further improved. Since the second-order rate constant of chemicals reacting with oxidants were collected from various references, the different experimental condition may lead to the inconsistency of the data. Future efforts can be made to determine the data under the same experimental condition to ensure the consistency of the dataset.

REFERENCES

Acero, J.L., Benítez, F.J., Real, F.J., Rodríguez, E., 2018. Degradation of selected emerging contaminants by UV-activated persulfate: Kinetics and influence of matrix constituents. Sep. Purif. Technol. 201, 41–50. https://doi.org/10.1016/j.seppur.2018.02.055

Acero, J.L., Benitez, F.J., Real, F.J., Roldan, G., 2010. Kinetics of aqueous chlorination of some pharmaceuticals and their elimination from water matrices. Water Res. 44, 4158–4170. https://doi.org/10.1016/j.watres.2010.05.012

An, T., An, J., Gao, Y., Li, G., Fang, H., Song, W., 2015. Photocatalytic degradation and mineralization mechanism and toxicity assessment of antivirus drug acyclovir : Experimental and theoretical studies. Appl. Catal. B, Environ. 164, 279–287. https://doi.org/10.1016/j.apcatb.2014.09.009

Andreozzi, R., Canterino, M., Marotta, R., Paxeus, N., 2005. Antibiotic removal from wastewaters: The ozonation of amoxicillin. J. Hazard. Mater. 122, 243–250. https://doi.org/10.1016/j.jhazmat.2005.03.004

Andreozzi, R., Caprio, V., Ciniglia, C., De Champdoré, M., Lo Giudice, R., Marotta, R., Zuccato, E., 2004. Antibiotics in the environment: Occurrence in Italian STPs, fate, and preliminary assessment on algal toxicity of amoxicillin. Environ. Sci. Technol. 38, 6832–6838. https://doi.org/10.1021/es049509a

Antoniou, M.G., de la Cruz, A.A., Dionysiou, D.D., 2010. Degradation of microcystin-LR using sulfate radicals generated through photolysis, thermolysis and e^- transfer mechanisms. Appl. Catal. B Environ. 96, 290–298. https://doi.org/10.1016/j.apcatb.2010.02.013

Autin, O., Hart, J., Jarvis, P., MacAdam, J., Parsons, S.A., Jefferson, B., 2013. The impact of background organic matter and alkalinity on the degradation of the pesticide metaldehyde by two advanced oxidation processes: UV/H_2O_2 and

UV/TiO_2. Water Res. 47, 2041–2049. https://doi.org/10.1016/j.watres.2013.01.022

Baxendale, J.H., Wilson, J. a., 1957. The photolysis of hydrogen peroxide at high light intensities. Trans. Faraday Soc. 53, 344–356. https://doi.org/10.1039/tf9575300344

Benitez, F.J., Acero, J.L., Real, F.J., Roldan, G., Casas, F., 2011. Chemosphere Bromination of selected pharmaceuticals in water matrices. Chemosphere 85, 1430–1437. https://doi.org/10.1016/j.chemosphere.2011.08.022

Besse, J., Latour, J., Garric, J., 2012. What can we say about the occurrence and environmental significance of cytotoxic, cytostatic and endocrine therapy drugs? Environ. Int. 39, 73–86. https://doi.org/10.1016/j.envint.2011.10.002

Bolton, J.R., Stefan, M.I., 2002. Fundamental photochemical approach to the concepts of fluence (UV dose) and electrical energy efficiency in photochemical degradation reactions. Res. Chem. Intermed. 28, 857–870. https://doi.org/10.1163/15685670260469474

Booker, V., Halsall, C., Llewellyn, N., Johnson, A., Williams, R., 2014. Prioritising anticancer drugs for environmental monitoring and risk assessment purposes. Sci. Total Environ. 473–474, 159–170. https://doi.org/10.1016/j.scitotenv.2013.11.145

Borhani, T.N.G., Saniedanesh, M., Bagheri, M., 2016. QSPR prediction of the hydroxyl radical rate constant of water contaminants. Water Res. 98, 344–353. https://doi.org/10.1016/j.watres.2016.04.038

Buerge, I.J., Buser, H., Poiger, T., Müller, M.D., 2006. Occurrence and fate of the cytostatic drugs cyclophosphamide and ifosfamide in wastewater and surface waters. Environ. Sci. Technol. 40, 7242–7250. https://doi.org/10.1021/es0609405

Busetti, F., Linge, K.L., Heitz, A., 2009. Analysis of pharmaceuticals in indirect

potable reuse systems using solid-phase extraction and liquid chromatography-tandem mass spectrometry. J. Phys. Chem. A 1216, 5807–5818. https://doi.org/10.1016/j.chroma.2009.06.001

Buxton, G. V, Greenstock, C.L., Helman, W.P., Ross, A.B., 1988. Critical review of rate constants for reactions of hydrated electrons, hydrogen atoms and hydroxyl radicals (OH/O^{-}) in aqueous solution. At. Energy 17, 513–886. https://doi.org/10.1063/1.555805

Calamari, D., Zuccato, E., Castiglioni, S., 2003. Strategic survey of therapeutic drugs in the rivers Po and Lambro in northern Italy. Environ. Sci. Technol. 37, 1241–1248. https://doi.org/10.1021/es020158e

Chen, B., Zhang, T., Bond, T., Gan, Y., 2015. Development of quantitative structure activity relationship (QSAR) model for disinfection byproduct (DBP) research : A review of methods and resources. J. Hazard. Mater. 299, 260–279. https://doi.org/10.1016/j.jhazmat.2015.06.054

Chen, L., Cai, T., Cheng, C., Xiong, Z., Ding, D., 2018. Degradation of acetamiprid in UV/$H_2O_2$and UV/persulfate systems: A comparative study. Chem. Eng. J. 351, 1137–1146. https://doi.org/10.1016/j.cej.2018.06.107

Chen, Y., Hu, C., Hu, X., Qu, J., 2009. Indirect photodegradation of amine drugs in aqueous solution under simulated sunlight. Environ. Sci. Technol. 43, 2760–2765. https://doi.org/10.1021/es803325j

Cho, K.H., Sthiannopkao, S., Pachepsky, Y.A., Kim, K.W., Kim, J.H., 2011. Prediction of contamination potential of groundwater arsenic in Cambodia, Laos, and Thailand using artificial neural network. Water Res. 45, 5535–5544. https://doi.org/10.1016/j.watres.2011.08.010

Chu, W., Li, D., Deng, Y., Gao, N., Zhang, Y., Zhu, Y., 2016. Effects of UV/PS and UV/H_2O_2 pre-oxidations on the formation of trihalomethanes and haloacetonitriles during chlorination and chloramination of free amino acids

and short oligopeptides. Chem. Eng. J. 301, 65–72. https://doi.org/10.1016/j.cej.2016.04.003

Clifton, C.L., Huie, R.E., 1989. Rate constants for hydrogen abstraction reactions of the sulfate radical, $SO_4^{\bullet-}$. Alcohols. Int. J. Chem. Kinet. 21, 677–687. https://doi.org/10.1002/kin.550210807

Criquet, J., Leitner, N.K.V., 2015. Reaction pathway of the degradation of the p-hydroxybenzoic acid by sulfate radical generated by ionizing radiations. Radiat. Phys. Chem. 106, 307–314. https://doi.org/10.1016/j.radphyschem.2014.07.016

Dail, M.K., Mezyk, S.P., 2010. Hydroxyl-radical-induced degradative oxidation of β-lactam antibiotics in water: Absolute rate constant measurements. J. Phys. Chem. A 114, 8391–8395. https://doi.org/10.1021/jp104509t

De la Cruz, N., Giménez, J., Esplugas, S., Grandjean, D., de Alencastro, L.F., Pulgarín, C., 2012. Degradation of 32 emergent contaminants by UV and neutral photo-fenton in domestic wastewater effluent previously treated by activated sludge. Water Res. 46, 1947–1957. https://doi.org/10.1016/j.watres.2012.01.014

Deshpande, A.D., Baheti, K.G., Chatterjee, N.R., 2004. Degradation of beta-lactam antibiotics. Curr. Sci. 87, 1684–1695.

Dimitrakopoulou, D., Rethemiotaki, I., Frontistis, Z., Xekoukoulotakis, N.P., Venieri, D., Mantzavinos, D., 2012. Degradation, mineralization and antibiotic inactivation of amoxicillin by UV-A/TiO_2 photocatalysis. J. Environ. Manage. 98, 168–174. https://doi.org/10.1016/j.jenvman.2012.01.010

Dodd, M.C., Rentsch, D., Singer, H.P., Kohler, H.P.E., Gunten, U. Von, 2010. Transformation of β-Lactam antibacterial agents during aqueous ozonation: Reaction pathways and quantitative bioassay of biologically-active oxidation products. Environ. Sci. Technol. 44, 5940–5948.

https://doi.org/10.1021/es101061w

Duan, X., He, X., Wang, D., Mezyk, S.P., Otto, S.C., Marfil-Vega, R., Mills, M.A., Dionysiou, D.D., 2017. Decomposition of iodinated pharmaceuticals by UV-254 nm-assisted advanced oxidation processes. J. Hazard. Mater. 323, 489–499. https://doi.org/10.1016/j.jhazmat.2016.04.022

Elovitz, M.S., von Gunten, U., Kaiser, H.-P., 2000. Hydroxyl radical/ozone ratios during ozonation processes. II. The effect of temperature, pH, alkalinity, and DOM properties. Ozone Sci. Eng. 22, 123–150. https://doi.org/10.1080/01919510008547216

Fang, Z., Chelme-Ayala, P., Shi, Q., Xu, C., Gamal El-Din, M., 2018. Degradation of naphthenic acid model compounds in aqueous solution by UV activated persulfate: Influencing factors, kinetics and reaction mechanisms. Chemosphere 211, 271–277. https://doi.org/10.1016/j.chemosphere.2018.07.132

Fazio, T.T., Singh, A.K., Kedor-Hackmann, E.R.M., Santoro, M.I.R.M., 2007. Quantitative determination and sampling of azathioprine residues for cleaning validation in production area. J. Pharm. Biomed. Anal. 43, 1495–1498. https://doi.org/10.1016/j.jpba.2006.10.016

Ferrando-Climent, L., Rodriguez-Mozaz, S., Barcelo, D., 2013. Development of a UPLC-MS / MS method for the determination of ten anticancer drugs in hospital and urban wastewaters , and its application for the screening of human metabolites assisted by information-dependent acquisition tool (IDA) in sewage samples. Anal. Bioanal. Chem. 405, 5937–5952. https://doi.org/10.1007/s00216-013-6794-4

Franquet-Griell, H., Gómez-Canela, C., Ventura, F., Lacorte, S., 2015. Predicting concentrations of cytostatic drugs in sewage effluents and surface waters of Catalonia (NE Spain). Environ. Res. 138, 161–172.

https://doi.org/10.1016/j.envres.2015.02.015

Gao, Y., Gao, N., Deng, Y., Yin, D., Zhang, Y., 2015. Degradation of florfenicol in water by UV/$Na_2S_2O_8$ process. Environ. Sci. Pollut. Res. 22, 8693–8701. https://doi.org/10.1007/s11356-014-4054-6

Garcia-Ac, A., Broséus, R., Vincent, S., Barbeau, B., Prévost, M., Sauvé, S., 2010. Oxidation kinetics of cyclophosphamide and methotrexate by ozone in drinking water. Chemosphere 79, 1056–1063. https://doi.org/10.1016/j.chemosphere.2010.03.032

Göğer, N.G., Parlatan, H.K., Basan, H., Berkkan, A., Özden, T., 1999. Quantitative determination of azathioprine in tablets by 1H NMR spectroscopy. J. Pharm. Biomed. Anal. 21, 685–689. https://doi.org/10.1016/S0731-7085(99)00156-9

Gómez-Canela, C., Cortés-Francisco, N., Oliva, X., Pujol, C., Ventura, F., Lacorte, S., Caixach, J., 2012. Occurrence of cyclophosphamide and epirubicin in wastewaters by direct injection analysis-liquid chromatography-high-resolution mass spectrometry. Environ. Sci. Pollut. Res. 19, 3210–3218. https://doi.org/10.1007/s11356-012-0826-z

Haag, W.R., David Yao, C.C., 1992. Rate constants for reaction of hydroxyl radicals with several drinking water contaminants. Environ. Sci. Technol. 26, 1005–1013. https://doi.org/10.1021/es00029a021

He, X., de la Cruz, A.A., Dionysiou, D.D., 2013. Destruction of cyanobacterial toxin cylindrospermopsin by hydroxyl radicals and sulfate radicals using UV-254nm activation of hydrogen peroxide, persulfate and peroxymonosulfate. J. Photochem. Photobiol. A Chem. 251, 160–166. https://doi.org/10.1016/j.jphotochem.2012.09.017

He, X., Mezyk, S.P., Michael, I., Fatta-Kassinos, D., Dionysiou, D.D., 2014. Degradation kinetics and mechanism of β-lactam antibiotics by the activation of H_2O_2 and $Na_2S_2O_8$ under UV-254nm irradiation. J. Hazard. Mater. 279,

375–383. https://doi.org/10.1016/j.jhazmat.2014.07.008

Hirose, J., Kondo, F., Nakano, T., Kobayashi, T., 2005. Inactivation of antineoplastics in clinical wastewater by electrolysis. Chemospherem 60, 1018–1024. https://doi.org/10.1016/j.chemosphere.2005.01.024

Hirte, K., Seiwert, B., Schüürmann, G., Reemtsma, T., 2016. New hydrolysis products of the beta-lactam antibiotic amoxicillin, their pH-dependent formation and search in municipal wastewater. Water Res. 88, 880–888. https://doi.org/10.1016/j.watres.2015.11.028

Huang, X., Feng, Y., Hu, C., Xiao, X., Yu, D., Zou, X., 2015. Mechanistic QSAR models for interpreting degradation rates of sulfonamides in UV-photocatalysis systems. Chemosphere 138, 183–189. https://doi.org/10.1016/j.chemosphere.2015.05.075

Ismail, L., Ferronato, C., Fine, L., Jaber, F., Chovelon, J.M., 2017. Elimination of sulfaclozine from water with $SO_4^{\bullet-}$ radicals: Evaluation of different persulfate activation methods. Appl. Catal. B Environ. 201, 573–581. https://doi.org/10.1016/j.apcatb.2016.08.046

Jiang, G., Keller, J., Bond, P.L., Yuan, Z., 2016. Predicting concrete corrosion of sewers using artificial neural network. Water Res. 92, 52–60. https://doi.org/10.1016/j.watres.2016.01.029

Jin, X., Peldszus, S., Huck, P.M., 2015. Predicting the reaction rate constants of micropollutants with hydroxyl radicals in water using QSPR modeling. Chemosphere 138, 1–9. https://doi.org/10.1016/j.chemosphere.2015.05.034

Jo, C.H., Dietrich, A.M., Tanko, J.M., 2011. Simultaneous degradation of disinfection byproducts and earthy-musty odorants by the UV/H_2O_2 advanced oxidation process. Water Res. 45, 2507–2516. https://doi.org/10.1016/j.watres.2011.02.006

Jung, Y., Gi, W., Yoon, Y., Kang, J., Min, Y., Wook, H., 2012. Removal of

amoxicillin by UV and UV/H_2O_2 processes. Sci. Total Environ. 420, 160–167. https://doi.org/10.1016/j.scitotenv.2011.12.011

Karlesa, A., De Vera, G.A.D., Dodd, M.C., Park, J., Espino, M.P.B., Lee, Y., 2014. Ferrate(VI) oxidation of beta-lactam antibiotics: Reaction kinetics, antibacterial activity changes, and transformation products. Environ. Sci. Technol. 48, 10380–10389. https://doi.org/10.1021/es5028426

Kasiri, M.B., Khataee, A.R., 2012. Removal of organic dyes by UV/H_2O_2 process: modelling and optimization. Environ. Technol. 33, 1417–1425. https://doi.org/10.1080/09593330.2011.630425

Khan, J.A., He, X., Shah, N.S., Khan, H.M., Hapeshi, E., Fatta-Kassinos, D., Dionysiou, D.D., 2014. Kinetic and mechanism investigation on the photochemical degradation of atrazine with activated H_2O_2, $S_2O_8^{2-}$ and HSO_5^-. Chem. Eng. J. 252, 393–403. https://doi.org/10.1016/j.cej.2014.04.104

Khan, S., He, X., Khan, J.A., Khan, H.M., Boccelli, D.L., Dionysiou, D.D., 2017. Kinetics and mechanism of sulfate radical- and hydroxyl radical-induced degradation of highly chlorinated pesticide lindane in UV/peroxymonosulfate system. Chem. Eng. J. 318, 135–142. https://doi.org/10.1016/j.cej.2016.05.150

Kim, C., Ryu, H.D., Chung, E.G., Kim, Y., 2018. Determination of 18 veterinary antibiotics in environmental water using high-performance liquid chromatography-q-orbitrap combined with on-line solid-phase extraction. J. Chromatogr. B. 1084, 158–165. https://doi.org/10.1016/j.jchromb.2018.03.038

Kim, I., Tanaka, H., 2009. Photodegradation characteristics of PPCPs in water with UV treatment. Environ. Int. 35, 793–802. https://doi.org/10.1016/j.envint.2009.01.003

Kıdak, R., Şifa, D., 2018. Medium-high frequency ultrasound and ozone based advanced oxidation for amoxicillin removal in water. Ultrason. Sonochem. 40, 131–139. https://doi.org/10.1016/j.ultsonch.2017.01.033

Kosjek, T., Heath, E., 2011. Occurrence, fate and determination of cytostatic pharmaceuticals in the environment. TrAC Trends Anal. Chem. 30, 1065–1087. https://doi.org/10.1016/j.trac.2011.04.007

Kovalova, L., McArdell, C.S., Hollender, J., 2009. Challenge of high polarity and low concentrations in analysis of cytostatics and metabolites in wastewater by hydrophilic interaction chromatography/tandem mass spectrometry. J. Chromatogr. A 1216, 1100–1108. https://doi.org/10.1016/j.chroma.2008.12.028

Kovalova, L., Siegrist, H., Singer, H., Wittmer, A., Mcardell, C.S., 2012. Hospital wastewater treatment by membrane bioreactor: Performance and efficiency for organic micropollutant elimination. Environ. Sci. Technol. 46, 1536–1545. https://doi.org/10.1021/es203495d

Kümmerer, K., Al-Ahmad, A., 2010. Estimation of the cancer risk to humans resulting from the presence of cyclophosphamide and ifosfamide in surface water. Environ. Sci. Pollut. Res. 17, 486–496. https://doi.org/10.1007/s11356-009-0195-4

Kusić, H., Rasulev, B., Leszczynska, D., Leszczynski, J., Koprivanac, N., 2009. Prediction of rate constants for radical degradation of aromatic pollutants in water matrix: a QSAR study. Chemosphere 75, 1128–1134. https://doi.org/10.1016/j.chemosphere.2009.01.019

Lakshmi, C.S.., Reddy, M.N., 1998. Spectrophotometric determination of azathioprine in pharmaceutical formulations. Talanta 47, 1279–1286. https://doi.org/10.1016/S0039-9140(98)00216-1

Lee, Y., Gunten, U. Von, 2010. Oxidative transformation of micropollutants during municipal wastewater treatment : Comparison of kinetic aspects of selective (chlorine , chlorine dioxide , ferrate VI , and ozone) and non-selective oxidants (hydroxyl radical). Water Res. 44, 555–566.

https://doi.org/10.1016/j.watres.2009.11.045

Li, C., Wei, G., Chen, J., Zhao, Y., Zhang, Y.-N., Su, L., Qin, W., 2018. Aqueous OH radical reaction rate constants for organophosphorus flame retardants and plasticizers: Experimental and modeling studies. Environ. Sci. Technol. 52, 2790–2799. https://doi.org/10.1021/acs.est.7b05429

Li, W., Tanumihardja, J., Masuyama, T., Korshin, G., 2015. Examination of the kinetics of degradation of the antineoplastic drug 5-fluorouracil by chlorine and bromine. J. Hazard. Mater. 282, 125–132. https://doi.org/10.1016/j.jhazmat.2014.05.090

Lian, L., Yao, B., Hou, S., Fang, J., Yan, S., Song, W., 2017. Kinetic study of hydroxyl and sulfate radical-mediated oxidation of pharmaceuticals in wastewater effluents. Environ. Sci. Technol. 51, 2954–2962. https://doi.org/10.1021/acs.est.6b05536

Lin, A.Y.-C., Wang, X.-H., Lee, W.-N., 2013. Phototransformation determines the fate of 5-fluorouracil and cyclophosphamide in natural surface waters. Environ. Sci. Technol. 47, 4104–4112. https://doi.org/10.1021/es304976q

Lin, H.H.-H., Lin, A.Y.-C., 2014. Photocatalytic oxidation of 5-fluorouracil and cyclophosphamide via UV/TiO_2 in an aqueous environment. Water Res. 48, 559–568. https://doi.org/10.1016/j.watres.2013.10.011

Liu, Y., He, X., Fu, Y., Dionysiou, D.D., 2015. Degradation kinetics and mechanism of oxytetracycline by hydroxyl radical-based advanced oxidation processes. Chem. Eng. J. 284, 1317–1327. https://doi.org/10.1016/j.cej.2015.09.034

Llewellyn, N., Lloyd, P., Jürgens, M.D., Johnson, A.C., 2011. Determination of cyclophosphamide and ifosfamide in sewage effluent by stable isotope-dilution liquid chromatography–tandem mass spectrometry. J. Chromatogr. A 1218, 8519–8528. https://doi.org/10.1016/j.chroma.2011.09.061

Løgager, T., Sehested, K., Holcman, J., 1993. Rate constants of the equilibrium reactions $SO_4^{\bullet-} + HNO_3 \rightleftarrows HSO_4^- + NO_3^\bullet$ and $SO_4^{\bullet-} + NO_3^- \rightleftarrows SO_4^{2-} + NO_3^\bullet$. Radial. Phys. Chem. 41, 0–4.

Lu, X., Shao, Y., Gao, N., Chen, J., Deng, H., Chu, W., An, N., Peng, F., 2018. Investigation of clofibric acid removal by UV/persulfate and UV/chlorine processes: Kinetics and formation of disinfection byproducts during subsequent chlor(am)ination. Chem. Eng. J. 331, 364–371. https://doi.org/10.1016/j.cej.2017.08.117

Luo, C., Gao, J., Wu, D., Jiang, J., Liu, Y., Zhou, W., Ma, J., 2019. Oxidation of 2,4-bromophenol by UV/PDS and formation of bromate and brominated products: A comparison to UV/H_2O_2. Chem. Eng. J. 358, 1342–1350. https://doi.org/10.1016/j.cej.2018.10.084

Luo, C., Jiang, J., Ma, J., Pang, S., Liu, Y., Song, Y., Guan, C., Li, J., Jin, Y., Wu, D., 2016. Oxidation of the odorous compound 2,4,6-trichloroanisole by UV activated persulfate: Kinetics, products, and pathways. Water Res. 96, 12–21. https://doi.org/10.1016/j.watres.2016.03.039

Luo, S., Wei, Z., Spinney, R., Villamena, F.A., Dionysiou, D.D., Chen, D., Tang, C.J., Chai, L., Xiao, R., 2018. Quantitative structure–activity relationships for reactivities of sulfate and hydroxyl radicals with aromatic contaminants through single–electron transfer pathway. J. Hazard. Mater. 344, 1165–1173. https://doi.org/10.1016/j.jhazmat.2017.09.024

Luo, X., Yang, X., Qiao, X., Wang, Y., Chen, J., Wei, X., Peijnenburg, W.J.G.M., Li, X.H., Peake, B.M., Rusak, S.A., Rose, A.L., Waite, T.D., 2017. Development of a QSAR model for predicting aqueous reaction rate constants of organic chemicals with hydroxyl radicals. Environ. Sci. Process. Impacts 19, 350–356. https://doi.org/10.1039/C6EM00707D

Lutterbeck, C.A., Machado, Ê.L., Kümmerer, K., 2015. Photodegradation of the

antineoplastic cyclophosphamide: a comparative study of the efficiencies of UV/H_2O_2, UV/Fe^{2+}/H_2O_2 and UV/TiO_2 processes. Chemosphere 120, 538–46. https://doi.org/10.1016/j.chemosphere.2014.08.076

Lutterbeck, C.A., Wilde, M.L., Baginska, E., Leder, C., Machado, Ê.L., Kümmerer, K., 2016. Degradation of cyclophosphamide and 5-fluorouracil by UV and simulated sunlight treatments: Assessment of the enhancement of the biodegradability and toxicity. Environ. Pollut. 208, 467–476. https://doi.org/10.1016/j.envpol.2015.10.016

Lutze, H. V, Bircher, S., Rapp, I., Kerlin, N., Bakkour, R., Geisler, M., von Sonntag, C., Schmidt, T.C., 2015. Degradation of chlorotriazine pesticides by sulfate radicals and influence of organic matter. Environ. Sci. Technol. 49, 1673–1680. https://doi.org/10.1021/es503496u

Ma, J., Sheridan, R.P., Liaw, A., Dahl, G.E., Svetnik, V., 2015. Deep neural nets as a method for quantitative structure-activity relationships. J. Chem. Inf. Model. 55, 263–274. https://doi.org/10.1021/ci500747n

Mahdi-Ahmed, M., Chiron, S., 2014. Ciprofloxacin oxidation by UV-C activated peroxymonosulfate in wastewater. J. Hazard. Mater. 265, 41–46. https://doi.org/10.1016/j.jhazmat.2013.11.034

Mahnik, S.N., Lenz, K., Weissenbacher, N., Mader, R.M., Fuerhacker, M., 2007. Fate of 5-fluorouracil, doxorubicin, epirubicin, and daunorubicin in hospital wastewater and their elimination by activated sludge and treatment in a membrane-bio-reactor system. Chemosphere 66, 30–37. https://doi.org/10.1016/j.chemosphere.2006.05.051

Mahnik, S.N., Rizovski, B., Fuerhacker, M., Mader, R.M., 2004. Determination of 5-fluorouracil in hospital effluents. Anal. Bioanal. Chem. 380, 31–35. https://doi.org/10.1007/s00216-004-2727-6

Mark, G., Schuchmann, M.N., Schuchmann, H.-P., von Sonntag, C., 1990. The

photolysis of potassium peroxodisulphate in aqueous solution in the presence of tert-butanol: a simple actinometer for 254 nm radiation. J. Photochem. Photobiol. A Chem. 55, 157–168. https://doi.org/10.1016/1010-6030(90)80028-V

Martín, J., Camacho-muñoz, D., Santos, J.L., Aparicio, I., Alonso, E., 2014. Occurrence and Ecotoxicological Risk Assessment of 14 Cytostatic Drugs in Wastewater. Water Air Soil Pollut. 225, 1-10. https://doi.org/10.1007/s11270-014-1896-y

Martín, J., Camacho-Muñoz, D., Santos, J.L., Aparicio, I., Alonso, E., 2011. Simultaneous determination of a selected group of cytostatic drugs in water using high-performance liquid chromatography–triple-quadrupole mass spectrometry. J. Sep. Sci. 34, 3166–3177. https://doi.org/10.1002/jssc.201100461

Martinez, J.L., 2009. Environmental pollution by antibiotics and by antibiotic resistance determinants. Environ. Pollut. 157, 2893–2902. https://doi.org/10.1016/J.ENVPOL.2009.05.051

Michael-Kordatou, I., Iacovou, M., Frontistis, Z., Hapeshi, E., Dionysiou, D.D., Fatta-Kassinos, D., 2015. Erythromycin oxidation and ERY-resistant Escherichia coli inactivation in urban wastewater by sulfate radical-based oxidation process under UV-C irradiation. Water Res. 85, 346–358. https://doi.org/10.1016/j.watres.2015.08.050

Miolo, G., Marzano, C., Gandin, V., Palozzo, A.C., Dalzoppo, D., Salvador, A., Caffieri, S., 2011. Photoreactivity of 5-fluorouracil under UVB light: Photolysis and cytotoxicity studies. Chem. Res. Toxicol. 24, 1319–1326. https://doi.org/10.1021/tx200212z

Moldovan, Z., 2006. Occurrences of pharmaceutical and personal care products as micropollutants in rivers from Romania. Chemosphere 64, 1808–1817.

https://doi.org/10.1016/j.chemosphere.2006.02.003

Moreira, N.F.F., Orge, C.A., Ribeiro, A.R., Faria, J.L., Nunes, O.C., Silva, M.T., Pereira, M.F.R., 2015. Fast mineralization and detoxification of amoxicillin and diclofenac by photocatalytic ozonation and application to an urban wastewater. Water Res. 87, 87–96. https://doi.org/10.1016/j.watres.2015.08.059

Negreira, N., de Alda, M.L., Barcelo, D., 2014. Study of the stability of 26 cytostatic drugs and metabolites in wastewater under different conditions. Sci. Total Environ. 482, 389–398. https://doi.org/10.1016/j.scitotenv.2014.02.131

Neta, P., Huie, R.E., Ross, A.B., 1988. Rate constants for reactions of inorganic radicals in aqueous solution. J. Phys. Chem. Ref. Data 17, 1027–1284. https://doi.org/10.1063/1.555808

Neta, P., Madhavan, V., Zemel, H., Fessenden, R.W., 1977. Rate constants and mechanism of reaction of $SO_4^{\bullet-}$ with aromatic compounds. J. Am. Chem. Soc. 99, 163–164.

Nihemaiti, M., Miklos, D.B., Hübner, U., Linden, K.G., Drewes, J.E., Croué, J.P., 2018. Removal of trace organic chemicals in wastewater effluent by UV/H_2O_2 and UV/PDS. Water Res. 145, 487–497. https://doi.org/10.1016/j.watres.2018.08.052

Ocampo-Pérez, R., Sánchez-Polo, M., Rivera-Utrilla, J., Leyva-Ramos, R., 2010. Degradation of antineoplastic cytarabine in aqueous phase by advanced oxidation processes based on ultraviolet radiation. Chem. Eng. J. 165, 581–588. https://doi.org/10.1016/j.cej.2010.09.076

Ortiz, S., García, D., Pinto, G., García, P., Irusta, R., 2013. Science of the Total Environment Consumption and occurrence of pharmaceutical and personal care products in the aquatic environment in Spain. Sci. Total Environ. 444, 451–465. https://doi.org/10.1016/j.scitotenv.2012.11.057

Parrella, A., Lavorgna, M., Criscuolo, E., Russo, C., Isidori, M., 2014. Estrogenic activity and cytotoxicity of six anticancer drugs detected in water systems. Sci. Total Environ. 485, 216–222. https://doi.org/10.1016/j.scitotenv.2014.03.050

Pereira, J.H.O.S., Reis, A.C., Homem, V., Silva, J.A., Alves, A., Borges, M.T., Boaventura, R.A.R., Vilar, V.J.P., Nunes, O.C., 2014. Solar photocatalytic oxidation of recalcitrant natural metabolic by-products of amoxicillin biodegradation. Water Res. 65, 307–320. https://doi.org/10.1016/j.watres.2014.07.037

Rickman, K.A., Mezyk, S.P., 2010. Kinetics and mechanisms of sulfate radical oxidation of beta-lactam antibiotics in water. Chemosphere 81, 359–365. https://doi.org/10.1016/j.chemosphere.2010.07.015

Rowney, N.C., Johnson, A.C., Williams, R.J., 2009. Cytotoxic drugs in drinking water: a prediction and risk assessment exercise for the thames catchment in the United Kingdom. Environ. Toxicol. Chem. 28, 2733–2743. http://doi.org/10.1897/09-067.1

Shah, N.S., He, X., Khan, H.M., Khan, J.A., O'Shea, K.E., Boccelli, D.L., Dionysiou, D.D., 2013. Efficient removal of endosulfan from aqueous solution by UV-C/peroxides: a comparative study. J. Hazard. Mater. 263, 584–592. https://doi.org/10.1016/j.jhazmat.2013.10.019

Shahrokhian, S., Ghalkhani, M., 2010. Glassy carbon electrodes modified with a film of nanodiamond–graphite/chitosan: Application to the highly sensitive electrochemical determination of Azathioprine. Electrochim. Acta 55, 3621–3627. https://doi.org/10.1016/j.electacta.2010.01.099

Shahrokhian, S., Ghalkhani, M., 2009. Electrochemical study of Azathioprine at thin carbon nanoparticle composite film electrode. Electrochem. commun. 11, 1425–1428. https://doi.org/10.1016/j.elecom.2009.05.025

Sharma, V.K., Liu, F., Tolan, S., Sohn, M., Kim, H., Oturan, M.A., 2013. Oxidation

of b -lactam antibiotics by ferrate (VI). Chem. Eng. J. 221, 446–451. https://doi.org/10.1016/j.cej.2013.02.024

Singh, S., Singla, R.K., Kumar, M., Gupta, R.L., 1988. Specific determination of azathioprine in solution by a spectrophotometric method and its application to a tablet assay. Analyst 113, 1665–1668. https://doi.org/10.1039/an9881301665

Somensi, C.A., Simionatto, E.L., Dalmarco, J.B., Gaspareto, P., Radetski, C.M., 2012. A comparison between ozonolysis and sonolysis/ozonolysis treatments for the degradation of the cytostatic drugs methotrexate and doxorubicin: Kinetic and efficiency approaches. J. Environ. Sci. Heal. - Part A Toxic/Hazardous Subst. Environ. Eng. 47, 1543–1550. https://doi.org/10.1080/10934529.2012.680414

Song, R., Keller, A.A., Suh, S., 2017. Rapid life-cycle impact screening using artificial neural networks. Environ. Sci. Technol. 51, 10777–10785. https://doi.org/10.1021/acs.est.7b02862

Song, W., Chen, W., Cooper, W.J., Greaves, J., Miller, G.E., 2008. Free-radical destruction of beta-lactam antibiotics in aqueous solution. J. Phys. Chem. A 112, 7411–7417. https://doi.org/10.1021/jp803229a

Steger-hartmann, T., Kiimmerer, K., Schecker, J., 1996. Trace analysis of the antineoplastics ifosfamide and cyclophosphamide in sewage water by two-step solid-phase extraction and gas chromatography-mass spectrometry. J. Chromatogr. A 726, 179–184.

StegerHartmann, T., Kümmerer, K., Hartmann, A., 1997. Biological degradation of cyclophosphamide and its occurrence in sewage water. Ecotoxicol. Environ. Saf. 179, 174–179.

Sunil Paul, M.M., Aravind, U.K., Pramod, G., Saha, a., Aravindakumar, C.T., 2014. Hydroxyl radical induced oxidation of theophylline in water: a kinetic and mechanistic study. Org. Biomol. Chem. 12, 5611.

https://doi.org/10.1039/C4OB00102H

Szabó, L., Tóth, T., Engelhardt, T., Rácz, G., Mohácsi-Farkas, C., Takács, E., Wojnárovits, L., 2016a. Change in hydrophilicity of penicillins during advanced oxidation by radiolytically generated .OH compromises the elimination of selective pressure on bacterial strains. Sci. Total Environ. 551–552, 393–403. https://doi.org/10.1016/j.scitotenv.2016.02.002

Szabó, L., Tóth, T., Rácz, G., Takács, E., Wojnárovits, L., 2016b. OH and e-aq are yet good candidates for demolishing the beta-lactam system of a penicillin eliminating the antimicrobial activity. Radiat. Phys. Chem. 124, 84–90. https://doi.org/10.1016/j.radphyschem.2015.10.012

Tan, C., Gao, N., Deng, Y., Zhang, Y., Sui, M., Deng, J., Zhou, S., 2013. Degradation of antipyrine by UV, UV/H_2O_2 and UV/PS. J. Hazard. Mater. 260, 1008–1016. https://doi.org/10.1016/j.jhazmat.2013.06.060

Tauxe-Wuersch, A., Alencastro, L.F. De, Grandjean, D., Grandjean, D., Tarradellas, J., 2006. Trace determination of tamoxifen and 5-fluorouracil in hospital and urban wastewaters. Int. J. Environ. Anal. Chem. 86, 473–485. https://doi.org/10.1080/03067310500291502

Ternes, T.A., 1998. Occurrence of drugs in German sewage treatment plants and rivers. Water Res. 32, 3245-3260. https://doi.org/10.1016/S0043-1354(98)00099-2

Thomas, K. V, Dye, C., Schlabach, M., Langford, K.H., 2007. Source to sink tracking of selected human pharmaceuticals from two Oslo city hospitals and a wastewater treatment works w. J. Environ. Monit. 9, 1410–1418. https://doi.org/10.1039/b709745j

Toth, J.E., Rickman, K.A., Venter, A.R., Kiddle, J.J., Mezyk, S.P., 2012. Reaction kinetics and efficiencies for the hydroxyl and sulfate radical based oxidation of artificial sweeteners in water. J. Phys. Chem. A 116, 9819–9824.

https://doi.org/10.1021/jp3047246

Trovó, A.G., Pupo Nogueira, R.F., Agüera, A., Fernandez-Alba, A.R., Malato, S., 2011. Degradation of the antibiotic amoxicillin by photo-Fenton process - Chemical and toxicological assessment. Water Res. 45, 1394–1402. https://doi.org/10.1016/j.watres.2010.10.029

Verma, S., Sillanpää, M., 2015. Degradation of anatoxin-a by UV-C LED and UV-C LED/H_2O_2 advanced oxidation processes. Chem. Eng. J. 274, 274–281. https://doi.org/10.1016/j.cej.2015.03.128

Wammer, K.H., Lapara, T.M., McNeill, K., Arnold, W. a, Swackhamer, D.L., 2006. Changes in antibacterial activity of triclosan and sulfa drugs due to photochemical transformations. Environ. Toxicol. Chem. 25, 1480–6. https://doi.org/10.1897/05-384r.1

Wang, Z., Shao, Y., Gao, N., An, N., 2018. Degradation kinetic of dibutyl phthalate (DBP) by sulfate radical- and hydroxyl radical-based advanced oxidation process in UV/persulfate system. Sep. Purif. Technol. 195, 92–100. https://doi.org/10.1016/j.seppur.2017.11.072

Watkinson, A.J., Murby, E.J., Costanzo, S.D., 2007. Removal of antibiotics in conventional and advanced wastewater treatment: Implications for environmental discharge and wastewater recycling. Water Res. 41, 4164–4176. https://doi.org/10.1016/j.watres.2007.04.005

Winkler, D.A., Le, T.C., 2017. Performance of deep and shallow neural networks, the universal approximation theorem, activity cliffs, and QSAR molecular informatics. Mol. Inform. 36, 1–6. https://doi.org/10.1002/minf.201781141

Wols, B. a., Hofman-Caris, C.H.M., Harmsen, D.J.H., Beerendonk, E.F., 2013. Degradation of 40 selected pharmaceuticals by UV/H_2O_2. Water Res. 47, 5876–5888. https://doi.org/10.1016/j.watres.2013.07.008

Wols, B.A., Hofman-Caris, C.H.M., 2012. Review of photochemical reaction

constants of organic micropollutants required for UV advanced oxidation processes in water. Water Res. 46, 2815–2827. https://doi.org/10.1016/j.watres.2012.03.036

Xiao, R., Ye, T., Wei, Z., Luo, S., Yang, Z., Spinney, R., 2015a. Quantitative structure−activity relationship (QSAR) for the oxidation of trace organic contaminants by sulfate radical. Environ. Sci. Technol. 49, 13394–13402. https://doi.org/10.1021/acs.est.5b03078

Xiao, R., Zammit, I., Wei, Z., Hu, W., Macleod, M., 2015b. Kinetics and mechanism of the oxidation of cyclic methylsiloxanes by hydroxyl radical in the gas phase: An experimental and theoretical study. Environ. Sci. Technol. 49, 13322-13330. https://doi.org/10.1021/acs.est.5b03744

Xiao, Y., Fan, R., Zhang, L., Yue, J., Webster, R.D., Lim, T.T., 2014. Photodegradation of iodinated trihalomethanes in aqueous solution by UV 254 irradiation. Water Res. 49, 275–285. https://doi.org/10.1016/j.watres.2013.11.039

Xiao, Y., Zhang, L., Zhang, W., Lim, K.-Y., Webster, R.D., Lim, T.-T., 2016. Comparative evaluation of iodoacids removal by UV/persulfate and UV/H_2O_2 processes. Water Res. 102, 629–639. https://doi.org/10.1016/j.watres.2016.07.004

Xie, P., Ma, J., Liu, W., Zou, J., Yue, S., Li, X., Wiesner, M.R., Fang, J., 2015. Removal of 2-MIB and geosmin using UV/persulfate: Contributions of hydroxyl and sulfate radicals. Water Res. 69, 223–233. https://doi.org/10.1016/j.watres.2014.11.029

Yang, Y., Lu, X., Jiang, J., Ma, J., Liu, G., Cao, Y., Liu, W., Li, J., Pang, S., Kong, X., Luo, C., 2017. Degradation of sulfamethoxazole by UV, UV/H_2O_2 and UV/persulfate (PDS): Formation of oxidation products and effect of bicarbonate. Water Res. 118, 196–207.

https://doi.org/10.1016/j.watres.2017.03.054

Yang, Z., Luo, S., Wei, Z., Ye, T., Spinney, R., Chen, D., Xiao, R., 2016. Rate constants of hydroxyl radical oxidation of polychlorinated biphenyls in the gas phase : A single-descriptor based QSAR and DFT study. Environ. Pollut. 211, 157–164. https://doi.org/10.1016/j.envpol.2015.12.044

Ye, T., Wei, Z., Spinney, R., Dionysiou, D.D., Luo, S., Chai, L., Yang, Z., Xiao, R., 2017a. Quantitative structure–activity relationship for the apparent rate constants of aromatic contaminants oxidized by ferrate (VI). Chem. Eng. J. 317, 258–266. https://doi.org/10.1016/j.cej.2017.02.061

Ye, T., Wei, Z., Spinney, R., Tang, C., Luo, S., Xiao, R., Dionysiou, D.D., 2017b. Chemical structure-based predictive model for the oxidation of trace organic contaminants by sulfate radical. Water Res. 116, 106–115. https://doi.org/10.1016/j.watres.2017.03.015

Yin, J., Shao, B., Zhang, J., Li, K., 2010. A preliminary study on the occurrence of cytostatic drugs in hospital effluents in Beijing, China. Bull. Environ. Contam. Toxicol. 84, 39–45. https://doi.org/10.1007/s00128-009-9884-4

Zhang, B.-T., Zhang, Y., Teng, Y., Fan, M., 2015. Sulfate radical and its application in decontamination technologies. Crit. Rev. Environ. Sci. Technol. 45, 1756–1800. https://doi.org/10.1080/10643389.2014.970681

Zhang, J., Chang, V.W.C., Giannis, A., Wang, J.-Y., 2013. Removal of cytostatic drugs from aquatic environment: A review. Sci. Total Environ. 445, 281–298. https://doi.org/10.1016/j.scitotenv.2012.12.061

Zhang, R., Sun, P., Boyer, T.H., Zhao, L., Huang, C.-H., 2015. Degradation of pharmaceuticals and metabolite in synthetic human urine by UV, UV/H_2O_2, and UV/PDS. Environ. Sci. Technol. 49, 3056–3066. https://doi.org/10.1021/es504799n

Zhang, Y., Xiao, Y., Zhang, J., Chang, V.W.C., Lim, T.-T., 2017a. Degradation of

cyclophosphamide and 5-fluorouracil in water using UV and UV/H_2O_2: Kinetics investigation, pathways and energetic analysis. J. Environ. Chem. Eng. 5, 1133–1139. https://doi.org/10.1016/j.jece.2017.01.013

Zhang, Y., Zhang, J., Xiao, Y., Chang, V.W.C., Lim, T.-T., 2017b. Direct and indirect photodegradation pathways of cytostatic drugs under UV germicidal irradiation: Process kinetics and influences of water matrix species and oxidant dosing. J. Hazard. Mater. 324, 481–488. https://doi.org/10.1016/j.jhazmat.2016.11.016

Zhang, Y., Zhang, J., Xiao, Y., Chang, V.W.C., Lim, T.T., 2016. Kinetic and mechanistic investigation of azathioprine degradation in water by UV, UV/H_2O_2 and UV/persulfate. Chem. Eng. J. 302, 526–534. https://doi.org/10.1016/j.cej.2016.05.085

Zhou, L., Ferronato, C., Chovelon, J.M., Sleiman, M., Richard, C., 2017a. Investigations of diatrizoate degradation by photo-activated persulfate. Chem. Eng. J. 311, 28–36. https://doi.org/10.1016/j.cej.2016.11.066

Zhou, L., Sleiman, M., Ferronato, C., Chovelon, J.M., de Sainte-Claire, P., Richard, C., 2017b. Sulfate radical induced degradation of B2-adrenoceptor agonists salbutamol and terbutaline: Phenoxyl radical dependent mechanisms. Water Res. 123, 715–723. https://doi.org/10.1016/j.watres.2017.07.025

Zoschke, K., Dietrich, N., Börnick, H., Worch, E., 2012. UV-based advanced oxidation processes for the treatment of odour compounds: efficiency and by-product formation. Water Res. 46, 5365–73. https://doi.org/10.1016/j.watres.2012.07.012

APPENDIX

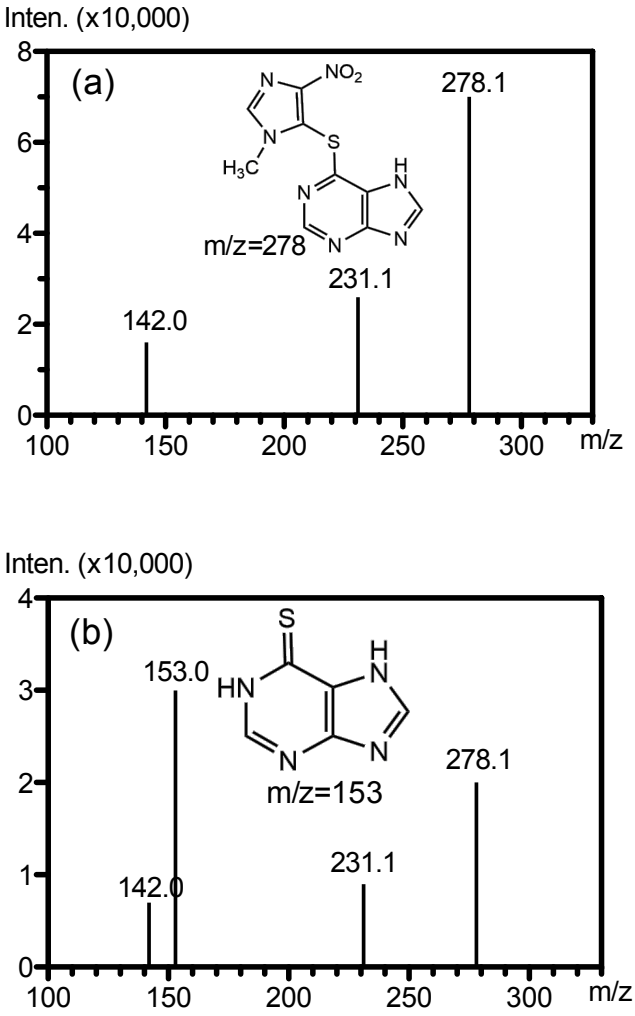

Appendix 1 Mass spectrum of AZA solution (a) before and (b) after UV photolysis.

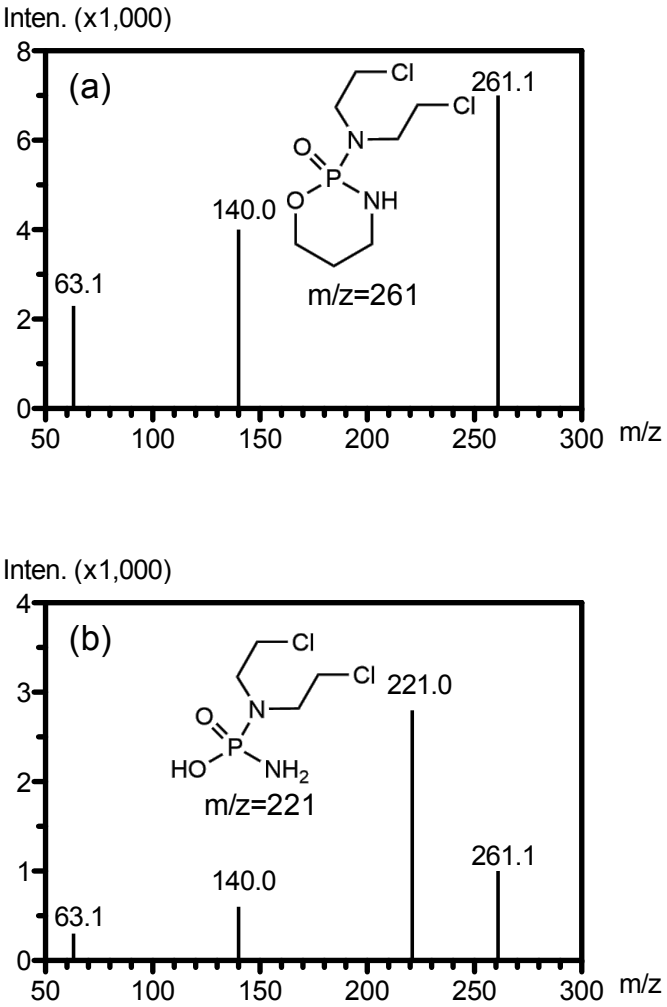

Appendix 2 Mass spectrum of CP solution (a) before and (b) after UV photolysis.

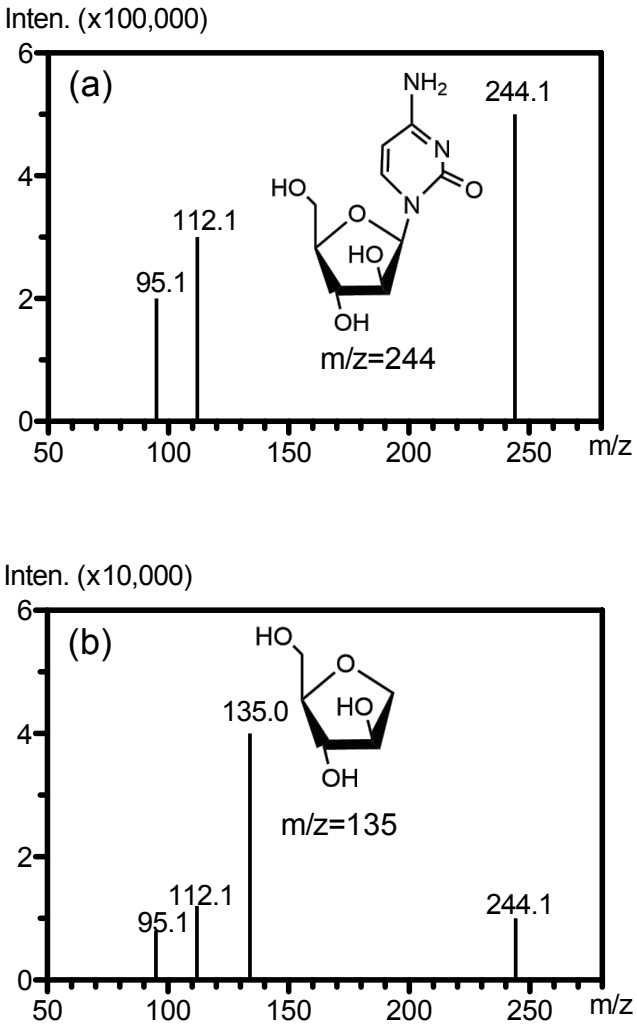

Appendix 3 Mass spectrum of CYT solution (a) before and (b) after UV photolysis.

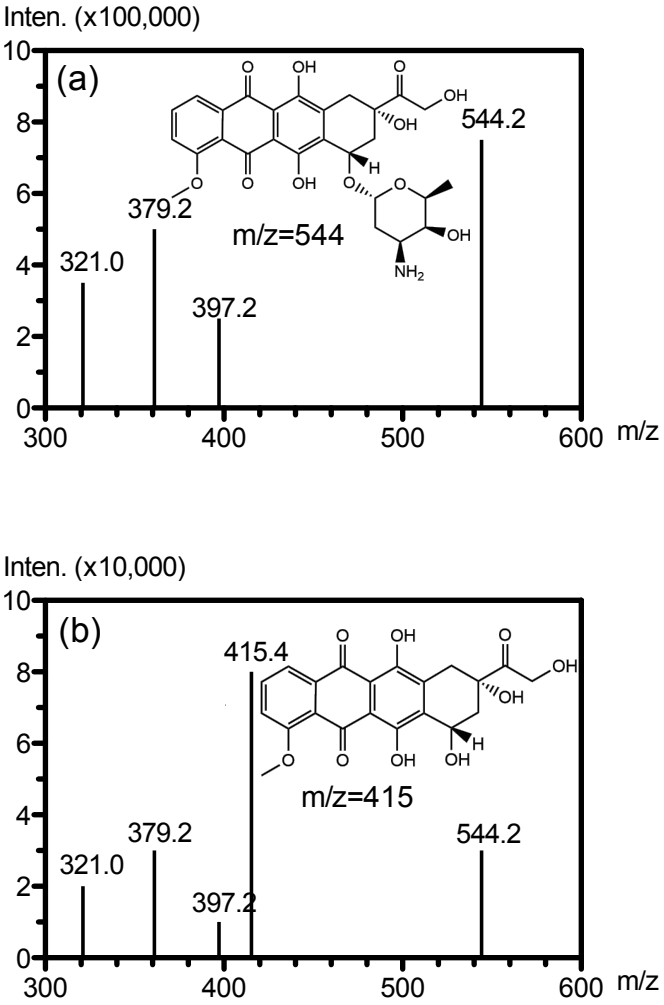

Appendix 4 Mass spectrum of DOX solution (a) before and (b) after UV photolysis.

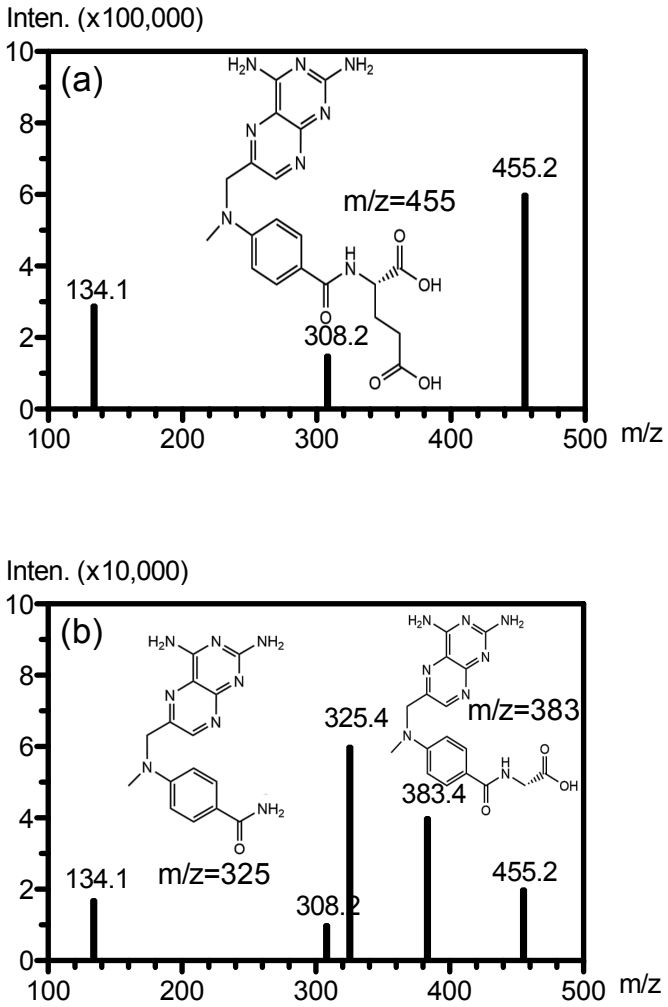

Appendix 5 Mass spectrum of MET solution (a) before and (b) after UV photolysis.

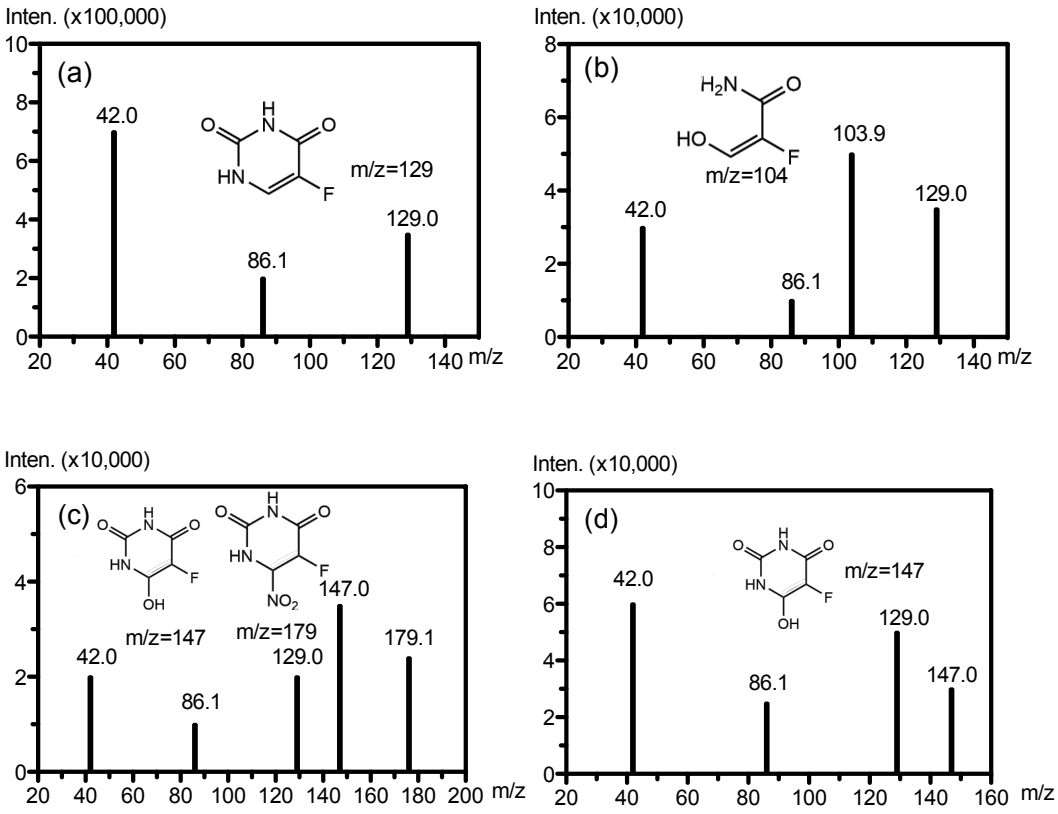

Appendix 6 Mass spectrum of 5FU solution (a) before treatment, (b) after UV photolysis, (c) after NO_3^--induced irradiation and (d) after DOM-induced irradiation.

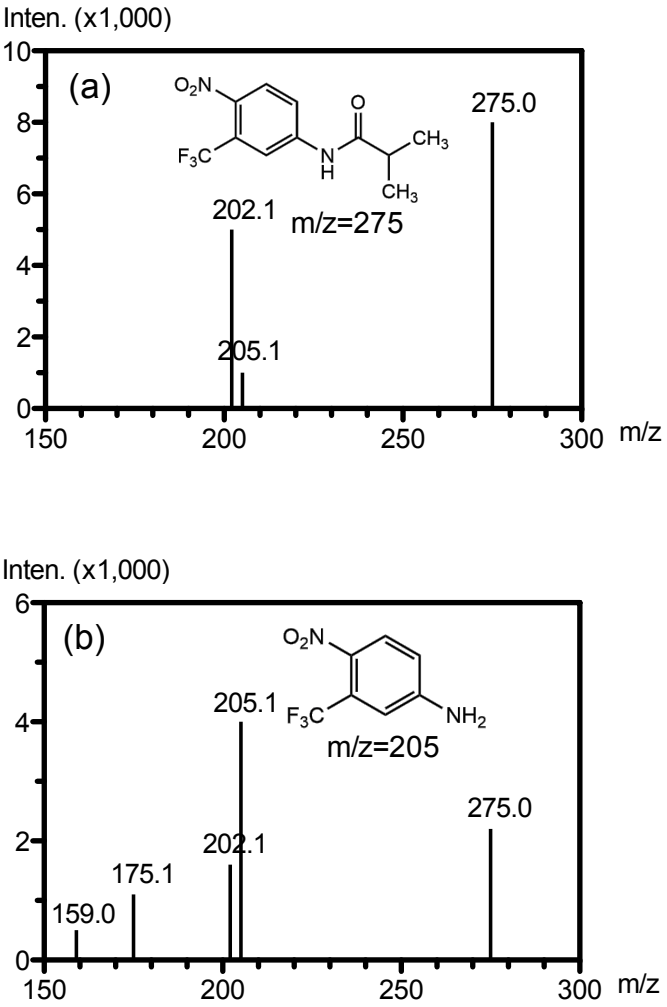

Appendix 7 Mass spectrum of FLU solution (a) before and (b) after UV photolysis.

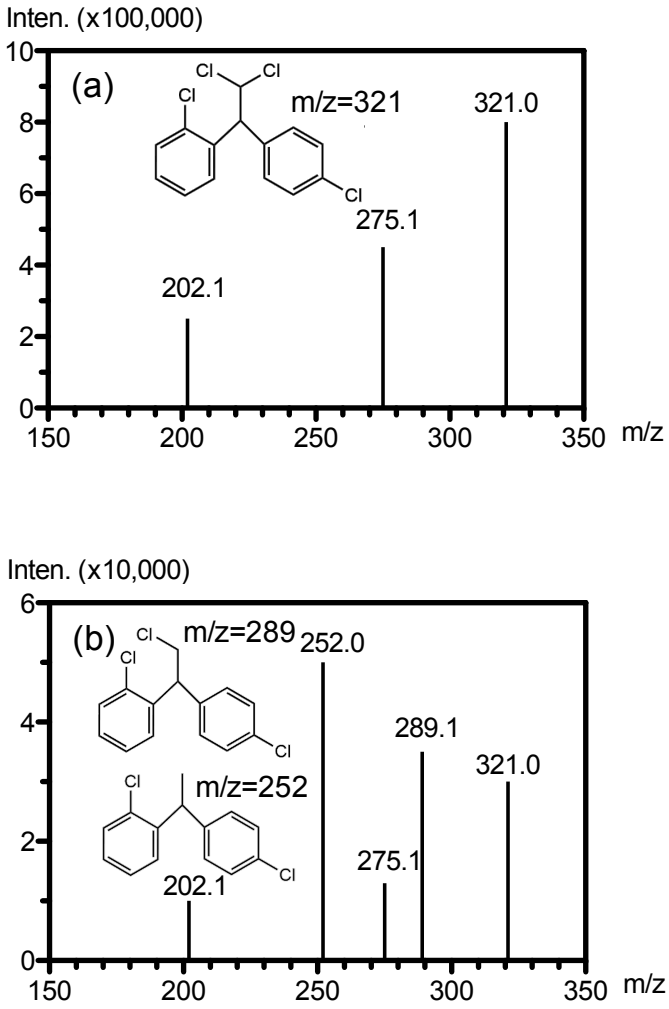

Appendix 8 Mass spectrum of MIT solution (a) before and (b) after UV photolysis.

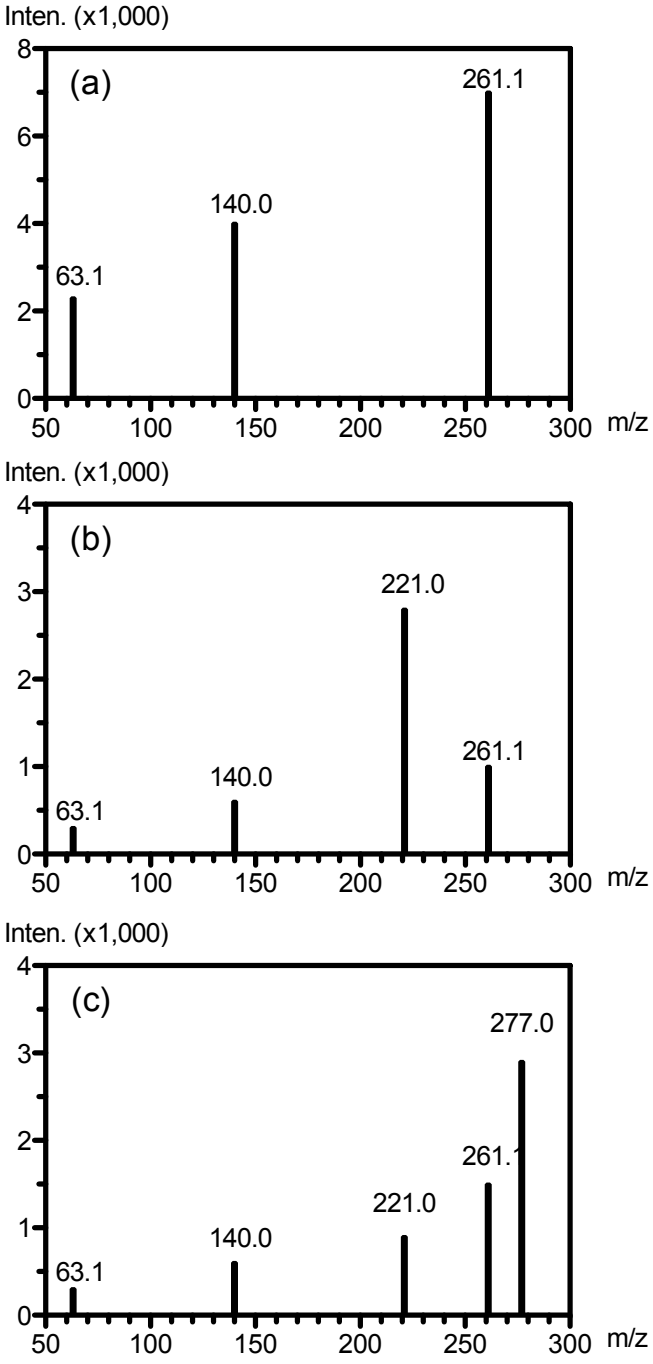

Appendix 9 Mass spectrum of CP solution (a) before treatment, (b) after direct UV photolysis, and (c) after UV/H_2O_2 treatment.

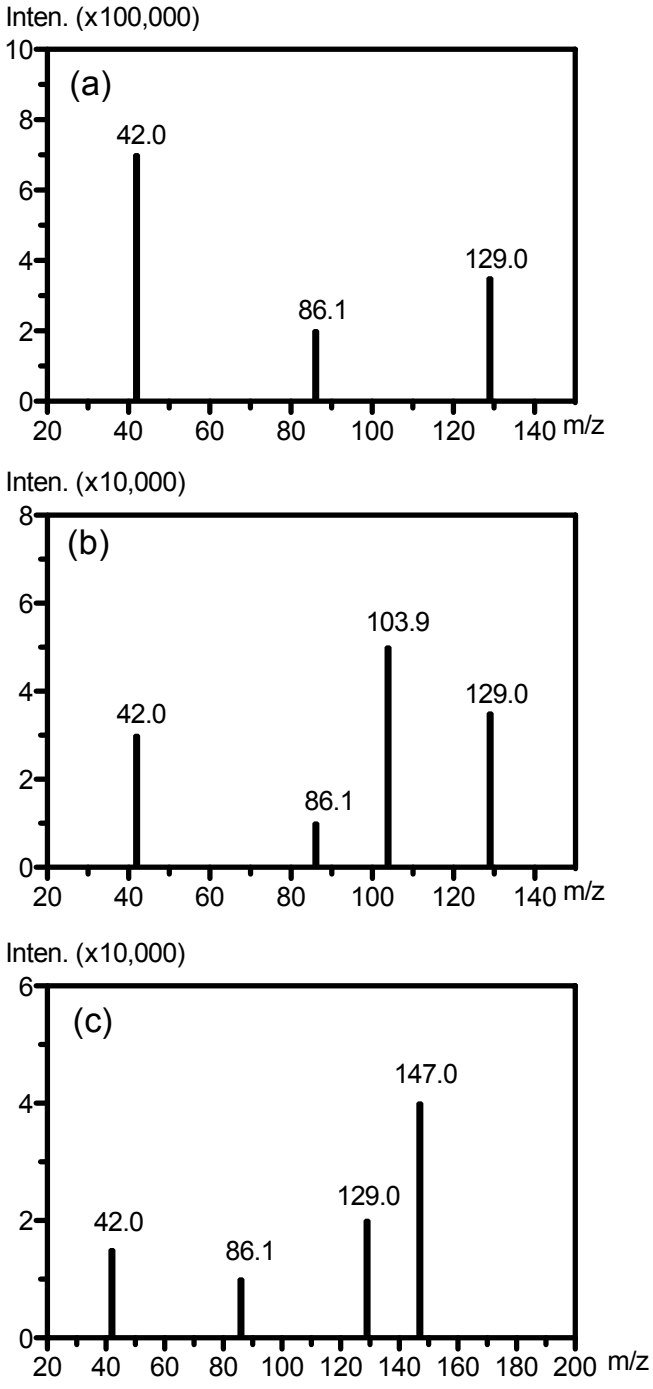

Appendix 10 Mass spectrum of 5FU solution (a) before treatment, (b) after direct direct UV photolysis, and (c) after UV/H_2O_2 treatment.

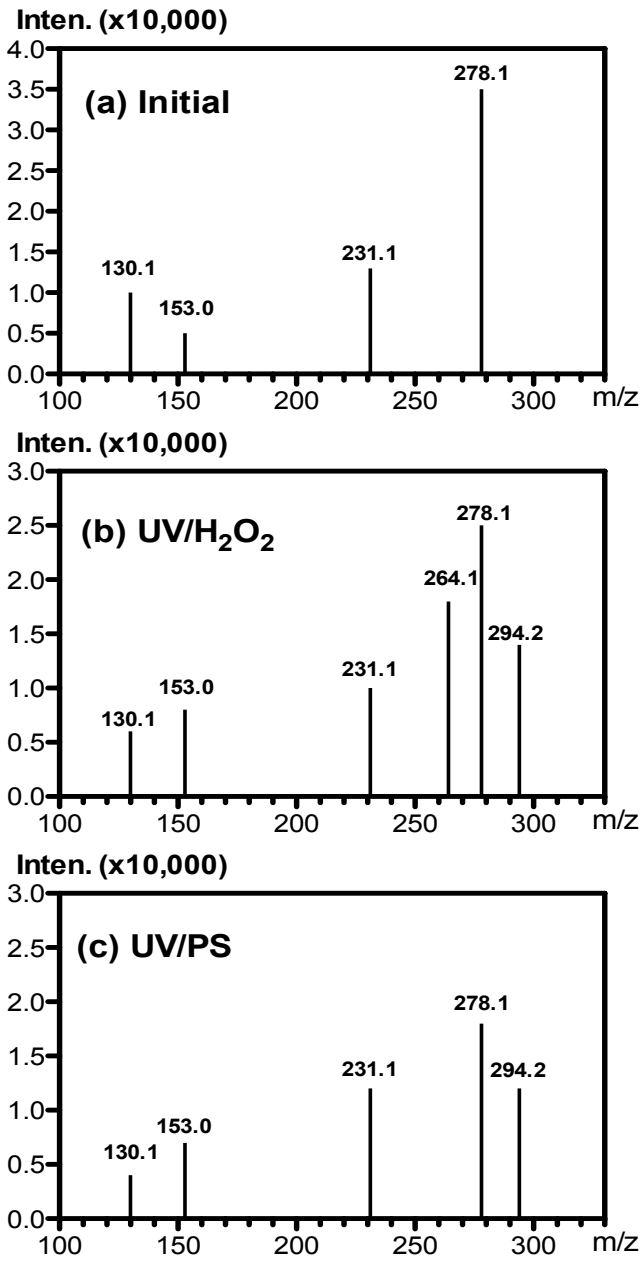

Appendix 11 Mass spectrum of AZA solution: (a) before treatment, (b) after 3 min of UV/H_2O_2 treatment and (c) after 3 min of UV/PS treatment.

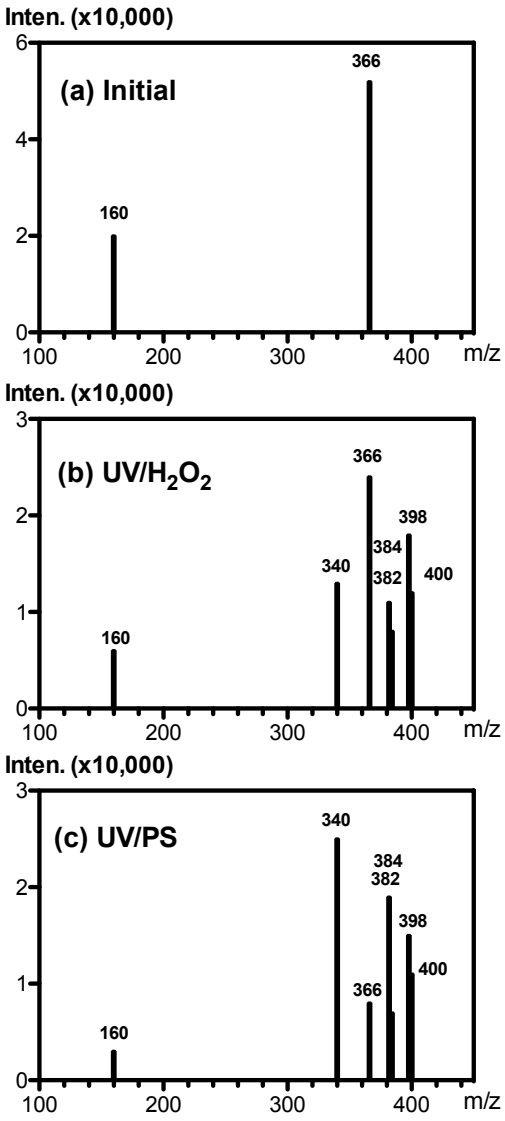

Appendix 12 Mass spectrum of AMX solution: (a) before treatment, (b) after UV/H_2O_2 treatment and (c) after UV/PS treatment.

Appendix 13 Second-order rate constants between micropollutants with radicals.

No.	Chemical	$k_{HO^{\cdot}}$	$k_{SO_4^{\cdot-}}$
1	1-butanol	4.20E+09	8.00E+07
2	1-heptanol	7.40E+09	2.50E+08
3	1-hexanol	7.00E+09	1.60E+08
4	1-octanol	7.70E+09	3.20E+08
5	1-pentanol	3.90E+09	1.30E+08
6	1-propanol	3.20E+09	5.35E+07
7	1,2-dimethoxy-benzene	5.20E+09	5.00E+09
8	1,2,3-trimethoxy-benzene	7.00E+09	7.00E+09
9	1,2,4-trimethoxy-benzene	6.20E+09	7.80E+09
10	1,3-dimethoxy-benzene	7.20E+09	7.00E+09
11	1,3,5-trimethoxy-benzene	8.10E+09	1.80E+09
12	1,4-benzoquinone	1.20E+09	1.00E+08
13	1,4-dimethoxy-benzene	7.00E+09	7.20E+09
14	1,4-dioxane	3.10E+09	2.85E+07
15	1H-benzotriazole	8.24E+09	1.10E+09
16	2-chloroethanol	9.12E+08	1.10E+07
17	2-methylisoborneol	4.30E+09	4.20E+08
18	2-propanol	1.90E+09	8.55E+07
19	2,2-dimethyl-1-propanol	5.20E+09	2.50E+07
20	2,4-bromophenol	8.73E+09	4.32E+09
21	2,4,6-trichloroanisole	5.10E+09	3.72E+09
22	2,4,6-trichorophenol	5.48E+09	4.16E+09
23	3-methylindole	5.57E+09	1.20E+10
24	3-pentanol	2.10E+09	1.60E+08
25	3,4,5-trihydroxybenzoate	2.50E+10	2.90E+09
26	acetamiprid	7.59E+08	3.68E+08
27	acetanilide	5.20E+09	3.60E+09
28	acetic acid	2.30E+07	1.40E+04
29	acetophenone	6.40E+09	3.10E+08
30	amoxicillin	6.94E+09	3.48E+09
31	ampicillin	4.87E+09	2.00E+09
32	anisole	5.40E+09	4.90E+09
33	aspartame	6.06E+09	2.28E+09
34	atenolol	7.05E+09	5.11E+09
35	atrazine	2.70E+09	3.50E+09
36	azathioprine	1.86E+09	2.16E+09
37	benzamide	4.60E+09	1.90E+08

38	benzene	7.80E+09	6.55E+08
39	benzoate	5.90E+09	1.20E+09
40	benzoic acid	4.30E+09	1.20E+09
41	benzonitrile	3.90E+09	1.20E+08
42	benzotriazole	8.34E+09	8.70E+08
43	caffeine	6.40E+09	2.39E+09
44	carbamazepine	8.02E+09	1.50E+09
45	carbenicillin	7.31E+09	1.23E+09
46	cephalothin	5.37E+09	3.48E+09
47	chlorophene	8.47E+09	1.80E+09
48	ciprofloxacin	2.15E+09	1.20E+09
49	clofibric acid	2.72E+09	1.73E+09
50	cloxacillin	6.27E+09	1.25E+09
51	cyclohexanoic acid	5.50E+09	5.30E+07
52	cylindrospermopsin	5.10E+09	4.50E+09
53	cytarabine	3.15E+10	1.61E+09
54	desethyl-atrazine	1.20E+09	9.60E+08
55	desisopropyl-atrazine	1.90E+09	2.00E+09
56	diatrizoate	6.10E+08	1.90E+09
57	dibutyl phthalate	6.30E+09	1.20E+08
58	diclofenac	7.50E+09	9.20E+09
59	diethyl disulfide	1.41E+10	2.60E+08
60	diethyl ether	2.90E+09	1.76E+08
61	dimetridazole	3.65E+09	3.30E+09
62	endosulfan	1.83E+09	1.50E+09
63	ethane	1.80E+09	4.40E+06
64	ethanol	2.10E+09	4.30E+07
65	florfenicol	1.76E+10	1.32E+08
66	formaldehyde	7.60E+08	1.10E+07
67	gabapentin	9.10E+09	1.00E+09
68	gallic acid	1.20E+10	6.30E+08
69	gemfibrozil	5.53E+09	7.13E+08
70	geosmin	5.70E+09	7.60E+08
71	glycolic acid	5.40E+08	4.20E+06
72	ibuprofen	7.40E+09	3.80E+09
73	iodoacetic acid	2.40E+09	3.40E+09
74	iopromide	3.30E+09	3.60E+08
75	isopropanol	1.90E+09	8.20E+07
76	lactic acid	4.30E+08	1.00E+07
77	lindane	5.50E+08	1.30E+09
78	m-toluic acid	8.00E+09	2.00E+09

79	malic acid	8.20E+08	7.70E+06
80	malonic acid	2.40E+07	2.70E+06
81	mesitylene	6.46E+09	1.30E+09
82	methanol	9.70E+08	1.10E+07
83	metoprolol	7.84E+09	3.89E+09
84	metronidazole	3.54E+09	2.74E+09
85	N,N-diethyl-m-toluamide	7.51E+09	9.50E+08
86	N4-acetyl-sulfamethoxazole	6.51E+09	2.68E+09
87	naproxen	8.99E+09	5.64E+09
88	nortriptyline hydrochloride	1.09E+10	2.00E+10
89	ornidazole	2.66E+09	2.39E+09
90	p-cresol	1.20E+10	2.80E+09
91	p-Hydroxybenzoate	6.70E+09	2.50E+09
92	p-Hydroxybenzoic acid	2.19E+09	2.50E+09
93	p-xylene	7.00E+09	2.70E+09
94	penicillin G	7.97E+09	2.08E+09
95	penicillin V	6.54E+09	2.39E+09
96	phenol	6.60E+09	8.80E+09
97	phenytoin	6.28E+09	6.20E+08
98	piperacillin	8.21E+09	1.85E+09
99	primidone	6.70E+09	5.30E+08
100	propane	3.63E+09	4.00E+07
101	propanol	2.80E+09	6.00E+07
102	propazine	1.20E+09	2.20E+09
103	propionic acid	3.20E+08	4.60E+06
104	propranolol	1.07E+10	4.79E+09
105	ractopamine	3.85E+09	1.68E+09
106	ronidazole	2.25E+09	2.47E+09
107	s-triazine	9.60E+07	8.10E+07
108	salbutamol	2.62E+09	1.79E+09
109	succinic acid	1.10E+08	7.10E+06
110	sucralose	1.50E+09	1.70E+08
111	sulfaclozine	6.55E+09	1.23E+10
112	sulfadiazine	8.78E+09	4.16E+10
113	sulfadimethoxypyrimidine	8.14E+09	7.70E+09
114	sulfamerazine	7.35E+09	4.90E+10
115	sulfamethazine	8.81E+09	3.58E+10
116	sulfamethoxazole	7.46E+09	1.39E+10
117	sulfamethoxypyridazine	6.21E+09	8.12E+10
118	sulfamonomethoxine	9.26E+09	1.33E+10
119	sulfathiazole	7.73E+09	4.71E+10

120	terbutaline	5.90E+09	4.20E+09
121	tetrahydrofuran	4.00E+09	1.72E+08
122	thyroxine	1.01E+10	3.77E+09
123	ticarcillin	8.18E+09	1.67E+09
124	tinidazole	2.74E+09	2.92E+09
125	toluene	5.10E+09	1.30E+09
126	trimethoprim	7.76E+09	6.78E+09
127	tris-(2-chloroethyl)-phosphate	5.60E+08	1.00E+09
128	venlafaxine	8.80E+09	4.99E+09

Appendix 14 R_{all} values of k_{HO}. model developed by CA-ANN and CA-DNN.

Number of neurons	CA-ANN (1 hidden layer)	CA-DNN (2 hidden layers)	CA-DNN (3 hidden layers)
1	0.6231	0.71	0.5929
2	0.7481	0.7542	0.6924
3	0.6576	0.715	0.7138
4	0.7526	0.557	0.5346
5	0.5689	0.7513	0.6231
6	0.6752	0.7955	0.5709
7	0.8822	0.8194	0.7109
8	0.8238	0.5926	0.5926
9	0.882	0.8347	0.827
10	0.8806	0.8717	0.6907
11	0.8503	0.6227	0.8105
12	0.7181	0.7189	0.6834
13	0.474	0.7363	0.8485
14	0.845	0.5874	0.6149
15	0.8828	0.8036	0.8119
16	0.7849	0.8009	0.8189
17	0.5831	0.8469	0.8775
18	0.8842	0.8073	0.7917
19	0.868	0.7121	0.8098
20	0.7311	0.6866	0.6625
21	0.6586	0.8522	0.877
22	0.7375	0.8589	0.8574
23	0.7872	0.7861	0.2384
24	0.46	0.8345	0.8215
25	0.6884	0.8617	0.6021
26	0.7797	0.8017	0.7685
27	0.8239	0.8078	0.7282
28	0.7053	0.7703	0.7852
29	0.7223	0.7921	0.598
30	0.8102	0.8329	0.8024
31	0.1914	0.5934	0.8657
32	0.7291	0.7442	0.8662

Appendix 15 R_{all} values of k_{HO}. model developed by PCA-ANN and PCA-DNN.

Number of neurons	PCA-ANN (1 hidden layer)	PCA-DNN (2 hidden layers)	PCA-DNN (3 hidden layers)
1	-0.0559	0.2657	0.0248
2	0.2346	0.0139	-0.0321
3	0.3953	0.3164	0.2042
4	-0.0501	0.2288	-0.0365
5	0.1104	0.7892	-0.1183
6	0.1577	0.2608	0.2748
7	0.0881	0.6800	0.8107
8	0.0544	0.2181	0.0035
9	0.0341	0.0527	-0.1590
10	0.4399	0.8951	0.9189
11	0.4068	0.5420	0.8826
12	0.3991	0.2687	0.7112
13	0.0615	0.6560	0.4975
14	0.5007	0.1550	0.0358
15	0.2896	0.7598	0.1642
16	0.5277	0.1840	0.0982
17	0.1004	0.2217	0.1711
18	0.4681	0.3685	0.0136
19	0.4570	0.1493	0.0590
20	0.2228	0.2334	0.8545
21	0.3516	0.1164	0.7202
22	0.2107	0.6373	0.1862
23	0.4631	0.2999	0.2077
24	0.2177	-0.1279	0.6281
25	0.4488	0.7938	0.4033
26	0.4866	0.6281	0.1006
27	0.2762	0.1825	0.5090
28	0.2032	0.4195	0.3408
29	0.7018	0.5406	-0.0517
30	0.6914	0.4512	0.3296
31	0.6428	0.4845	0.8149
32	0.3068	0.5093	0.3466

Appendix 16 R_{all} values of $k_{SO_4^{\bullet-}}$ model developed by CA-ANN and CA-DNN.

Number of neurons	CA-ANN (1 hidden layer)	CA-DNN (2 hidden layers)	CA-DNN (3 hidden layers)
1	0.1745	0.4134	-0.2525
2	0.2503	0.0457	0.0079
3	0.4995	0.5215	0.5312
4	0.6595	0.4613	0.7363
5	0.3833	-0.0023	-0.2083
6	0.0855	0.5099	0.5437
7	0.2093	0.8351	0.0510
8	0.5808	0.2447	0.6375
9	0.7379	-0.1855	0.3917
10	0.6570	-0.2601	0.2346
11	0.3764	0.2080	0.8460
12	0.3283	0.2753	0.5303
13	0.6092	0.8757	0.4382
14	0.8735	0.2821	0.7792
15	0.5090	0.3916	0.1041
16	0.6746	0.2437	-0.1960
17	0.5745	0.2377	0.1729
18	0.6330	0.6981	-0.0516
19	0.5288	0.3591	0.3636
20	0.4768	0.6311	0.0154
21	0.7583	0.2275	0.6570
22	0.7022	-0.0519	0.0017
23	0.8255	0.7009	0.3560
24	0.5179	0.5770	0.3271
25	0.5423	0.5860	0.7840
26	0.5687	0.2092	0.3661
27	0.2360	0.7337	0.5263
28	0.2264	0.2633	0.2775
29	0.2844	0.8958	0.9007
30	0.4260	0.7173	0.6182
31	0.5511	0.5005	-0.0025
32	0.6210	0.4191	0.1633

Appendix 17 R_{all} values of $k_{SO_4^{\bullet-}}$ model developed by PCA-ANN and PCA-DNN.

Number of neurons	PCA-ANN (1 hidden layer)	PCA-DNN (2 hidden layers)	PCA-DNN (3 hidden layers)
1	0.4585	0.4605	0.2347
2	0.1462	0.0271	-0.0195
3	0.5231	0.5077	0.4345
4	0.6000	0.4393	0.6770
5	0.1723	0.3204	-0.0078
6	0.3019	0.5334	0.2139
7	0.0207	0.8312	0.0586
8	0.4769	0.1747	0.0502
9	0.3091	0.7027	-0.1531
10	0.3998	-0.0623	0.3972
11	0.7364	0.4834	0.4718
12	0.5313	0.8127	0.7804
13	0.4732	0.8119	0.9259
14	-0.0285	0.0307	0.4358
15	0.1197	0.8613	0.3045
16	0.5388	0.2788	0.1342
17	0.6397	0.0942	0.4132
18	0.1855	0.4347	0.9409
19	0.9048	0.2322	0.3912
20	0.5001	0.3454	0.5280
21	0.0931	0.7751	0.4119
22	0.3239	0.5828	0.8848
23	0.5673	0.3646	0.4325
24	0.5749	0.7442	-0.0289
25	0.7944	0.3673	0.7191
26	0.4776	0.3507	0.3664
27	0.7456	0.2072	0.6840
28	0.5330	0.6380	0.2494
29	0.4681	0.3897	0.7255
30	0.6130	0.8938	-0.0176
31	0.4766	0.3952	0.7677
32	0.4920	0.4296	0.1411

Appendix 18 Leverage of chemicals based on the selected models.

No.	Chemical	Leverage ($k_{HO^{\bullet}}$)	Leverage ($k_{SO_4^{\bullet-}}$)
1	1-butanol	0.0079	0.0153
2	1-heptanol	0.0104	0.0098
3	1-hexanol	0.0100	0.0115
4	1-octanol	0.0108	0.0091
5	1-pentanol	0.0078	0.0125
6	1-propanol	0.0080	0.0182
7	1,2-dimethoxy-benzene	0.0084	0.0123
8	1,2,3-trimethoxy-benzene	0.0100	0.0141
9	1,2,4-trimethoxy-benzene	0.0092	0.0147
10	1,3-dimethoxy-benzene	0.0102	0.0141
11	1,3,5-trimethoxy-benzene	0.0112	0.0086
12	1,4-benzoquinone	0.0157	0.0140
13	1,4-dimethoxy-benzene	0.0100	0.0142
14	1,4-dioxane	0.0081	0.0235
15	1H-benzotriazole	0.0079	0.0085
16	2-chloroethanol	0.0107	0.0149
17	2-methylisoborneol	0.0084	0.0247
18	2-propanol	0.0083	0.0109
19	2,2-dimethyl-1-propanol	0.0086	0.0114
20	2,4-bromophenol	0.0099	0.0115
21	2,4,6-trichloroanisole	0.0288	0.0100
22	2,4,6-trichorophenol	0.0084	0.0108
23	3-methylindole	0.1627	0.1742
24	3-pentanol	0.0094	0.0091
25	3,4,5-trihydroxybenzoate	0.0099	0.0106
26	acetamiprid	0.0082	0.0089
27	acetanilide	0.0085	0.0122
28	acetic acid	0.0085	0.0107
29	acetophenone	0.0109	0.0091
30	amoxicillin	0.0080	0.0108
31	ampicillin	0.0109	0.0079
32	anisole	0.0089	0.0080
33	aspartame	0.0079	0.0080
34	atenolol	0.0078	0.0130
35	atrazine	0.0103	0.0080
36	azathioprine	0.0085	0.0106
37	benzamide	0.0098	0.0080

38	benzene	0.0093	0.0080
39	benzoate	0.0083	0.0117
40	benzoic acid	0.0343	0.0084
41	benzonitrile	0.0157	0.0078
42	benzotriazole	0.0107	0.0089
43	caffeine	0.0277	0.0088
44	carbamazepine	0.0105	0.0158
45	carbenicillin	0.0083	0.0111
46	cephalothin	0.0110	0.0083
47	chlorophene	0.0111	0.0456
48	ciprofloxacin	0.0099	0.0199
49	clofibric acid	0.0217	0.0125
50	cloxacillin	0.0156	0.0079
51	cyclohexanoic acid	0.0088	0.0078
52	cylindrospermopsin	0.0304	0.0463
53	cytarabine	0.0104	0.0110
54	desethyl-atrazine	0.0091	0.0106
55	desisopropyl-atrazine	0.0107	0.0152
56	diatrizoate	0.0360	0.0347
57	dibutyl phthalate	0.0111	0.0089
58	diclofenac	0.0218	0.0380
59	diethyl disulfide	0.1601	0.0530
60	diethyl ether	0.0189	0.0336
61	dimetridazole	0.0095	0.0097
62	endosulfan	0.0156	0.0098
63	ethane	0.0097	0.0095
64	ethanol	0.0096	0.0095
65	florfenicol	0.0100	0.0097
66	formaldehyde	0.0110	0.0090
67	gabapentin	0.0095	0.0094
68	gallic acid	0.0096	0.0155
69	gemfibrozil	0.0113	0.0087
70	geosmin	0.0084	0.0173
71	glycolic acid	0.0157	0.0091
72	ibuprofen	0.0442	0.0450
73	iodoacetic acid	0.0882	0.0153
74	iopromide	0.0823	0.0390
75	isopropanol	0.0096	0.0178
76	lactic acid	0.0120	0.0289
77	lindane	0.0112	0.0146
78	m-toluic acid	0.0104	0.0307

79	malic acid	0.0120	0.0273
80	malonic acid	0.0105	0.0188
81	mesitylene	0.0092	0.0367
82	methanol	0.0125	0.0184
83	metoprolol	0.0108	0.0303
84	metronidazole	0.0078	0.0112
85	N,N-diethyl-m-toluamide	0.0135	0.0110
86	N4-acetyl-sulfamethoxazole	0.0113	0.0085
87	naproxen	0.0083	0.0081
88	nortriptyline hydrochloride	0.0108	0.0139
89	ornidazole	0.0079	0.0088
90	p-cresol	0.0093	0.0079
91	p-Hydroxybenzoate	0.0115	0.0078
92	p-Hydroxybenzoic acid	0.0120	0.0122
93	p-xylene	0.0109	0.0111
94	penicillin G	0.0111	0.0083
95	penicillin V	0.0094	0.0094
96	phenol	0.0097	0.0081
97	phenytoin	0.0123	0.0079
98	piperacillin	0.0296	0.0079
99	primidone	0.0086	0.0182
100	propane	0.0101	0.0124
101	propanol	0.0141	0.0120
102	propazine	0.0078	0.0098
103	propionic acid	0.0078	0.0104
104	propranolol	0.0086	0.0094
105	ractopamine	0.0095	0.0095
106	ronidazole	0.0085	0.0100
107	s-triazine	0.0086	0.0078
108	salbutamol	0.0122	0.0129
109	succinic acid	0.0078	0.0085
110	sucralose	0.0086	0.0086
111	sulfaclozine	0.0232	0.0087
112	sulfadiazine	0.0144	0.0218
113	sulfadimethoxypyrimidine	0.0087	0.0176
114	sulfamerazine	0.0116	0.0086
115	sulfamethazine	0.0113	0.0079
116	sulfamethoxazole	0.0105	0.0078
117	sulfamethoxypyridazine	0.0093	0.0130
118	sulfamonomethoxine	0.0091	0.0092
119	sulfathiazole	0.0130	0.0113

120	terbutaline	0.0085	0.0086
121	tetrahydrofuran	0.0089	0.0114
122	thyroxine	0.0300	0.0081
123	ticarcillin	0.0232	0.0336
124	tinidazole	0.0078	0.0205
125	toluene	0.0095	0.0081
126	trimethoprim	0.0180	0.0097
127	tris-(2-chloroethyl)-phosphate	0.0199	0.0336
128	venlafaxine	0.0119	0.0116